AN ABSTRACT OF THE THESIS OF

Alexander D. Totpal for the degree of Master of Science in Mechanical Engineering

presented on February 22, 2017.

Title: The Energy Extraction Performance of an Oscillating Rigid and Flexible Foil

Abstract approved: _____

James A. Liburdy

The aerodynamic performance of an oscillating pitching and plunging foil operating in the energy harvesting mode is investigated. Experiments are conducted in a closed-loop recirculating wind tunnel at Reynolds numbers of $24,000$ to $48,000$, and reduced frequencies ($k = fc/u$) of 0.042 to 0.083. Foil kinematics are varied through the following parameter space: non-dimensional heaving amplitude ($h = h_0/c$) of 0.3, pitching amplitudes of 45°, 60°, and 75°, as well as phase lag between sinusoidal pitching and heaving motions of 30° to 120°. Aerodynamic force measurements are collected to show the energy extraction performance of the foil. Coupled with the force measurements, flow fields are collected around the foil using particle image velocimetry (PIV). The flow field characteristics are used to supplement the force results, shedding light into flow features that contribute to more efficient flow energy extraction at these lower reduced frequencies. In addition, inertia-induced passive chord-wise flexibility at the leading edge (LE) of the foil is investigated in order to assess its feasibility in this application. Results indicate that increased energy extraction (in terms of power coefficient and efficiency) occurs near pitching amplitudes of 45°, at a pitch-heave phase of 90° and $k = 0.083$. When k is decreased (through increased Re) to $k = 0.042$, overall extraction performance becomes insensitive to the pitching amplitude and motion phase. This is supported by the flow field measurements, which show premature leading edge vortex (LEV) evolution and detachment from the foil surface. However, these results indicate that a proper tuning of the LE may be used to delay the LEV detachment time, resulting in increased energy harvesting at this otherwise inefficient operating parameter space.

The Energy Extraction Performance of an Oscillating Rigid and Flexible Foil

by

Alexander D. Totpal

A THESIS

submitted to

Oregon State University

in partial fulfillment of
the requirements for the
degree of

Master of Science

Presented February 22, 2017
Commencement June 2017

Master of Science thesis of Alexander D. Totpal presented on February 22, 2017.

APPROVED:

Major Professor, representing Mechanical Engineering

Head of the School of Mechanical, Industrial, and Manufacturing Engineering

---

Dean of the Graduate School

I understand that my thesis will become part of the permanent collection of Oregon State University libraries. My signature below authorizes release of my thesis to any reader upon request.

Alexander D. Totpal, Author

ACKNOWLEDGEMENTS

First off, I would like to thank Dr. James Liburdy for all of your expertise and guidance throughout these last couple of years. At times I wondered how in the world you understood the gibberish I would present to you in our meetings, and you would always know exactly what I was talking about. You helped shape my skills as a researcher and a writer. Thank you for your insight and helping me achieve my goal of finishing off this degree. I would also like to thank my committee members, Drs. Apte, Gess, and McIntyre, for all of your support and guidance during the course of this degree.

Drs. David Blunck, Joshua Gess, James Liburdy, and Deborah Pence, thank you all for taking me on as a graduate teaching assistant (GTA) throughout my graduate career. I have learned a lot with this position and am so grateful that you guys gave me the opportunity to work directly with you all.

I would like to thank Aaron (AJ) Fillo and Cameron Planck for all of your help in designing and manufacturing the motion device and test foil used in this research. I want to extend a big thank you to Ali Mousavian, who created the LabVIEW code used to generate the motion of the motion device, collect force measurements, and synchronize the device with PIV measurements. Over the course of the last two years I have asked Ali to implement new features into the LabVIEW code on several occasions, and, despite his heavy academic load, he was always more than happy to come by and help me out. Without you, Firas and I would probably still be generating that code.

I would like to thank my McMenamins crew, professors James Liburdy, Deborah Pence, and A. Murty Kanury, as well as fellow graduate student attendees Firas Siala and Forrest Anderson. Thank you for all of the beers and heated discussions, as well as the friendships that have developed as a result of these out of office "meetings".

I would like to express my sincere gratitude to my friends Sebastian Okhovat and Firas Siala, whom without their peer pressure, I may not have pursued or completed this degree. I may have only met you guys during our undergrad years at Oregon State, but I know we will be lifelong friends. I also want to thank you guys for all of the memories, the good and the bad. The countless late nights in the library or in Rogers (remember Dr. Apte's CFD class?!). Halloween shenanigans. Cheesy Stuffed Burgers. Having Sebastian live in my living room for a year. The list goes on...

I would like to thank the many others that I met during my graduate studies. Chaitanya Ghodke and his wife Amu Amruta Gupte, Chaitrali Ghodke, Bryan Xiaoliang He and his wife Cathy Huan Wang, Bo Liu, Reza Ziazi, and Pedram Pakseresht. You guys have all played an important part in my life these last couple of years. I especially want to acknowledge Pedram, whom without, I probably wouldn't have even completed my first term as a graduate student! I also want to thank Kyle Zada for continually pushing me throughout the end stages of the thesis writing and defense preparation.

I would like to thank my childhood friends, David Borok, Joseph Harder, and Tabron Vorrath, and friends from high school, Miguel Soler and Erik Demke, for all of your moral support and encouragement.

I would like to thank my mother Holli Dennett, step-father George Dennett, and sister Alora Dennett for all of their encouragement and support. You guys also gave me a place to escape to from the lab every now and then and relax, watch movies, play games, drink coffee, etc. Thank you for everything, I couldn't have done it without you all.

I also want to thank my father Daniel Totpal, my step-mother Rachel Totpal, and my sister Lilliana Totpal. You guys always believed in me and were always supportive of my goals. Dad, thank you for always hearing me out and giving me the inspiration and motivation I needed to get through this degree. I couldn't have done this without you.

I would like to thank my great grandparents on my mother's side, Nana and Papa (Ann and Elmer Buchmiller), whom passed away during this last year. You two are the people I aspire to grow up to be, and are the best role models I have ever come to know. I also want to thank my great grandmother on my father's side, Bunica (Maria Gulerez), who passed away in 2007. You helped shape me into the man I am today, by instilling the right ideals in me from a young age. Plus, you taught me how to speak Romanian, which is pretty sweet.

I would like to thank the rest of my family, including: My grandparents on my mother's side Victoria and Kenneth Ambroise. My grandparents on my father's side Maria and Victor Totpal. My grandparents on my step-father's side, George and Enriqueta Dennett, and all of my extended family through them. My aunt Heather Mitchell and my cousin Chance Mitchell. My uncle Gabriel and aunt Donnie Totpal, and my cousins Michael and Amanda Totpal. My uncle Robert Totpal. You have all inspired

me and believed in me. Thank you all for your unconditional support.

I would also like to thank my best friend and girlfriend, Roopa Sriram. You have been there for me no matter what. Helped inspire me when I needed that optimism. Without your help, understanding, and friendship, this work would not have been possible. I know that at times this degree was probably a lot harder for you than it was for me, so I thank you for your patience, encouragement, and love throughout this journey.

TABLE OF CONTENTS

TABLE OF CONTENTS (Continued)

LIST OF FIGURES

Figure Page

LIST OF FIGURES (Continued)

Figure Page

LIST OF FIGURES (Continued)

Figure Page

LIST OF FIGURES (Continued)

Figure Page

LIST OF TABLES

LIST OF APPENDICES

LIST OF APPENDIX FIGURES

LIST OF APPENDIX FIGURES (Continued)

Figure Page

LIST OF APPENDIX FIGURES (Continued)

Figure Page

LIST OF APPENDIX FIGURES (Continued)

Figure Page

LIST OF APPENDIX TABLES

Table Page

Chapter 1: Introduction

1.1 Background and Motivation

Greenhouse gases emitted from fossil fuel usage have contributed to a 0.89 ± 0.2°C increase in the average land and sea temperature from 1901 to 2012 [53]. According to the United Nations' Intergovernmental Panel on Climate Change (IPCC), the current trajectory of greenhouse gas emissions could result in an increase in global temperature by as high as 5.8°C by 2100 [18]. Consequently, this could result in increased weather extremes such as elevated temperatures or increased precipitation (and thus more natural disasters), as well as significant health related risks stemming from infectious diseases or air-pollution related effects [36]. As such, there is a growing concern of fossil fuel use and its contribution to global climate change, resulting in an increased interest in renewable energy harvesting methods.

An example of this growing interest is shown through the Paris Agreement (November 2016), compiled by the United Nations Framework Convention on Climate Change (UNFCCC). This agreement was signed by 194 of the UNFCCC members as of January 2017 (including the world's top five polluters, China, the United States, the European Union, India, and the Russian Federation), with the pledge to pursue sustainable development of renewable energy sources. According to this agreement, the goal is to limit greenhouse gas emissions such that the global average temperature shall not exceed a 2°C increase over the pre-industrial levels, with 1.5°C being the preferred target [38]. In pursuit of this target, the United States released a strategic plan titled "Mid-Century Strategy for Deep Decarbonization" (in collaboration with Canada and Mexico), where the U.S. targets an 80% reduction from the 2005 greenhouse gas emissions by the year 2050 [19]. A portion of this strategy involves the decarbonizing of the electrical system through implementation of renewable energy sources, nuclear power, and carbon capture methods. Wind energy and hydropower are expected to play a big role in the decarbonization of the electrical grid. Additionally, China is in the process of promoting renewable energy sources through government driven policies, of which wind energy is

expected to play a significant role [13]. The demand for clean energy around the world is clear and drives the motivation of this work, which is to expand the portfolio of hydro and wind power sectors through the use of oscillating foil energy converters (OFECs).

The driving principle of extracting energy using OFECs is based on the flutter motion resulting from fluid (air or water) flow over an immersed foil. Under the correct design conditions, the foil will begin to oscillate, a reaction induced by the on-coming flow. By controlling the proper foil motion (combination of heaving and pitching), significant energy harvesting at high efficiencies can be obtained [28]. As the foil pursues a pitch-plunge motion, the effective velocity of the free stream flow varies with time with respect to the foil frame of reference, imparting oscillating lift and pitching moments on the foil. By aligning the direction of the lift forces and pitching moments with the heaving velocity and rate of pitch of the foil, power may be harvested from the flow.

There are two primary advantages to the application of this method for power generation relative to traditional hydrokinetic and wind turbines as discussed by Zhu [69] and Young et al. [65]. First, the system is versatile and may be implemented in shallow water systems such as rivers or streams as well as larger flow systems such as tidal basins, thus eliminating the need for dams. Dams required for reservoir-style hydropower result in heightened environmental impacts through: the construction of the dam, infrastructure, and access roads; altering the river flow patterns; and the presence of the reservoir itself, which could shift the ecosystem from river-type to lake-type ecology [11]. Additionally, in the case of the Manwan Reservoir Dam in the upper Mekong River in China, the dam has been shown to cause multiple stressors on various wildlife through sedimentation, discharge change, and heavy metal pollution, which have significant impact on Molluska, benthic-feeding fish, and zooplanktivorous fish [6]. Additionally, OFEC systems have the potential to harness new untapped resources more localized to the demand [61]. Second, the large tip speeds of traditional wind turbines result in noisy operation as well as bird and bat mortality [43]. OFEC systems do not require large translational speed, reducing the noise output and minimizing the danger to migratory fish or birds when compared to traditional hydro and wind turbine systems [8]. Also, there is an added advantage of lower stress on the oscillating turbine blade due to reduced tip velocities, compared to traditional rotational turbines, whose tip speeds scale with turbine radius [70]. Because of these reasons, OFEC systems may be a solution to minimizing environmental impact while maintaining efficient power production.

There has been an increased interest in OFEC research in the last decade, as its potential becomes more evident. A number of studies have shown that oscillating rigid foils in the pitch and heave motion can achieve energy extraction on the order of 16.8% to 40% [28, 29, 35, 66], comparable to the 45% achieved with traditional wind turbines [41]. Although there are some experimental investigations on these OFEC systems, many studies utilize numerical efforts (computational fluid dynamics, CFD), and are thus limited to relatively low Reynolds numbers (Re) as they become extremely expensive in terms of time and money for $Re > 1,000$. Although many of these computational studies provide significant insight into the mechanisms of energy extraction for rigid oscillating foils, there is an increased need for physical (experimental) evaluation of these systems. Of particular interest are experimental studies with surface deformation of the oscillating foil.

Inspired from biological lifting surfaces such as bird wings and fish fins, surface deformation has been shown to greatly enhance propulsive efficiencies of oscillating foils, [37, 40, 42, 46–48, 68, 73] to name a few. Because propulsion and energy harvesting applications share several similarities in terms of their operation, there has been heightened interest to incorporate flexible surfaces to OFEC systems. Through computational efforts, some degree of surface flexibility has shown significant improvements in energy extraction efficiencies [17, 33]. Few studies have investigated the flow fields around these OFEC systems experimentally using particle image velocimetry (PIV) [50, 51]. However, to the best of the author's knowledge, there have been no experimental studies for OFEC systems using flexible foils which show performance metrics such as efficiency or power coefficients. This study aims to fulfill this gap by experimentally investigating the contributions of leading edge surface deformation on an OFEC system in order to assess the performance of passive flexibility and its feasibility in enhancing energy harvesting oscillating foil systems.

The objectives of this study are outlined as the following:

1. Develop an understanding of the experimentally measured force trends (and thus energy extraction performance) as they pertain to OFECs operating in the low reduced frequency range ($0.042 \leq k \leq 0.083$).

2. Experimentally investigate the flow fields responsible for the performance of these OFEC systems in the low reduced frequency range ($0.042 \leq k \leq 0.083$).

3. Experimentally investigate the feasibility of inertially-driven, passive surface deformation at the leading edge of the OFEC system operating in the low reduced frequency range ($0.042 \leq k \leq 0.083$).

Note that this range of reduced frequency ($k = fc/U_\infty$) corresponds to systems in which the oscillation frequency and/or foil geometry are constrained such that the time scale of the flow traveling across the foil surface is smaller than the oscillation time scale. In other words, the flow travels the full foil chord length (c) well before the foil completes the motion oscillation cycle. Typical "high" efficiency parameter space has been shown to occur near $0.13 \leq k \leq 0.17$. As such, this study investigates the parameter space in which the flow time scales are even smaller relative to the oscillation time scales, due to experimental (physical) constraints.

1.2 Literature Review

1.2.1 Mechanisms and Performance Metrics of Energy Harvesting

Flapping foil energy harvesting was first explored in 1971 by Wu [59]. In this study, a foil placed near free-surface water waves generated by gravity was shown to utilize the wave energy in order to propel itself forward. Wu determined that it was impossible for this phenomenon to occur in a uniform flow where there is no wave energy available. However, this conclusion was inadvertently challenged in 1981 by McKinney and DeLaurier and their oscillating foil "wingmill" [35]. Through theoretical and experimental investigation, they determined that with the proper heave and pitch motion, along with the proper time delay between the two motions, energy could be harvested from a uniform flow. The driving principle behind this energy harvesting mechanism is through the onset of flow induced instability [69].

As discussed by Peng and Zhu [39], the onset of flow induced instability (similar to airfoil flutter) excites the pitching and heaving motion of a foil supported by a torsion spring in the pitching mode and a damper in the heaving mode. The oscillation of the flow induced by these instabilities impart oscillatory forces on the foil surface. The foil then responds to these forces through fluid-structure interactions and naturally begins to pitch and heave. It is this pitching and heaving motion which extracts energy from the flow, as these motions are induced by the flow energy [32].

This idea is extended into two branches of oscillating foil studies: foil propulsion, and flow energy harvesting. The distinction between these two operating regimes is explained by considering the motion of the foil and the corresponding force vectors [28]. Beginning this discussion, consider the motion of an oscillating foil as a combination of sinusoidal heaving and pitching,

$$h(t) = h_0 sin(2\pi f t + \Phi) \tag{1.1}$$

$$\theta(t) = \theta_0 sin(2\pi f t) \tag{1.2}$$

where $h(t)$ is the instantaneous heaving position, $\theta(t)$ is the instantaneous pitching angle, h_0 and θ_0 are the heaving and pitching amplitudes, f is the oscillation frequency, Φ is the phase delay between the heaving and pitching motions, and t is time. Note that the pitching axis may occur at any point along the foil chord, where x_p (shown in Fig. 1.1) is used to designate the location of the pitching axis from the leading edge of the foil. Additionally, Fig. 1.1 shows the two angles of attack that are at play when the foil pursues these motions. These two angles correspond the the pitching angle $\theta(t)$, and the angle induced by the heaving motion $\theta_h(t)$, where $\theta_h(t) = arctan(2\pi f h(t)/U_\infty)$. In the heave-induced angle, the numerator is essentially the heaving velocity, and the denominator is the free stream velocity. As the foil heaves (vertical translation), there is an induced angle between the foil and the flow due to the apparent flow velocity in the translational direction, in the foil frame of reference. This angle is the heave-induced angle. Thus, the pitching and heave-induced angles set up an effective angle of attack α_{eff} as the following.

$$\alpha_{eff}(t) = \theta(t) - \theta_h(t) \tag{1.3}$$

The nominal (maximum) effective angle of attack is defined by replacing the time dependent terms with their respective amplitudes according to the following equation.

$$\alpha_0 = \theta_0 - \theta_{h_0} \tag{1.4}$$

By taking the ratio of the pitching and heaving angle amplitudes, the feathering parameter χ is established.

$$\chi = \frac{\theta_0}{2\pi f h_0 / U_\infty} \tag{1.5}$$

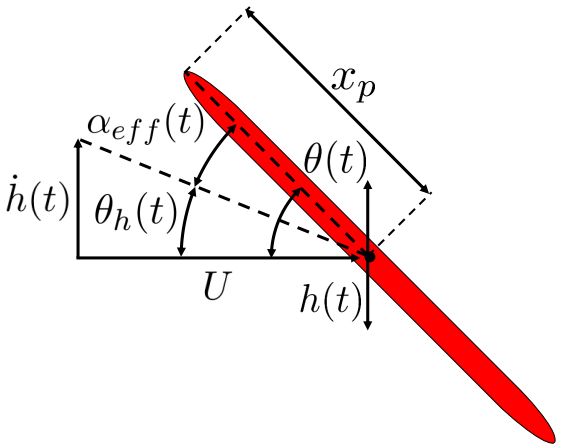

Figure 1.1: Schematic showing an example of oscillating foil motion and relevant angles.

When $\chi = 1$ (also called the feathering limit), the pitching and heaving induced angles are equal and the foil moves through the flow with no effective angle as shown in Fig. 1.2a. As such, no lift forces are generated on the foil and the flow is essentially undisturbed, with the exception of a small drag wake from the foil trailing edge. When $\chi < 1$, the heaving angle plays a dominant role in the effective angle of the foil. When this happens, the resultant force vector acting on the foil contains a component in the positive x-direction as shown in Fig. 1.2b. This enables the foil to propel itself forward in a thrust type application. This mode is not known to occur passively in a uniform stream, and requires input power to drive the foil motion. Thus, the lift force which is also generated acts in a non-energy harvesting mode (lift force aligned opposite the foil motion), which will be discussed later in this section.

Finally, when $\chi > 1$, the apparent trajectory of the foil is that of Fig. 1.2c. In this case, the pitching angle is larger than the heaving induced angle, generating a resultant force in the positive y-direction when the foil moves up, and a negative y-direction lift when the foil moves down. This motion is obtainable in a fully passive situation (as discussed previously by Peng and Zhu [39]), thus yielding energy extraction due to the alignment of the lift force and the foil heaving velocity.

It is now useful to define the power extracted from the flow by the oscillating foil. The power extracted from the flow is determined by the product of the lift force (L) and heaving velocity ($\dot{h}$), added to the product of the pitching moment (M) and the rate of

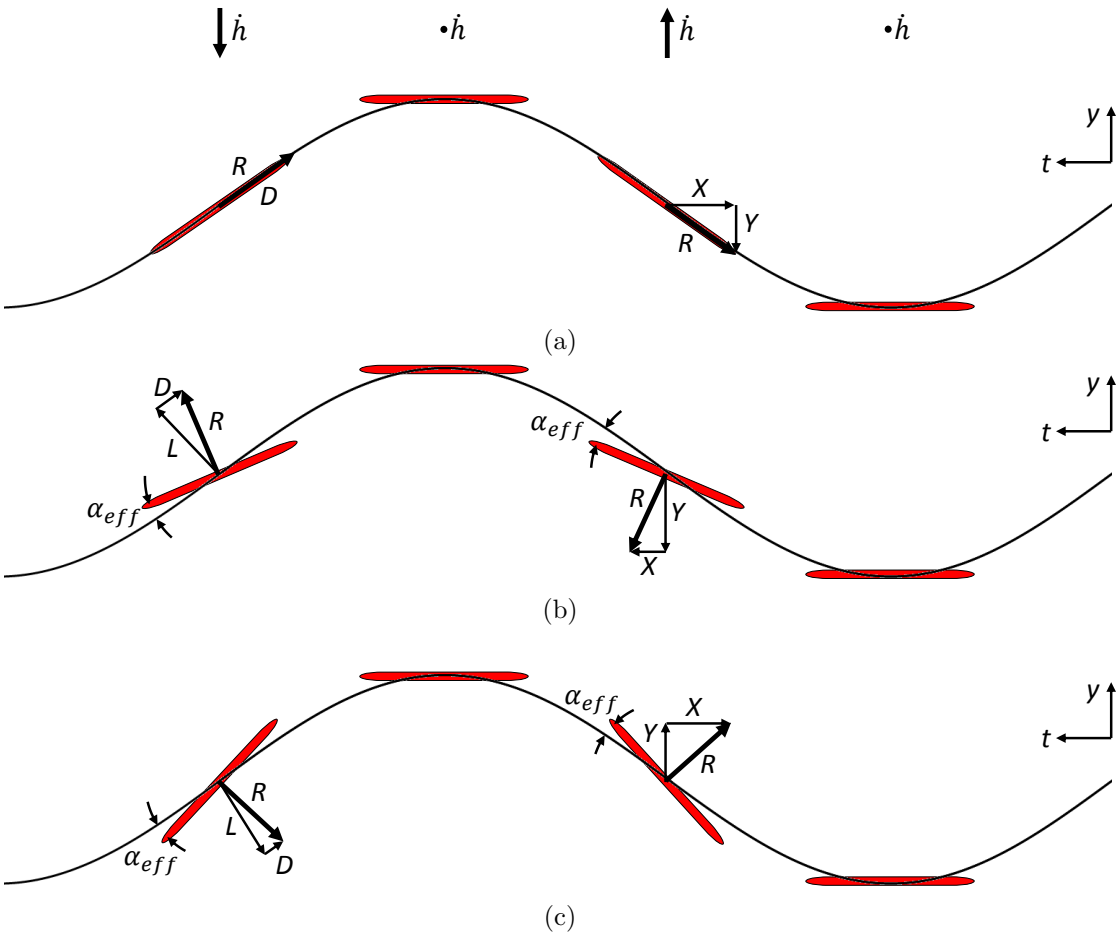

Figure 1.2: Schematic showing the foil trajectory and resulting operating regimes. The sinusoidal curve represents the apparent trajectory of the foil, or the effective flow velocity relative to the foil reference frame. The foil moves from right to left with time. R represents the resultant force acting on the foil, L and D correspond to the lift and drag forces experienced by the foil, while X and Y represent the x and y components of R. The top of (a) shows the heaving velocity of the foil as a reference. The cases shown here correspond to (a) the feathering regime when $\chi = 1$, (b) the propulsion regime when $\chi < 1$, and (c) the energy harvesting regime when $\chi > 1$. This figure is adopted from Kinsey and Dumas [28].

pitch ($\dot{\theta}$) as the following [65].

$$P(t) = L(t)\dot{h}(t) + M(t)\dot{\theta}(t) \tag{1.6}$$

The time averaged power $\bar{P}$ is determined by integrating the power P over the oscillation cycle T.

$$\bar{P} = \frac{1}{T}\int_{t}^{t+T} P(t)dt \tag{1.7}$$

In all studies pertaining to energy harvesting through the use of OFECs, it has been shown that the heaving contribution to the power equation plays a dominant role over the pitching contribution. Additionally, many studies show that the pitching term, in a cycle averaged sense, shows near negligible contribution to energy harvesting over a wide range of parameters. As such, many studies neglect the contributions due to the pitching motion in order to simplify the problem [28, 52, 60]. The reason for this is discussed in more detail in Section 1.2.2.

In order to assess the performance of energy extraction, two main parameters are used. These parameters include the power coefficient C_P, which is a measure of the power extracted by the foil, as well as the energy extraction efficiency η, which is a measure of the extracted power divided by the power available from the flow within the foil swept area. These parameters are shown below.

$$C_P = \frac{\bar{P}}{\frac{1}{2}\rho U_\infty^3 sc} \tag{1.8}$$

$$\eta = \frac{\bar{P}}{P_a} \tag{1.9}$$

where P_a is the available flow power, ρ is the fluid density, and s and c are the foil span and chord, respectively. For the available flow energy P_a, there are four definitions typically used [26]. These four definitions for the available power in the flow include:

1. $P_a = \frac{1}{2}\rho U_\infty^3 sd$
2. $P_a = \frac{1}{2}\rho U_\infty^3 s(2h_0)$
3. $P_a = \frac{1}{2}\rho U_\infty^3 sd(\frac{16}{27})$

4. $P_a = \frac{1}{2}\rho U_\infty^3 s(2h_0)(\frac{16}{27})$

where d is the total swept height of the foil throughout the flapping window, and the term $\frac{16}{27}$ is the Betz limit, which is the maximum amount of energy that is possible to extract from the flow using actuator disk theory [5]. These definitions result in vastly different efficiency values, and care must be taken when comparing efficiency results across studies. In an example provided by Kinsey and Dumas [26], these definitions applied to data in [28] result in the following efficiencies: 1) 33.7%, 2) 43.0%, 3) 56.9%, and 4) 72.6%.

1.2.2 The Role of the Leading Edge Vortex (LEV)

Leading edge vortices (LEVs) have been shown to provide a significant increase in lift forces acting on oscillating foils operating in the propulsion regimes [37, 40, 42, 46–48, 68, 73]. This phenomenon was first discovered in insect flight by Ellington et al. in 1996, where flow visualization around a hawkmoth wing in flight showed massive aerodynamic separation coinciding with high lift generation during the flapping motion [12]. Since then, a large amount of studies have investigated the role of this LEV as it pertains to flapping wing propulsion.

This increase in lift force is the direct result of the increased pressure differential across the the upper and lower surfaces of the foil, stemming from the low pressure of the separation bubble vortex core [49]. As the foil oscillates in both pitch and heave, the elevated forces are utilized dynamically such that the foil takes advantage of the increased lift without reaching a fully stalled condition. This same concept is applied to energy harvesting applications in order to generate enhanced lift, and thus, increase their energy harvesting performance.

The LEV has been believed to be an integral part of oscillating foil energy harvesting as it has been shown to provide an increase in lift throughout key points in the oscillation cycle. Beginning with the pioneering work of McKinney and Delaurier, their experimental results showed that lift dominates the energy harvesting performance of an oscillating foil operating at a nominal effective angle of attack of 15.5°, far exceeding the static stall angle of the foil (around 10°) [35]. Coincidentally, their theoretical approach, which was based on an attached flow assumption, consistently under-predicted their experimental results ($\eta = 16.8\%$) for the energy harvesting performance. This was later found to be

attributed to the dynamic flow separation, or LEV.

In 1999, Davids used an unsteady panel code in order to investigate the various operating parameters and their effect on OFEC performance [7]. In part of his analysis, Davids compared his results to the experimental results of McKinney and Delaurier. He found that at lower angles of attack ($\theta_0 = 25°$), his panel code consistently over-predicted η for Φ between 60° and 120°, which was likely attributed to mechanical losses in the experimental measurements. However, his results greatly under-predicted η when $\theta_0 = 30°$ and $\Phi > 90°$. In his discussion, Davids described this as a consequence of the onset of dynamic stall (LEV) in the experimental results. The optimal operating point in his work was found to be at $k = 0.31$, $h_0/c = 0.625$, $\theta_0 = 94°$, $x_p/c = 0.55$, and $\Phi = 94°$, with an efficiency of 31%.

Jones et al. expanded the work of Davids [7] through additional inviscid simulations, viscid computations, and experiments [24]. The numerical simulations were solved using an incompressible two-dimensional inviscid panel code as well as a two-dimensional Navier-Stokes viscid solver for two different Reynolds numbers, $Re = 2 \times 10^4$ and 1×10^6. Using the panel code, C_P and η contour maps were generated in the $k - h_0/c$ parameter space for $80° \leq \Phi \leq 110°$. It was determined that, by neglecting flow separation, peak C_P tends towards high h_0/c and low k for $\Phi = 80°$, and low h_0/c and high k for $\Phi = 110°$ in a nearly linear fashion. However, peak efficiency was fairly stable near low heaving amplitudes of $h_0/c = 1$ to 1.75, with higher k. These results are almost identical to those of Shimizu et al., where they used a multi objective optimization algorithm in order to maximize the values of η and C_P in an energy extraction mode [45]. In their study, peak efficiencies were obtained near higher frequencies with low heaving amplitudes, and peak power generation was found near higher heaving amplitudes but lower frequencies. Shimizu et al. also found that the presence on an LEV increased the overall efficiency by up to 36.6%, obtaining a maximum efficiency of $\eta = 29\%$.

A comparison was then performed by Jones et al. between their panel code and their viscid Navier-Stokes solver for a NACA 0014 airfoil operating at $x_p/c = 0.25$, $\theta_0 = 73°$, $h_0/c = 1.3$, and $\Phi = 90°$ [24]. They found that the dynamic flow separation caused a large increase in C_P for k between 0.08 and 0.19 for the $Re = 1 \times 10^6$ case, and is critical to high power generation. Additionally, the LEV was found to convect towards the trailing edge when the foil was changing its angle of attack, providing a favorable pressure gradient and thus assisting the pitching motion. Interestingly, their viscid code results

severely over-predicted the performance of the experimental apparatus. The authors of that paper express several possible reasons for this, including three dimensional flow contributions as well as mechanical losses in the system which were not accounted for.

Kinsey and Dumas investigated the performance of an OFEC system using an unsteady two-dimensional laminar-flow code in the commercial software FLUENT [28]. In their simulations, the LEV was also found to increase lift forces throughout the foil oscillation cycle. In addition to the increased lift force, they found that the lift forces were delayed to later times in the cycle, resulting in increased synchronization between lift and the heaving velocity of the foil. The combination of increased sustained lift and the proper synchronization of lift with the heaving motion resulted in significantly higher efficiencies of energy extraction. Comparing a test case where no LEV was present and a case where an LEV was detected, the efficiency of energy extraction increased from $\eta = 11\%$ to 34%. Kinsey and Dumas also note that a small increase in pitching moment can be beneficial with a well timed LEV, however for simplicity, the $M(t)\dot{\theta}(t)$ term can be considered negligible when averaged over a period for $k \leq 0.16$. For many cases at $k \leq 0.16$, the LEV detaches itself from the foil surface before reaching the trailing edge, thus the LEV does not provide a favorable pitching moment when the foil changes its pitching angle. In order to achieve increased energy harvesting through pitching moment contributions, the LEV would need to form at the leading edge surface as the foil increases its pitching angle, and maintain attachment near the trailing edge as the pitching angle is decreased. This would yield a positive net contribution of the pitching term over the oscillation cycle.

1.2.3 Implementation Methods

There are three methods of implementation used in oscillating foil energy harvesting studies: fully prescribed motion, semi-passive motion, and fully passive motion. This section provides a broad overview of the work that has been done on these three methods. For the fully prescribed method, both the pitching and heaving motions are driven motions. The intention for studies on fully driven systems is to investigate the parameter space and provide insight into the design of actual systems. In semi-passive systems, the pitching motion is actively controlled allowing the heaving mode to respond to the fluid structure interaction. These systems are capable of extracting net energy so long as the

heaving mode extracts more energy than what is required to drive the pitching mode. With a fully passive system, the pitching and heaving components respond to the flow induced vibrations and no part of the system requires input power. These systems typically include a system of springs and dampers or mechanically-constrained motion trajectories such that the foil pursues periodic motion passively.

Fully Prescribed. A significant number of studies use fully prescribed methods to generate the foil motion [7, 24, 26, 28]. These systems are useful to understand the contributions of each parameter relevant to OFEC systems in order to better their design. Peak energy extraction performance for the fully prescribed motions result in η ranging from 20% to 43% for $0.1 \leq k \leq 0.2$. These efficiencies are generally found near heaving amplitudes of h_0/c near 1, and larger pitching amplitudes of $\theta_0 \geq 65°$. Many fully prescribed motion studies have already been discussed in Section 1.2.2 and will not be discussed further here.

Semi-Passive. Typical studies involving semi-passive motion involve active control of the pitching mode, allowing the heaving mode to passively respond to the fluid loading [1,20,45,71,72]. In these systems, a generator (damper) is attached to the foil in the heave mode, by which the amount of extracted energy can be measured. A new parameter is now introduced, the damping coefficient, which greatly influences the OFEC performance [1]. Therefore, these systems contain a different response than those of the fully controlled method, as the heaving motion becomes a function of the pitching motion and the damping coefficient. Generally there exists a trade-off between the amount of energy harvested and its efficiency in the semi-passive system [1,45]. This is because the amount of energy harvested increases with the heave amplitude, which in turn decreases the efficiency as the amount of available power in the flow increases proportionally with h_0/c. Typical efficiencies in this operation mode range from 23.8% to 34% [1, 9, 20, 45, 54].

Deng et al. investigated the inertial effects on the semi-passive OFEC system using OpenFOAM [9]. In this study, the mass ratio ($r = \rho_{foil}/\rho_{fluid}$) was varied from 0.125 to 100 for a NACA0015 foil with the pitching axis at $x_P = 1/3$. For their baseline case where $r = 1$, an efficiency map in the $k - \theta_0$ space was determined where k ranged from 0.08 to 0.22 and θ_0 was varied from 60° to 90°. An optimal efficiency of $\eta = 34\%$ was obtained for $k = 0.16$ and $\theta_0 = 75°$, similar to that of [28]. When the mass ratio was

varied, C_P remained fairly constant with a 5.2% increase in C_P up to $r = 10$, thereafter quickly plummeting. On the other hand, the efficiency monotonically decreased with any increase in r, with an 11.8% reduction in η between $r = 1$ and 10. However, the effects of the moment of inertia were not considered, which were determined to play an important role in fully passive systems by Zhu [70] and Young et al. [64], and thus may also be important in the semi-passive implementation. Additionally, according to Zhu and Peng [72], the LEV has significant contributions on the pitching moment for semi-passive systems and thus the pitching axis should be placed near the center of pressure. The moment of inertia could have an impact on this result.

In 2017, Zhan et al. investigated the contributions of wind gusts on the energy harvesting performance of a semi-passive system in order to understand how these systems perform in non-uniform flows [67] using the commercial software FLUENT. This study used a spring and damper system in the heaving mode, which were mounted at the pitching axis ($x_P/c = 1/3$). By neglecting the foil mass, the semi-passive response of the system was investigated under both uniform and gusty free stream conditions. The gusty flow condition was achieved by varying the free stream velocity amplitude cosinusoidally as the following: $U(t) = U_{avg}(1 + A\cos 2\pi ft + \phi)$, where A is the gust amplitude and ϕ is the phase shift between the pitching motion and the flow gust. It was determined that the larger the gust amplitude, the more efficient the system operated (η determined using the average flow speed U_{avg}). When $A = 0.2$ and $\phi = 180°$, η increased from 27.4% to 31.9% and C_P increased from 0.33 to 0.39 for the gusty flow versus the uniform flow condition. This was due to elevated lift forces with minimal change in the heaving amplitude, which keeps the available flow power nearly constant. Therefore semi passive systems may be beneficial in gusty environments, however these conclusions need to be explored more.

Fully Passive. Using a Navier-Stokes solver, Peng and Zhu [39] investigated a fully passive OFEC system. In order to generate the fully passive motion, a damper was placed in the heave mode with a torsion spring in the pitch mode. The motion is then induced by the flow instabilities and the fluid-structure interaction, and is dependent on the location of the pitching axis and the stiffness of the torsion spring. As a result, four possible responses occur; no movement, periodic pitching and heaving with the average pitching angle $\bar{\theta_0} = 0°$, irregular motion due to competition between modes, and

motion about a non-zero $\bar{\theta_0}$. When the second response occurs, the system is capable of extracting energy with up to 18% to 20% efficiency, comparable to that of the fully passive system numerically investigated by Young et al. ($\eta = 17.8\%$) [64]. This mode occurs when the pitching axis is near the center of the foil ($0.4 \leq x_P/c \leq 0.5$). An extension of this work was performed by Zhu [70] in which the foil was subject to a shear flow, representative of the flow conditions where these systems are deployed in shallow rivers or streams. In this situation, the above motions were observed in addition to a tumbling motion in which the foil continuously rotates, as well as completely irregular motion. The contributions of the moment of inertia were also included in a portion of the study. Zhu's results showed that higher efficiency and power were obtained when the foil was modeled with the mass located near the leading edge, effectively increasing the foil moment of inertia. In addition, higher efficiency was achieved when the foil mass was considerably less than the fluid it displaced. This increase in efficiency is a result of the decrease in oscillation frequency and an increase in the pitch angle, which are related to the most unstable wake mode discussed in Zhu [69].

1.2.4 Relevant Parameters

There are a wide range of parameters relevant to OFEC systems making them complicated to compare across different studies. As such, this section aims to clarify the role of each key parameter in order to ease cross-study discussion. This section is divided according to the relevant geometric parameters (Section 1.2.4.1) as well as kinematic parameters (Section 1.2.4.2).

1.2.4.1 Geometric Parameters

Foil Thickness. In 2002, Lindsey investigated the effects of foil thickness of three NACA foils (0010, 0014, 0018) on the energy harvesting performance of OFEC systems using an unsteady panel code [32]. He found that as the foil thickness decreased, efficiency increased from 23% to 28%. However, the use of the unsteady panel method did not allow for flow separation from the leading edge, which could change these results. Kinsey and Dumas performed a similar study in which they tested NACA0002, 0015, and 0020 foils using an unsteady two-dimensional Navier-Stokes code in FLUENT. It

was found that the foil thickness had a weak influence on the overall performance, with efficiencies ranging from 31.8% to 33.7%. Although the thinner foils showed increased peak lift forces, the timing of the peak forces were slightly out of synchronization with the foil motion resulting in similar performance when averaged over the cycle. This is also consistent with [71], where negligible changes in system performance were found at reduced frequencies below 0.35 across NACA0005 and 0025 foils.

Additionally, Usoh et al. found that decreases in thickness for a flat plate foil also showed nearly negligible influence on the energy extraction performance [57]. However, they found that a rectangular cross-section ($\eta = 34.3\%$) had a 5.4% larger efficiency than a NACA0012 foil ($\eta = 32.5\%$) with the same cross-sectional area operating at $Re = 1,100$, $x_P/c = 1/3$, and $h_0/c = 1$. This was attributed to the promotion of LEV formation for the rectangular cross-section, providing a beneficial interaction with the trailing edge of the foil. Thus simple rectangular foils may prove to be more practical for implementation due to increased performance with decreased manufacturing costs.

Aspect Ratio. Foil aspect ratio has been shown to have a significant effect on the energy extraction performance. By experimentally testing NACA0012 foils of aspect ratio $AR = 7.9$, 5.9, and 4.1, Simpson et al. showed an abrupt decrease in efficiency of $\eta = 43\%$, 29%, and 17%, respectively [52]. Zhu et al. also showed a decrease in performance between foils with $AR = 10$ and 2 [71], although not as dramatic as Simpson et al. [52].

The effects of three-dimensionality (3D) are also increased as the Reynolds number increases. According to Deng et al., 3D effects are very weak at $Re = 1,100$, and the performance is very similar to that of two-dimensional (2D) flow [8]. The 2D flow case results in the highest performance, due to the increased secondary peak in the force traces. As the flow becomes more 3D, the secondary peak in the force trends significantly decreases resulting in the loss of energy extraction performance. The critical foil aspect ratio was determined to be around $AR = 4$, due to decreased performance sensitivity above this aspect ratio. For low aspect ratios, the LEV is overall weaker and further away from the foil surface at any given time in the oscillation cycle compared to its two-dimensional counter part. At larger AR, the LEV is much stronger and closer to the foil surface, increasing the overall forces and thus increasing the energy extraction performance. However, some 3D effects are still shown for AR up to 8. This is similar

to the experimental results of Abiru and Yoshitake [1], where $\eta = 32\%$ when the foil $AR = 3$, and $\eta = 37\%$ when end-plates were used on a semi-passive system.

Kinsey and Dumas performed simulations using an unsteady Reynolds-averaged Navier-Stokes code for a range of foil aspect ratios [31] at $Re = 500,000$. These 2D simulations showed roughly 15% larger efficiencies over an $AR = 7$ foil, and increased performance over the entire range of k tested $(0.04 - 0.20)$. They also found that at lower k, 3D effects were reduced. These results showed excellent agreement with their experimental prototype testing conducted in [27]. Further tests were conducted by Kinsey and Dumas in [31]. Computational simulations were conducted for the 2D case, as well as 3D cases where $AR = 5$ and 7 with no end-plates, and $AR = 5$, 7, and 10 with end-plates. Their results showed that 2D simulations showed the highest performance, with $\eta = 38.7\%$. When no end-plates were used, foils with $AR = 7$ and 5 had efficiencies of 30.4% (21% lower than 2D) and 27.9% (28% lower than 2D), respectively. The addition of end-plates significantly improved performance, however, foils with AR up to 10 still showed a 10% decrease in extraction efficiency as compared to the purely 2D results.

Pitching Axis. The effects of pitching axis location on the performance of OFEC systems has been extensively investigated by a number of groups. However, many papers agree that operating at $x_P = 1/3$ yields the optimal energy extraction efficiency [7,28,33, 54,69]. This is largely due to the timing of the formation of the LEV, which is directly related to the location of the pitching axis. In fact, it has been shown that the pitching axis location shows slightly more influence on the energy extraction performance than the motion phase due to the amplified forces which result from changing the pitching axis location [28]. For pitching centers closer to the leading edge, vortices are shed from the leading edge at earlier times. When the pitching axis is located near the center of the foil, LEV formation and shedding is delayed.

However, for semi-passive and fully-passive systems, the flow induced instabilities seem to initiate the proper pitching and heaving motion desired for efficient energy extraction when the pitching axis is located near the mid-chord [39,64,71,72].

1.2.4.2 Kinematic Parameters

Heaving Amplitude. In general, there exists a trade-off between energy extraction and efficiency as the heaving amplitude is increased. Heaving amplitudes comparable to the foil chord ($h_0/c \approx 1$) yield optimal energy extraction efficiency, while further increases in h_0 result in increased power performance [7, 23, 28, 32, 60]. Additionally, as the heaving amplitude is increased, peak performance has been shown to tend toward lower k and higher θ_0 [26]. This stems from the need of the feathering parameter χ to be greater than 1, which is dependent on the heaving velocity and the pitching amplitude. Thus, Kinsey and Dumas argue that the effective angle of attack α_{eff} may be a more important parameter to use as it incorporates both h_0 and θ_0 [28]. Similar trends were discussed by Zhu [69], where peak efficiency tends towards increased pitching angles as the heaving amplitude is increased. In this study, Zhu also mentions that the effects of the phase ϕ becomes less influential on the overall performance for $h_0/c \leq 1$. In Kinsey and Dumas [26], a model was developed based on turbulent flow simulations at $Re = 500,000$ that predicts the performance of OFEC systems using h_0/c as an input variable.

Pitching Amplitude. In order to operate in the energy extraction regime, the pitching angle must exceed that induced by the heaving motion (see Section 1.2.1) [22]. Because of this, the pitching angle is a fairly important parameter in OFEC studies. Efficiencies as high as 32% to 34% have been obtained for systems with pitching angles between $70° \leq \theta_0 \leq 80°$ and reduced frequency between $0.12 \leq k \leq 0.18$ [28, 54]. Teng et al. [54] and Kinsey and Dumas [26] found that more energy was extracted with larger pitching angles. Additionally, the model developed by Kinsey and Dumas [26] shows that for the range of $0.50 \leq h_0/c \leq 3$, high efficiencies were obtained with pitching angles ranging from $65.4° \leq \theta_0 \leq 98.4°$. For semi-passive systems, higher pitching angles also showed increase energy extraction performance and efficiency [1, 71, 72].

The need for high pitching angles is explained using the unstable wake modes investigated by Zhu [69]. At low θ_0, the wake instability frequencies are 7 to 17 times larger than the oscillation frequency for $0.05 \leq k \leq 0.21$. However, at sufficiently large θ_0, the wake instability frequency approaches that of the oscillation frequency of the foil creating a resonant effect in the energy transfer.

Motion Phase. The phase relationship between the pitching and heaving motions has been shown to control the timing of the LEV development throughout the cycle. Optimal phase has been determined to be near $\phi = 90°$, as this allows for a favorable timing between the lift force and heaving velocity of the foil resulting in higher power performance [2, 24]. Ashraf et al. also noted that at $\phi = 90°$, the lift force acting on the foil was more sustained throughout the oscillation cycle, which also contributes positively to power extraction [2]. Additionally, a naturally occurring phase shift of 90° has been shown for semi-passive systems, alluding that this may be the optimal delay [1]. However, it has been shown that the energy extraction efficiency is somewhat insensitive to ϕ over a narrow band of phase delays between 80° and 100° [24], particularly at low heaving amplitudes ($h_0/c = 0.5$) [69].

Effective Angle of Attack. The effective angle of attack combines the contributions of the heaving amplitude, pitching amplitude, and oscillation frequency into a single term (see Eq. 1.3). With sufficiently high effective angle of attack, the onset of LEV formation is more likely to occur due to the decrease in the unstable wake frequency [69]. According to Zhu, when α_{eff} approaches 40°, the unstable wake frequency is equal to the oscillation frequency, resulting in optimal energy extraction performance [69]. Kinsey and Dumas also showed that similar trends can be seen across different combinations of operating parameters that result in similar α_{eff} [28]. As such, Young et al. as well as Kinsey and Dumas note that controlling the effective angle of attack is advantageous over controlling the pitching amplitude, resulting in increased sustained lift forces along the foil and thus better energy harvesting performance [28, 64].

Reduced Frequency. The reduced frequency represents the dimensionless frequency that the OFEC operates at. Peak energy extraction efficiencies have been reported for reduced frequencies in the range of $0.15 \leq k \leq 0.17$ in many studies [23, 26, 28, 54, 69]. In this range of k, the magnitude of the foil heaving velocity is comparable to the free stream flow speed, resulting in near maximum α_{eff} [28]. Peak efficiency is obtained at these k because of the unstable wake frequency discussed in Zhu [69]. When $k \approx 0.15$, the oscillation frequency is approximately equal to the unstable wake frequency, resulting in favorable timing between the lift forces and the foil motion, as well as sustained increased lift forces throughout each half cycle. However, as h_0/c is increased, peak η

occurs towards decreasing k, and vice versa [26].

Reynolds Number. Due to the limitation of computational methods, many numerical studies have focused on Reynolds number near $Re = 1,000$ to $1,100$ [22, 28, 69]. As turbulence models have become more widely used in these types of applications, few studies have investigated the performance of OFEC systems numerically at $Re = 500,000$ [26, 30]. Experimentally, these devices have been tested in a wide range of Re, ranging from $10,000$ to $500,000$ [1,27]. Kinsey and Dumas [28] showed that by increasing Re from $1,100$ to $10,000$, slightly larger forces were measured but overall, no significant changes occur in the energy extraction performance. This is similar to Jones et al. [22], where the effects of Re from $1,100$ to $20,000$ were virtually the same. However, Dumas and Kinsey [10] showed an increase in efficiency from 32.7% to 35.9% as Re was increased from 500 to $2,400$. In 2008, Kinsey and Dumas conducted further Reynolds number testing, ranging Re from 500 to $10,000$ [28]. Across this range, efficiency only increased from 32.7% to 36.4%. Kinsey and Dumas [26] also showed that an increase in Re from $1,100$ to $500,000$ steadily increased the overall performance in the $k-\theta_0$ parameter space tested. These findings were interpreted to be a result of a reduction in the effective foil thickness due to reduced viscous diffusion at high Re, thus increasing lift generation [61].

1.2.5 Enhancement Mechanisms

In more recent years, attention has shifted towards enhancement strategies aimed at increasing the energy extraction capabilities of OFEC systems. By considering the power equation (Eq. 1.6), increasing the amount of energy extracted by the foil occurs in several ways. These methods include increasing the lift or heaving velocity such that the product $L(t)\dot{h}(t)$ is increased, or increasing the pitching moment or rate of pitch such that the product $M(t)\dot{\theta}(t)$ is increased with little or no decrease in the other terms. In the previous sections, it has been shown that larger effective angles of attack yield higher extraction performance through elevated and sustained lift forces, as well as favorable LEV interaction with the trailing edge. As such, enhancement methods seek to increase the effective foil angle over the duration of the oscillation cycle. In order to accomplish this, methods include utilizing non-sinusoidal pitching trajectories as well as incorporating a degree of surface deformation. This section investigates the studies conducted on

these enhancement mechanisms and discusses opportunities for further studies.

1.2.5.1 Non-Sinusoidal Motions

Ashraf et al. showed that through a non-sinusoidal pitch and heave motion, the energy extraction and efficiency increased by 17% and 15%, respectively for stroke reversal time of $\Delta T_R = 0.3$ over purely sinusoidal motion [2]. The stroke reversal time is a measure of time in which the motion changes or "reverses" direction, where $\Delta T_R = 0.5$ corresponds to fully sinusoidal motion, and $\Delta T_R = 0.1$ corresponds to swift directionality change, where the foil completely changes direction within 1/10 of a cycle period. The non-sinusoidal motion, achieved through stretching the sinusoidal motion into a trapezoidal shape, was shown to increase the performance by holding the maximum effective angle of attack for a longer duration of the cycle.

Xiao et al. investigated the effects of non-sinusoidal pitching motion (sinusoidal heaving) where a parameter β is used to impose a trapezoidal pitching motion on sinusoidal motion [60]. In this work, as β increases from 1 to ∞, the pitching profile transitions from purely sinusoidal to purely square. It was shown that, for $\beta = 1.25$ to 2, there is increased energy extraction and efficiency over a purely sinusoidal wave due to sustained elevated lift forces. When $\beta = 1.5$, there is a 72% increase in C_P over $\beta = 1$ (C_P increases to 0.62 from 0.36). However, severe performance degradation is seen when the pitching motion becomes too square (i.e. $\beta > 2$). Although there are increased peak forces when $\beta > 2$, the increase in lift is far outweighed by the amount of power required to quickly reverse the pitch of the foil. Similar results were obtained by Young et al., who notes that the rapid pitching angle change results in the formation of a vortex that opposes the foil motion, thus decreasing the net power extracted [64]. Deng et al. also investigated similar pitch profiles and determined that, although a slight degree of non-sinusoidal motion is beneficial, the effect is more favorable for lower pitch angles [8]. In their study, increasing β from 1 to 2 showed a 114% increase in efficiency ($\eta = 7\%$ versus 22%) when $\theta_0 = 60.7°$, but only a 6% increase in efficiency ($\eta = 34\%$ versus 36%) by increasing β from 1 to 1.15 when $\theta = 81.5°$. These values of β correspond to the highest efficiency for each θ_0. Teng et al [54] also obtained similar results, where near optimal conditions (large θ_0), changing the pitching profile towards a square wave did not have a significant influence on the overall performance. They also found that altering the pitching profile

was more beneficial at smaller θ_0. When $\theta_0 = 45°$, increasing β from 1 to 1.5 results in a 16.5% increase in efficiency, with a maximum efficiency of 32%.

A modified pitching profile governed by the motion $\theta(t) = \frac{\pi}{2} + \theta_0 \sin(2\pi ft + \Phi)$ was investigated by Xie [62], resulting in increased α_{eff} near the top and bottom heaving positions. It was found that for this modified motion, the pitching contributions to energy extraction were near zero, and the maximum efficiency obtained was $\eta = 24\%$. This pitching profile results in peak efficiencies for small θ_0 (10°) and large k (0.32), or larger θ_0 (25°) and smaller k (0.13). The appeal to this type of motion is that the η and C_P maps have identical shapes (different magnitudes) due to the constant heaving amplitude.

A swing arm type motion was investigated by [25], where the foil heave motion is obtained by mounting the foil on the end of a pivoting radius. The heaving amplitude, pitching amplitude, and Reynolds numbers were held fixed at $h_0/c = 1.25$, $\theta_0 = 70°$, and $Re = 100,000$. With some degree of swing arm motion, the peak energy extraction efficiency at $k = 0.08$ is roughly 20% while 18% for the purely sinusoidal motion (no swing arm). This small increase in efficiency is attributed to increased local Re and α_{eff}, changing the LEV growth and detachment time. The LEV detachment time is delayed, resulting in more favorable power generation and efficiency near lower k.

1.2.5.2 Surface Flexibility

Inspired through biomimetics, foil flexibility in propulsion systems have been shown to increase lift forces acting on oscillating foils [14,15,63]. This idea has been extended into OFEC applications, with intent to enhance energy extraction capabilities. In this section, the limited work performed in flexible foil OFEC systems is presented and split into two parts. These two parts consist of the work performed using controlled (driven) surface deformation, and purely passive surface deformation resulting from fluid-structure interactions or foil inertia.

Controlled. Using computational modeling, Liu et al. [33] investigated the performance of a flexible foil operating in the energy extraction regime. In this study, surface flexibility was determined a priori under three conditions: leading edge control (LEC), trailing edge control (TEC), and combined leading and trailing edge control (LTEC).

The timing of the flexible edges was such that an increased local angle attack (from the foil pitching angle) was generated with a maximum local deflection when the pitching angle was also maximum. It was determined that LEC resulted in a roughly 40% increase in performance ($\eta_{rigid} = 16.2\%$, $\eta_{LEC} = 22.5\%$) when $h_0/c = 1$. For TEC and LTEC, the performance increased by 75% ($\eta = 28.4\%$) and 60% ($\eta = 26\%$), respectively, over the rigid foil. These results were even more profound at low $h_0/c = 0.5$, where efficiencies were: $\eta_{rigid} = 12.5\%$, $\eta_{LEC} = 19\%$, $\eta_{TEC} = 21.9\%$, $\eta_{LTEC} = 22\%$. LEC was found to control the timing of the LEV allowing the LEV to develop earlier in the cycle, and TEC was found to control the size and strength of the LEV, increasing overall loads. Additionally, too much flexibility resulted in decreased performance, showing that the degree of flexibility is also important.

Using a thin flat plate, Tian et al. [55] performed numerical simulations using a Navier-Stokes solver for $h_0/c = 1$, $X_P = 1/3$, $\Phi = 90$, $k = 0.14$, and $\theta_0 = 76.3°$. In their simulations, they compared the performance of a rigid plate to a passively flexible plate, a passively flexible leading segment, and a controlled flexible plate. The results of the passive flexibility simulations will be discussed in the next section. The rigid foil showed an efficiency of 33.4% with a power coefficient of 0.856. Additionally, the leading segment of the foil, which is only 1/3 of the chord, extracted 47% of the total power harvested by the foil. This shows that the leading portion of the foil plays a vital role in the energy extraction process of OFEC systems. As such, controlled flexibility at the leading edge was implemented. Controlled leading edge flexibility showed a 11.3% larger C_P and η over the rigid foil, with $\eta = 38.2\%$. This was attributed to the flexible leading edge stabilizing the LEV, keeping it attached to the foil surface for a prolonged period of time throughout the oscillation cycle.

Hoke et al. investigated the contributions of surface deformation on the energy extraction performance of an oscillating foil [16]. In their Navier-Stokes simulations, flexibility was achieved through camber displacement, where the leading and trailing edge positions were fixed and chord centerline is displaced at the pitching axis. Using a maximum deflection distance of $0.1c$ from the rigid centerline, the optimal phase between the controlled flexibility and the pitching motion is $\phi_{camber} = -135°$. The efficiency of energy extraction using this approach increased from 32.9% for the rigid case to 38.1% for the flexible case (15.8% increase). With the controlled surface deformation at $\phi_{camber} = 135°$, there was an increase in sustained lift force throughout the cycle, although the

maximum lift in this case was not the largest lift observed. Thus the contributions of surface flexibility showed increases in performance by increasing the time that the LEV interacts with the foil, not necessarily by increasing force magnitudes through stronger LEVs. Using the flywheel-linkage approach of Young et al. [64] to achieve passive foil motion, Hoke et al. also investigated the contributions of controlled surface deformation of a passively-oscillating foil. It was shown that the extraction efficiency was much more sensitive to varying ϕ_{camber}, where ϕ_{camber} which results in increased performance correspond to the cases of highest flapping frequency. Additionally, the pitching mode of energy extraction had an increased contribution due to the proper LEV convection timing that interacts with the trailing edge. For the passive system, flexibility was shown to increase performance by nearly 13% over the rigid case.

Passive. In the work of Tian et al. [55] discussed above, the contributions of fully-passive flexibility were also investigated. Using flexible leading and trailing segments of the thin plate, it was found that the overall energy extraction efficiency was 9.4% less ($\eta = 30.2\%$) than that of a rigid plate. By looking at the force contributions from the leading and trailing segments of the plate, the leading segment contributed 30% higher power ($C_{P,L} = 0.520$) than the rigid configuration, however the overall C_P was 4% less. When a passively-flexible leading edge and a rigid trailing edge was used, the performance was similar to that of a rigid plate with $\eta = 33.7\%$ and $C_P = 0.864$. In this case, the flow fields were very similar between flexible leading edge and rigid configurations, suggesting that the trailing edge deformation has a significant impact of OFEC performance and the leading edge does not have a significant contribution.

More recently, Liu et al. [34] performed an extension of their previous work [33], where computational simulations including passive surface deformation at the trailing edge were conducted through coupling of fluid-structure interactions. The heaving and pitching motions were imposed motions with $h_0/c = 1$, $x_P = 1/4$, $\Phi = 90°$, and $\theta_0 = 60°$ and 73°. It was found that trailing edge deformation shows greatly enhanced performance at $k = 0.15$, with positive contributions in the range of $0.1 \leq k \leq 0.25$. The surface flexibility increased peak loads, as well as incurring a small phase shift in the force history. As a result, the pitching moment of the foil was reduced, such that less input power was required to generate the foil motion. Furthermore, tests were conducted to assess performance contributions for several different degrees of flexibility using two

methods; increasing Young's modulus coefficients from 8.15×10^7 to 1.02×10^9 (decreasing flexibility) for a fixed density ratio ($\rho_{foil}/\rho_{fluid} = 8.9$), as well as changing the density ratio from 7 to 1500 for a fixed Young's modulus coefficient (1.12×10^8). By varying the Young's modulus such that the degree of flexibility is decreased, the energy extraction performance decreases and approaches the results of the rigid foil. By increasing the density ratio, the deflection becomes more inertially dominant (for density ratio above 116) and as such more sinusoidal with a frequency approaching the oscillation frequency. It was shown that lower density ratios result in increased energy extraction performance as the LEV remains attached to the foil surface longer, and interacts favorably with the trailing edge. Additionally, a study was performed on the contributions of passive leading edge flexibility showing a decrease in performance, however no details on this were provided.

1.3 Problem Statement

This study seeks to fulfill the gaps in the literature by performing, to the best of the author's knowledge, the first experimental investigation on OFEC systems with passive surface flexibility. In this investigation, both force measurements as well as flow field measurements using particle image velocimetry will be used to assess the performance of inertially-induced, passive surface flexibility at the leading edge of an oscillating foil operating in the low reduced frequency range of the energy harvesting mode. The heaving amplitude, aspect ratio, pitching axis location, and oscillation frequency are all fixed parameters, with $h_0/c = 0.30$, $S/c = 2$, $x_P = 0.50$, and $f = 2$, respectively. The parameters that are varied are the pitching amplitude, motion phase, Reynolds number, reduced frequency, and torsion constant (degree of flexibility), with $45^\circ \leq \theta_0 \leq 75^\circ$, $30^\circ \leq \Phi \leq 120^\circ$, $24,000 \leq Re \leq 48,000$, $0.042 \leq k \leq 0.083$, and $0.07 \leq \kappa \leq \infty$, respectively.

Chapter 2: Experimental Methodology

This sections contains details on the experimental facilities, foil and motion device design, force measurement techniques, motion tracking methods, and particle image velocimetry methods, and are each described in their respective subsections.

2.1 Overall Setup

2.1.1 Wind Tunnel and Facilities

All experiments were conducted in the Experimental Fluid Mechanics Research Laboratory (EFMRL) and the Aero Lab located at Oregon State University. A closed loop wind tunnel was used with an internal cross-section of 1.37 $m \times 1.52$ m with turbulence intensities below 1%. The wind tunnel is equipped with Plexiglas windows on both the top and side of the test section allowing for convenient laser and optical access. The wind tunnel also contains an air-temperature and flow speed readout, which has been calibrated against free stream flow PIV measurements (see Appendix A). The foil and motion device (described in Sections 2.1.2 and 2.1.3) are located in the center of the wind tunnel test section in order to reduce wall boundary effects, and is shown in Fig. 2.1.

2.1.2 Foil Design

The foil used in this study was designed and manufactured in-house using the Machining and Product Realization Lab (MPRL) and FDM/Jet 3D printer facilities. The foil (shown in Fig. 2.2) has a chord length of 125 mm, aspect ratio of 2, and a thickness of 5% of the chord. The foil is composed of four acrylonitrile butadiene styrene (ABS) pieces and a machined titanium rod three quarters the length of the foil span. The foil was attached to the motion device via the titanium rod located at the foil mid-chord. The titanium rod also provides structural support along the foil span to help reduce span-wise flexibility under higher heaving frequencies ($\geq$1.5 Hz). Two of the printed

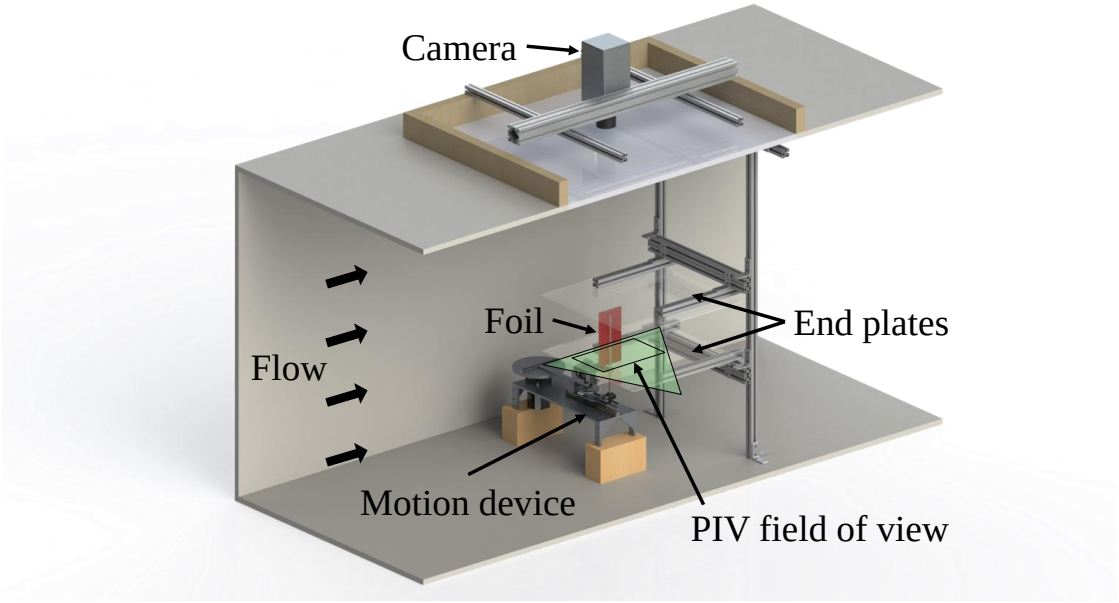

Figure 2.1: The overall experimental setup consisting of the wind tunnel, motion device, foil and end plates, and the camera mounted above the tunnel.

sections are rigidly attached to the titanium rod using pressed inserts, forming the main body section. The remaining two ABS pieces consist of the leading and trailing edges (LE/TE). These edges are configurable to either rigidly attach to the main body, or serve as passively-actuated edges mimicking simplified surface flexibility found in natural flyers and swimmers. The LE/TE edges are elliptical with a major to minor axis ratio of $5:1$ and are each one third of the total chord. In this study, the flexible TE configuration was not used.

The LE was attached to the main body using a metal rod which acts as a dual purpose hinging mechanism (see Fig. 2.3). The rod mechanically attaches the LE to the body and doubles as a torsion spring, providing a restorative force to the LE flap. By anchoring one end of the shaft to the LE and fixing another end to the main body, a torsional restoring force is generated during LE deflection. This allows for a fixed degree-of-freedom flexibility along the foil chord. Due to the foil design, the torsion shaft can be easily replaced with different materials and can be anchored at up to six different axial lengths in order to adjust the torsional restoring force in the flaps. The torsion shafts

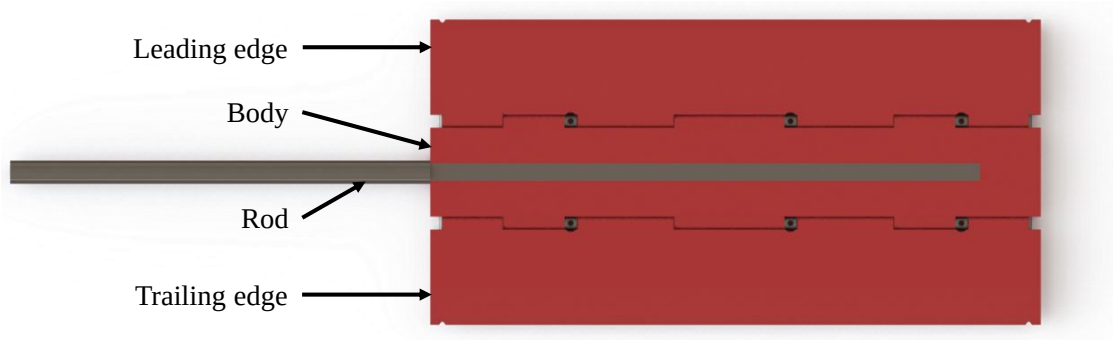

Figure 2.2: A top view of the foil used in this work.

considered in this study were made of steel ($0.13\ N-m/rad$, lower flexibility) and brass ($0.07\ N-m/rad$, more flexibility), each with a diameter of $1.4\ mm$. Additionally, the LE was printed using an internal honeycomb structure in order to reduce the overall foil mass (as opposed to printing an LE made from solid ABS). As such, the density ratio of the LE is $\rho_{LE}/\rho air = 524$, and is inertially dominant over the added mass during LE deflection [34].

Because this study only investigates the effects of a flexible LE, the TE was attached to the body in the rigid configuration. In rigid mode, the LE and/or TE are connected to the main body with an additional steel rod perpendicular to the torsion spring. This rod is sized such that the edges cannot freely flap, keeping the foil elements rigid relative to each other. Further details on the foil components are discussed in Appendix B, which contains an exploded view of the foil and the component masses.

2.1.3 Motion Device

The motion device is comprised of four primary components: the heaving base, pitching carriage, foil assembly, and load cell module as shown in Fig. 2.4. Using a Gecko Drive stepper motor (1.8° resolution), the heaving disk translates the pitching carriage along a linear motion track using a scotch-yoke mechanism capable of heaving through 5 to 20 cm full amplitude in 2.5 cm increments at frequencies ranging from 0.5 to 2.5 Hz. The pitching carriage also utilizes a stepper motor and scotch-yoke system. However, the linear motion delivered from this scotch-yoke is converted into a periodic rotational

motion using a rack and pinion, where the pinion gear is rigidly attached to the foil titanium shaft, and the rack travels along a linear guide. Using this pitching assembly, the foil is capable of sweeping through $\pm 45°$ to $90°$ in $5°$ increments. The pitching carriage also houses two load cells, which are discussed in Section 2.2.

The motions generated by the test device follow sinusoidal pitching and heaving motions according to the following equations, and are controlled through a LabVIEW script. For details on the LabVIEW script, refer to Appendix C.

$$h(t) = h_0 sin(2\pi f t) \tag{2.1}$$

$$\theta(t) = \theta_0 sin(2\pi f t + \Phi) \tag{2.2}$$

where $h(t)$ and $\theta(t)$ are the instantaneous heaving and pitching positions, respectively, h_0 and θ_0 are the heaving and pitching amplitudes, respectively, f is the oscillation frequency, t is the time, and Φ is the phase shift between the pitching and heaving motions. The foil was oriented in the spanwise-vertical direction, such that bias contributions from gravity on the force measurements and foil flexibility were negated. Additionally, Plexiglas foil-tip end plates with a smoothed leading edge were attached roughly 2 mm away from the foil tips to reduce three-dimensional flow effects.

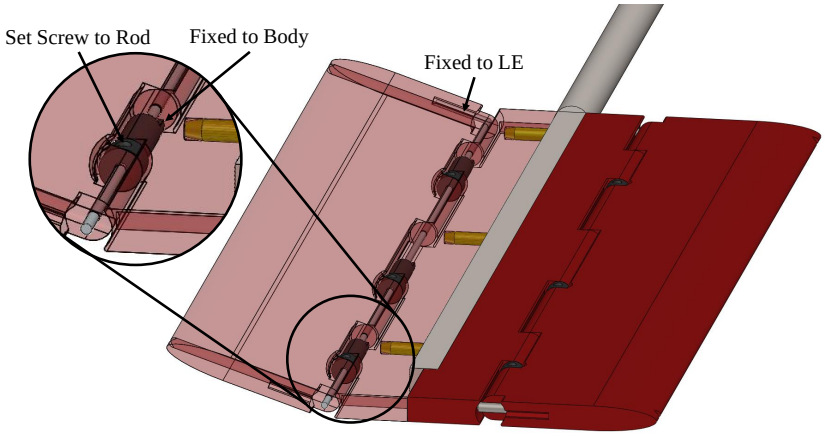

Figure 2.3: Detailed view of the foil hinge mechanism used to achieve passive edge flexibility.

It is important to note that this system does not use linear encoders to measure the instantaneous foil position or pitching angle. However, the timestamp of each stepping signal is known and the motion of the system is mechanically constrained, thus the pitching and heaving positions can be calculated throughout the oscillation cycle. The calculated motion was verified with motion tracking software using the methods outlined in Section 2.3 and shows good agreement and synchronization (Fig. 2.5).

2.2 Force Measurements

All force measurements were collected using two Futek LSB200 load cells, with a resolution of 0.0022 N with a 22.2 N maximum. Voltage signals from the load cells were amplified using an in-house built external amplifier and were recorded in LabVIEW using an NI DAQ board (National Instruments, BNC-2110). The load cells were placed in a flexure device (shown in Fig. 2.6), which was was designed to reduce cross-talk between lift and drag measurements. A bearing was attached to the end of this flexure device, with the foil rod passing through the bearing center. This allows the foil rod to freely pitch, while collecting direct lift and drag force measurements regardless of the

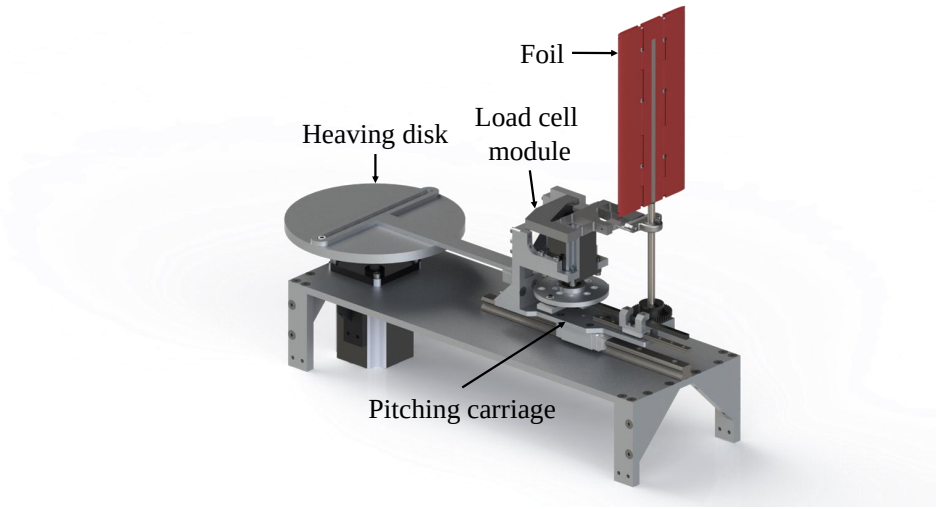

Figure 2.4: The motion device, showing the heaving disk, pitching carriage, load cell module, and the test foil.

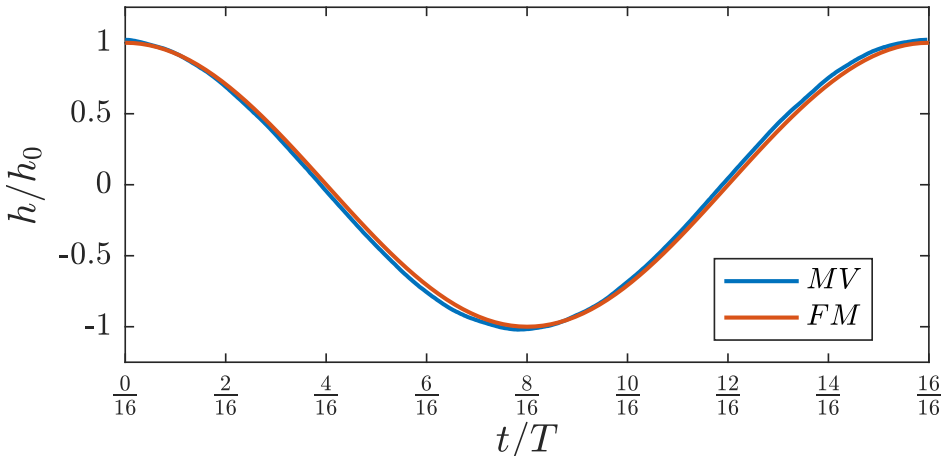

Figure 2.5: Synchronization of foil motion taken from motion video tracking (MV) and force measurement (FM) data. The data presented here is for the case of $\Phi = 90°$ and $\theta_0 = 75°$.

foil instantaneous pitching angle. Forces were sampled at a rate of 200 Hz, resulting in 100 measurements per oscillation period.

2.2.1 Calibration

The load cell voltages were calibrated against known loads by conducting a tare experiment where measurements were collected under three loading scenarios;

1. No external loading on the foil rod.
2. An external force is applied in the lift direction.
3. An external force is applied in the drag direction.

The external force is applied by attaching a known mass to the foil rod using a string and pulley system as shown in Fig. 2.7. This generates a voltage change in the load cells, which is then amplified to the $\pm 5\ V$ scale using an external signal conditioning unit. The amplified force signal is then stored on a computer using the National Instruments data acquisition board. The result of this calibration is the following linear system of equations.

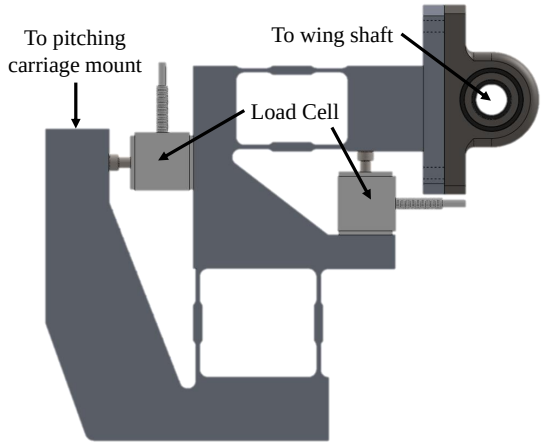

Figure 2.6: Flexure device used to house the lift and drag load cells.

$$\begin{bmatrix} F_N \\ F_A \end{bmatrix} = \begin{bmatrix} M_{V_N \ on \ F_N} & M_{V_N \ on \ F_A} \\ M_{V_A \ on \ F_N} & M_{V_A \ on \ F_A} \end{bmatrix} \left(\begin{bmatrix} V_N \\ V_A \end{bmatrix} - \begin{bmatrix} V_{N,0} \\ V_{A,0} \end{bmatrix} \right) \tag{2.3}$$

where the variables F, V, and M correspond to the force (Newtons), load cell voltage (volts), and the normal and axial calibration constants related to their respective voltage output. The subscripts N, A, and 0 correspond to variables in the normal direction (lift), axial direction (drag), and the null voltage values with no loading, respectively. Note that the M matrix corresponds to the cross-talk between the lift and drag forces. That is, any resulting drag force when a load is applied in the lift direction is accounted for, and any resulting lift force from a load applied in the drag direction is accounted for, similar to the methods of [52].

2.2.2 Validation

In order to assess the validity of the force measurements, lift and drag force data were collected for a statically-mounted wing. In this experiment, a foil with an aspect ratio of 3 was used with no foil-tip end plates. The flow Reynolds number based on the foil chord was set at $70,000$, and the foil was set at different angles of attack ranging from $-20°$ to $24°$ in increments of roughly $3°$. The resulting lift and drag coefficients are plotted

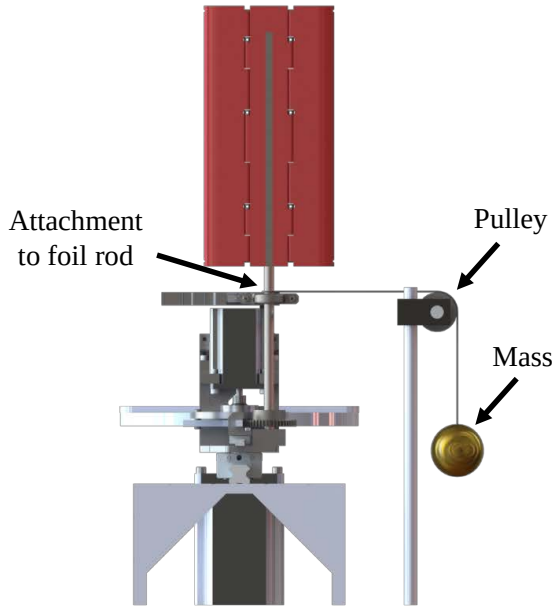

Figure 2.7: Application of attaching a known mass to the foil rod for the calibration procedure. This was done for both the lift and drag directions.

against values obtained by Torres and Mueller [56] in Fig. 2.8.

It can be seen in Fig. 2.8 (a) that as the foil aspect ratio increases, the zero-angle lift curve slope also increases. This results in larger lift gains with increasing angle of attack. The zero-lift slope was calculated to be $4.20/rad$. Additionally, an increase in aspect ratio shows that peak lift forces are obtained near lower attack angles due to the quicker leveling-off of the lift curve. Figure 2.8 (b) also shows slight increases in drag with foil aspect ratio. The measured lift and drag curves in this study follow the trends shown by Torres and Mueller [56], thus showing good validation of the force data acquisition system.

2.2.3 Acquisition Method

Once the LabVIEW program was initiated, the foil was left to oscillate for a minimum of 60 seconds to minimize transient motion-ramp-up induced vibrations. After these initial 60 seconds, force data was collected for a total of 180 seconds and split into 3

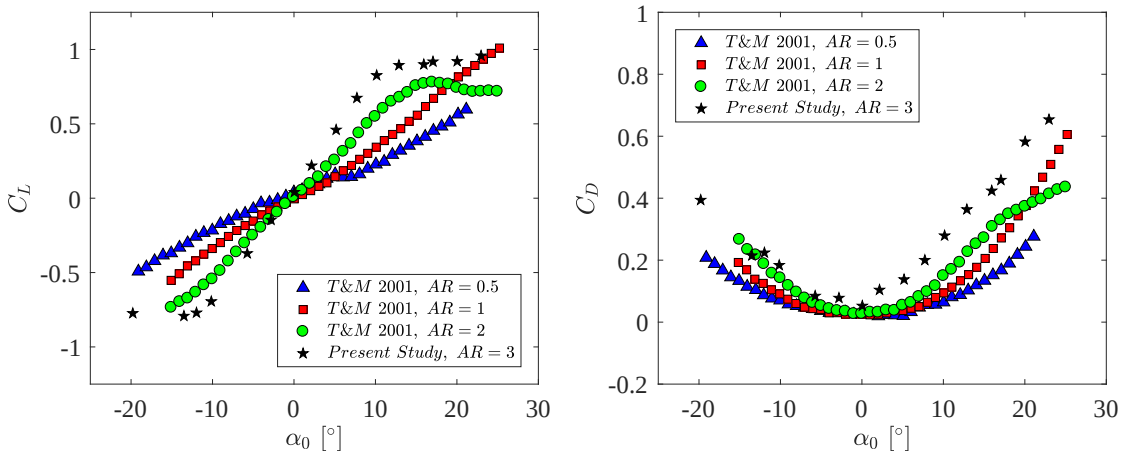

Figure 2.8: Lift and drag coefficients of Torres and Mueller compared to results obtained in this study.

different sections. The first 60 seconds of data account for the inertia contribution of the oscillating foil under no flow conditions. The next 60 seconds correspond to the transient free stream period where the flow is allowed to steady state to the desired flow speed. Finally, the last 60 seconds of data correspond to the measured total forces, which consist of the combined foil inertia and aerodynamic forces. Between each run, a minimum wait time of 180 seconds was used.

A total of seven runs were collected for each force data point presented in this work. Collection of the seven runs was necessary due to variations in the structural resonant frequency of the device and foil, which were measured to range from 22 to 26 Hz. These variations were found to be a direct consequence of the internal loading in the device resulting from the initial setting of the foil. The variation of internal loading in the device and foil originate from: rack and pinion backlash, the degree of pitching amplitude, and the bearing clamping position.

Between each of the seven repetition runs, the backlash of the rack and pinion was reset and the flexure device bearing was loosened and re-torqued into position. It was found that performing this seven times for each operating condition was sufficient to capture the general range of structural loading variability. This can be seen in Fig. 2.9, where each plotted curve is determined by increasing the number of repetition runs

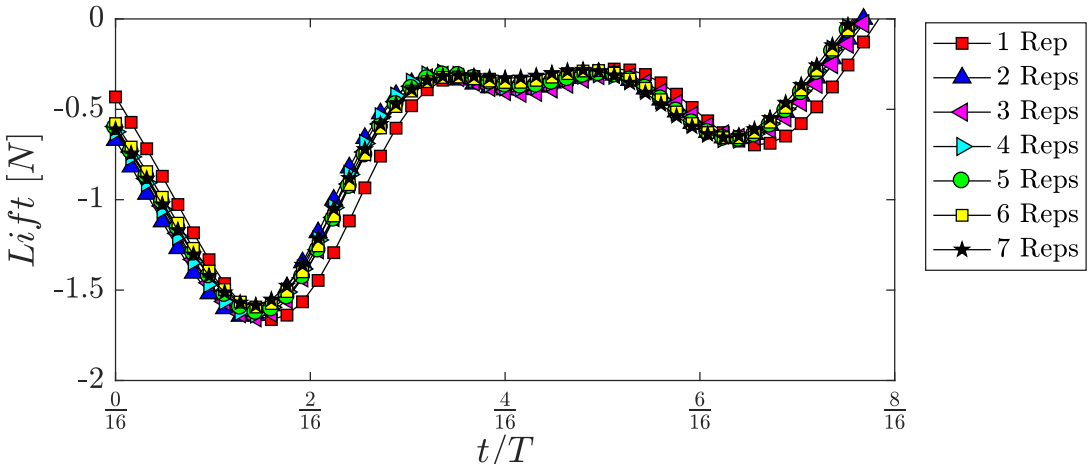

Figure 2.9: Mean lift force curves as additional repetition runs are used to calculate the mean. This data corresponds to an oscillating rigid foil undergoing pitching at $f = 2\ Hz$, $\theta_0 = 75°$, and $\Phi = 90°$ for half of a cycle period.

included in the mean calculation. The data in the figure corresponds to an oscillating rigid foil undergoing pitching and heaving motions at $f = 2\ Hz$, $\theta_0 = 75°$, and $\Phi = 90°$. The data is filtered and processed in accordance to Sections 2.2.4 and 2.2.5. Additionally, repetition runs were not collected sequentially and several different operating points were collected between repeated measurements in order to account for day to day variability.

2.2.4 Filtering and Data Reduction

The seven repetition runs for each operating condition were then uploaded into MATLAB (R2015b) for filtering and processing. Because the aerodynamic center of the foil is cantilevered out with respect to the load cells, a force transformation from the load cells to the aerodynamic center must occur. This is accomplished by taking the sum of the moments about the base of the foil rod (see Fig. 2.10), resulting in the following relationship:

$$F_{Foil} = \frac{F_{LC} L_{LC}}{L_{Foil}} \tag{2.4}$$

The force signals were then divided into two parts; one corresponding to the inertia

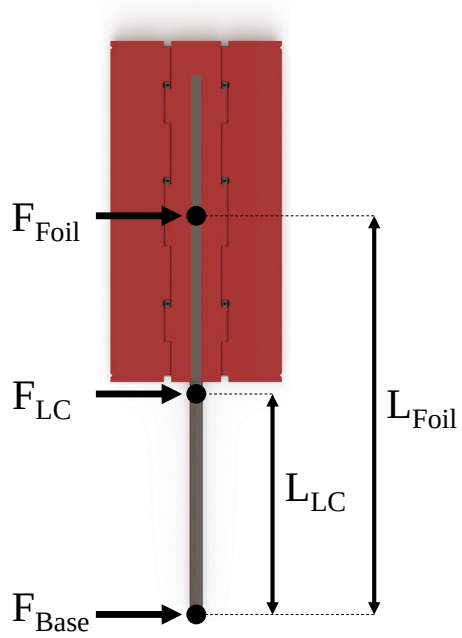

Figure 2.10: Free body diagram used to calculate the forces acting at the foil center. Note that "LC" designates the "load cells", where force measurements are collected.

regime (first 60 seconds), and one corresponding to the total force regime (final 60 seconds). These two signals were converted into the frequency domain using the fast Fourier transform (FFT) method. A low-pass filter was applied using a cutoff frequency of 15 Hz ($7.5f$) for the rigid foil data, and 8 Hz ($4f$) for the flexible LE data. This was found to be a good compromise between preserving the original signal while filtering out the structurally-induced force contributions. The inverse-FFT was then applied to the filtered frequency signal in order to reconstruct the filtered time domain force signal.

The filtered signals were then phase-averaged across 120 cycles (corresponding to 60 seconds of data) starting at the top heaving position. These phase-averaged cycles were then averaged across the seven repetitions of each operating condition to form a single representative force signal for the inertia and total force regimes.

2.2.5 Aerodynamic Force Calculation

In order to calculate the aerodynamic force, the inertia of the foil must be isolated from the total forces. This is accomplished using the formula below, which is similar to the methods of [4, 14, 21, 52].

$$F_T(t) - F_I(t) = F_A(t) \tag{2.5}$$

where subscripts T denotes the total force measured, I is the inertia regime force, and A is the purely aerodynamic force acting on the foil. The values for F_T are obtained from the force measurement data when flow is present, as discussed in Section 2.2.4. Values for F_I, however, may be determined using two different methods outlined below. In these two methods, the subscripts FM and V correspond to data collected from force measurements and video tracking, respectively.

Method 1: force measurement approach. The measured inertia regime forces are directly subtracted off from the total force according to the following formula, where $F_{T,FM} = F_T$.

$$F_{T,FM}(t) - F_{I,FM}(t) = F_{A,FM}(t) \tag{2.6}$$

This method is a good indication of what the aerodynamic forces would be, however the forces collected here are not purely isolated inertial forces. Although there is no prescribed flow in the wind tunnel during these measurements, some flow is generated as the foil oscillates in the otherwise still air. In order to collect purely inertial forces, these forces would need to be measured in a vacuum. On the other hand, it would be permitted to measure the foil inertia in a gaseous medium if flow measurements were collected in a liquid such as water.

Method 2: video tracking approach. This method utilizes measurements taken from motion videos of the foil in order to calculate the foil inertia. Once this "video inertia" is calculated, it is subtracted from the total forces similar to Method 1.

$$F_{T,FM}(t) - F_{I,V}(t) = F_{A,FM\&V}(t) \tag{2.7}$$

The method for obtaining the foil motion is discussed in Section 2.3. The goal of this approach is to use the foil motion in order to calculate a theoretical inertia force.

Using the tracked motion of points A, B, C, and D on the foil (defined in Section 2.3.2), the midpoints of segments $\overline{AB}$, $\overline{BC}$, and $\overline{CD}$ are calculated using a simple averaging. The midpoints of these segments correspond to the middle of the LE, main body, and TE, respectively. Using the MATLAB curve fitting toolbox, a sinusoidal curve fit of the midpoints was performed for the heaving direction (direction of inertia). The degree of the Fourier fit was of two different orders; for motion tracking of bodies that are known to have simple sinusoidal motion such as the main body and the rigid TE, the fit was of 1st order and is as shown below.

$$y_{fit}(t) = a_0 + a_1 cos(tw) + b_1 sin(tw) \tag{2.8}$$

Where the a, b, and w terms are the fit coefficients, and $y_{fit}(t)$ is the fitted heaving position as a function of time. For the flexible LE cases, the LE motion is more unpredictable and is thus anticipated to be of higher order than a simple sinusoidal oscillation. Because of this, an 8th order fit was used of the following form in order to capture these LE oscillations:

$$\begin{aligned} y_{fit}(t) = a_0 + ... \\ a_1 cos(tw) + b_1 sin(tw) + a_2 cos(2tw) + b_2 sin(2tw) + ... \\ a_3 cos(3tw) + b_3 sin(3tw) + a_4 cos(4tw) + b_4 sin(4tw) + ... \\ a_5 cos(5tw) + b_5 sin(5tw) + a_6 cos(6tw) + b_6 sin(6tw) + ... \\ a_7 cos(7tw) + b_7 sin(7tw) + a_8 cos(tw) + b_8 sin(tw) \end{aligned} \tag{2.9}$$

In order to get the heaving velocity and acceleration of the foil, the time derivative of the fit-position was taken appropriately. With Newtons second law, the inertia force of the foil was calculated. For the rigid foil configuration, only the fit-acceleration equation of the midpoint of the body was used, and the mass of the entire foil and rod was used as shown below.

$$F_{I,V}(t) = (m_{LE} + m_{body} + m_{TE} + m_{rod})\ddot{y}_{fit,body}(t) \tag{2.10}$$

For the case of flexible LE measurements, the acceleration and mass of each component of the wing was used according to the following:

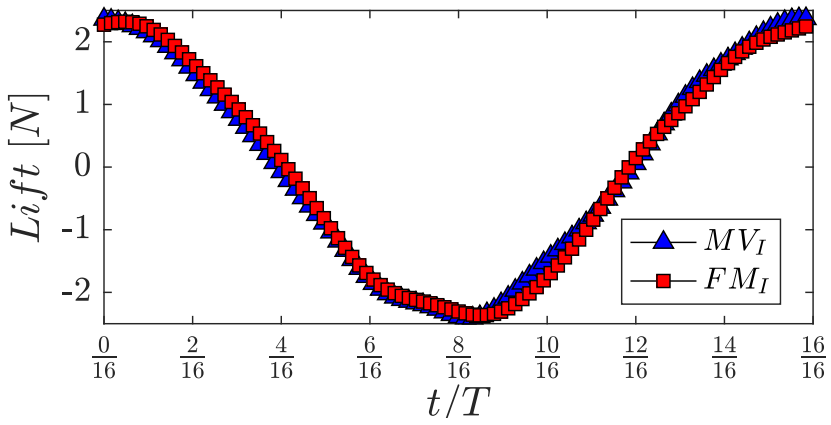

Figure 2.11: Inertia forces calculated from motion videos compared to inertia forces from force measurements for an oscillating rigid foil undergoing pitching at 2 Hz, with $\theta_0 = 75°$, $h_0/c = 0.30$, and $\Phi = 90°$.

$$F_{I,V}(t) = m_{LE}\ddot{y}_{fit,LE}(t) + (m_{body} + m_{rod})\ddot{y}_{fit,body}(t) + m_{TE}\ddot{y}_{fit,TE}(t) \tag{2.11}$$

The inertia as measured by the load cells as well as the video calculated inertia are compared in Fig. 2.11. As can be seen, the magnitudes and general shape of the inertia curves agree exceptionally well. Because of this agreement, the inertia used to determine the aerodynamic loading on the foil was that of Method 1 (solely force measurements).

2.3 Motion Tracking

In addition to the force measurements, the foil motion (position as a function of space and time) was observed. The foil motion is critical to understanding trends shown in force data due to the time-variation of the foil kinematics and effective angle of attack over the oscillation cycle. Additionally, the foil motion was used to calculate an analytical inertia of the foil, which was discussed in Section 2.2.5.

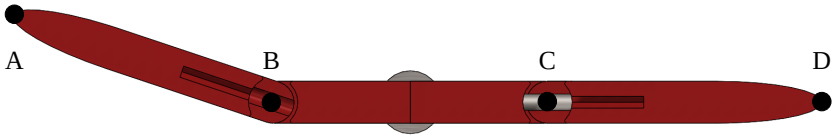

Figure 2.12: The four fiducial marks used for motion tracking. Marks A, B, C, and D correspond to the LE, leading hinge of the body, trailing hinge of the body, and the TE, repectively.

2.3.1 Acquisition Method

Four fiducial marks at different locations along the foil were filmed using a high-speed camera (iNanoSense MotionPro X-3, 1280×1024 pixels) at $1,000$ frames per second over 6 oscillation periods for both conditions with and without flow. Cycle to cycle variability in tracking the marks was small beyond 6 cycles for most cases and was deemed a sufficient cutoff. Image capturing was limited to $1,000$ Hz and 6 oscillation periods due to reduced hardware memory capabilities; however, this collection rate was able to sufficiently reduce spatial blurring effects. Additionally, repetition measurements of the foil motion showed negligible variations. Thus, in light of the information presented, only one video was collected for each operating condition.

2.3.2 Filtering and Data Reduction

The four points, shown in Fig. 2.12, correspond to the following locations on the foil: A is the leading edge, B is the leading portion of the central body (front hinge), C is the trailing portion of the central body (rear hinge), and D is the trailing edge. These four points were tracked as a function of time using Tracker, an open source physics software developed by Douglas Brown of Cabrillo College. In order to enhance the motion tracking of the fiducial marks, the video contrast and light balance was adjusted using ImageJ. Details on the motion tracking and video post-processing can be found in Appendix D.

2.3.3 Angle Calculations

The instantaneous pitching angle θ_P was calculated by finding the angle of the main body $\overline{BC}$ relative to the x-coordinate using the geometric formula below.

$$\|\theta_P(t)\| = acos\left(\frac{\overline{BC}(t)\cdot\hat{i}}{\|\overline{BC}(t)\|\cdot\|\hat{i}\|}\right) \tag{2.12}$$

Because the above formula determines the angle in the range $0^\circ \leq \theta_p \leq 180^\circ$, it shows no sense of directionality of the foil (clockwise or counter-clockwise). Assigning the sign of this angle is accomplished by multiplying θ_p by the non-dimensionalized cross product of the two vectors as follows.

$$\theta_p(t) = \|\theta_p(t)\|\frac{\overline{BC}(t)\times\hat{i}}{\|\overline{BC}(t)\times\hat{i}\|} \tag{2.13}$$

Using the same method, the angle of the LE relative to the body (θ_{LE}) as well as the angle generated by the effective chord of the foil ($\theta_{\overline{AD}}$) were calculated as functions of time.

As the foil is subject to the heaving motion, an additional angle is generated. This angle, the effective angle of attack α_{eff}, is described according to the formula below using the geometry shown in Fig. 2.13.

$$\alpha_{eff}(t) = -atan\left(\frac{\dot{h}(t)}{U}\right) + \theta_{\overline{AD}}(t) \tag{2.14}$$

2.4 Particle Image Velocimetry

2.4.1 Acquisition Method

Two-component phase-locked particle image velocimetry (PIV) measurements were collected using a dual-head Nd:YAG pulsed laser (EverGreen, 145 $mJ/pulse$, max repetition rate of 15 Hz) operating at the 532 nm wavelength. A light sheet of approximately 1 mm thickness was generated at the mid-span of the foil using a LaVision optics module (see Fig. 2.1). Image pairs were collected using a CCD camera (Imager Pro, LaVision) with a resolution of 1600×1200 pixels. The camera was equipped with a 50 mm focal length lens (f-number 2.8) and a 532 nm bandpass filter. The resulting magnification was approximately 0.170 mm/px, yielding a field of view of 271×203 mm, or 2.17×1.62 c.

The time between pulses was varied from 169 to 338 μs for Reynolds numbers of $24,000$ and $48,000$, respectively, resulting in approximately 6.5 to 7-pixel displacement

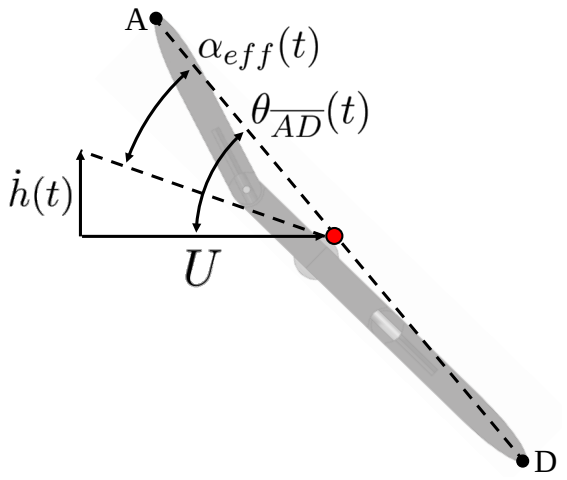

Figure 2.13: The heaving and pitching motions ($\dot{h}(t)$ and $\theta_{\overline{AD}}(t)$, respectively) and resulting effective angle of attack $\alpha_{eff}(t)$. This Fig. is adopted from Young et. al. [65].

of the seeding particles. Seeding particles were generated using an in-house designed and built Laskin nozzle atomizer filled with vegetable oil, resulting in particles of roughly 2 to 6 μm in diameter. The diameter of the particles as captured by the camera is roughly 2.1 px (including the Airy disk diffraction), determined from image autocorrelations. For these phase-locked measurements, 100 image pairs were collected at eight distinct phases. The eight phases are shown in Fig. 2.14, where only the first half of the oscillation cycle is considered due to motion symmetry.

2.4.2 Data Reduction

Image collection and post processing was performed using LaVision DaVIS v8.1.1. The velocity fields were calculated using a multi-pass adaptive cross-correlation between the image pairs, with a sub-pixel peak fitting algorithm. The initial and final interrogation windows in this adaptive scheme were varied from 128×128 pixels to 32×32 pixels, respectively. Using a 50% overlap, the resulting vector field was 100×75 vectors with a spacing of 2.6 mm (2.1% c). Additionally, a minimum peak validation of 1.2 was used to filter spurious vectors. These spurious vectors were replaced with a 3×3 moving average of neighboring vectors.

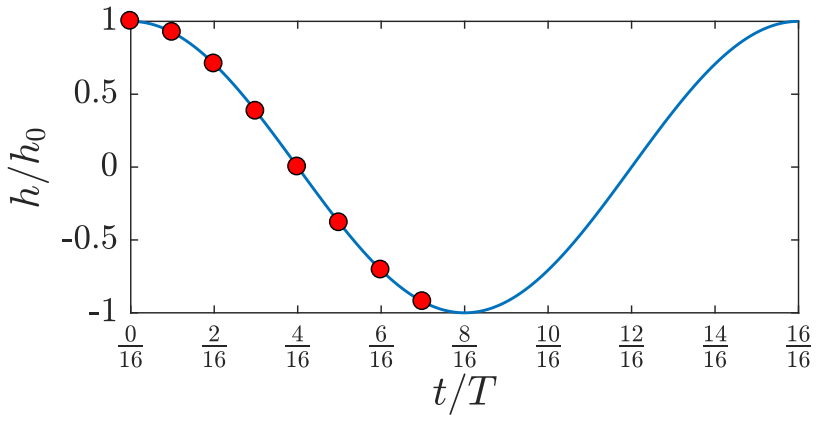

Figure 2.14: The circles indicate the phases at which PIV flow field measurements were taken. The phases are spaced by 1/16ths of an oscillation period, starting from the top heaving position and ending at the bottom heaving position.

Table 2.1: Fixed experimental parameters for force measurements.

h/c	S/c	x_{pitch}/c	f	T [#]
0.30	2	0.50	2	120

2.5 Parameter Space

The force measurement and PIV parameter space of this experimental investigation is discussed in Sections 2.5.1 and 2.5.2, respectively.

2.5.1 Force Measurements

A wide range of parameter space was tested for the collection of force measurements. The physical parameters that were held constant are tabulated in Table 2.1. Additionally, Table 2.2 shows the swept parameters investigated in this study. Note that all combinations of the listed values were tested, with the exception of flexible foil measurements ($\kappa = 0.13,\ 0.07$) which were taken at a Re of $48,000$ only ($k = 0.042$). This results in 105 unique operating points where force measurements were collected, and a total of 735 runs including the seven repeated measurements.

Additionally, motion videos were collected for all testing conditions with a flexible

Table 2.2: Experimental parameters varied for force measurements.

θ_0 [°]	Φ [°]	Re	k	κ $[N-m/rad]$
45, 60, 75	30 : 15 : 120	24000, 32000, 48000,	0.042, 0.063, 0.083	∞, 0.13, 0.07

Table 2.3: Experimental parameters for PIV measurements.

k	θ_0 [°]	Φ [°]	κ $[N-m/rad]$
0.083	75	90	∞
0.083	60	45	∞
0.083	60	60	∞
0.083	60	75	∞
0.083	60	90	∞
0.083	45	75	∞
0.083	45	90	∞
0.083	45	105	∞
0.063	60	60	∞
0.063	45	90	∞
0.042	60	60	∞
0.042	45	90	∞
0.042	60	60	0.13
0.042	45	90	0.13
0.042	60	60	0.07
0.042	45	90	0.07

LE. Because videos were taken with and without flow, a total of 84 motion videos were collected.

2.5.2 Particle Image Velocimetry

PIV experiments were conducted for a much smaller parameter space than the force measurements due to data collection and processing time. A total of 16 unique operating points were collected as per Table 2.3. These operating points were selected in order to show the influence of θ_0, Φ, k, and κ on the overall flow field.

2.6 Uncertainty

This section discusses the relevant experimental uncertainties associated with the force measurements (Section 2.6.1) and PIV measurements (Section 2.6.2).

2.6.1 Force Measurements

Each figure presenting results derived from force measurements showcase error bars of the measurement uncertainty. In determination of these uncertainties, the load cell linearity (±0.1% FSR), hysteresis (±0.1% FSR), and non-repeatability (±0.05% FSR) were used resulting in an uncertainty of $\pm 0.033\ N$. For cycle averaged force curves, the instrumentation uncertainty was combined with the force repeatability across the 120 phase-averaged cycles and seven repetition runs. The free-stream flow speed and density were measured using the FlowKinetics 3DP1A meter, which has uncertainties of ±0.24% FSR and ±0.5% FSR, respectively. The uncertainty in the heaving position was calculated using uncertainties associated with the camera pixel resolution ($\pm 8.13 \times 10^{-5}\ m$), repeatability of tracking ($\pm 4.12 \times 10^{-4}\ m$), cyclic repeatability across 4 phases ($\pm 6.36 \times 10^{-5}\ m$), the RMSE of the position curve fits (max of $\pm 1.69 \times 10^{-4}\ m$), and the motion repeatability across 21 repeated measurements. Using a similar procedure, the uncertainty in the heaving velocity was calculated. The position and velocity uncertainties of the foil motion are plotted in Fig. 2.15 for any given cycle. The maximum uncertainty in position and velocity is $\pm 5.8 \times 10^{-4}\ m$ and $\pm 4.7 \times 10^{-3}\ m/s$, respectively.

For calculated values such as the lift coefficient, power, efficiency, and power coefficient, uncertainties were determined using the sequential perturbation error propagation of the each individual variable's uncertainty. Because of the wide range of parameters tested, the uncertainties for each calculated result cannot simply be summarized as one value. Therefore, these uncertainties are expressed in each figure as error bars.

2.6.2 Particle Image Velocimetry

PIV uncertainty was calculated using the correlation statistics approach outlined by Wieneke in [58]. This section discusses the method used in order to provide a general understanding of the uncertainty calculations. However, for more details in the formulation and implementation of this method, please refer to the cited paper.

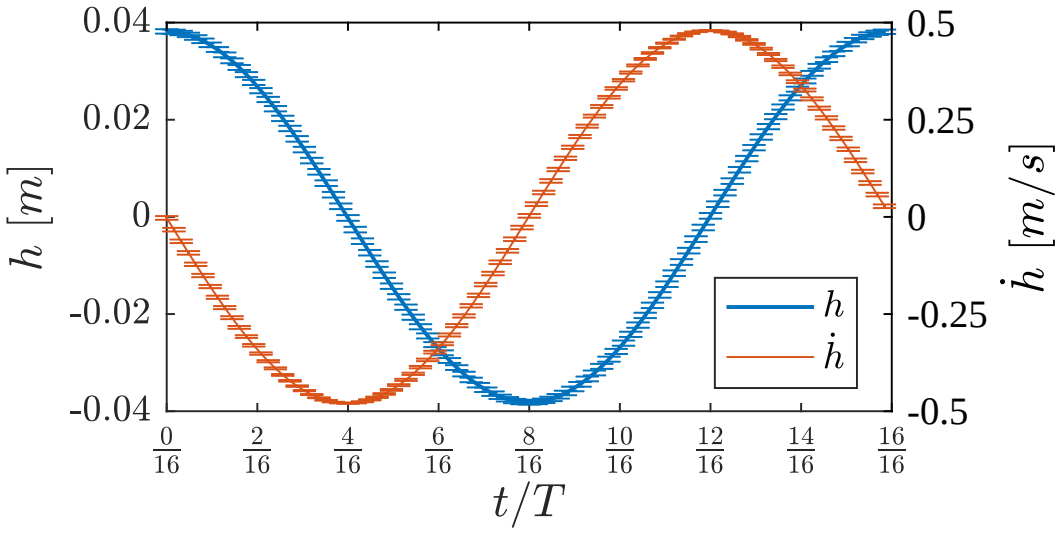

Figure 2.15: The uncertainty in the heaving position and heaving velocity over a a motion cycle.

This method essentially looks at the individual pixels and their fluctuating contributions to the correlation distribution shape, as opposed to computing uncertainties for groups of particles within an interrogation window or by tracking the displacement spread of each individual particle in an interrogation window [44]. As such, this method uses the two PIV images corresponding to an image pair and the displacement field calculated from the cross correlation algorithm. Using the displacement field, the second frame of an image pair is transformed into a reconstructed form of the first image using a high-order sub-pixel interpolation scheme by Astarita and Cardone [3]. By performing this using the same interrogation windows, weighing functions, and sub-pixel interpolation functions as the original PIV algorithm used to calculate the displacements, the following should be true.

$$C(u) = \sum(I_1(x,y)I_2(x+u,y)) = \sum(I_1(x,y)I_2^*(x,y)) \tag{2.15}$$

where, C is the correlation coefficient, u is the x-component of the flow velocity, I_1 and I_2 are the pixel intensities of the first and second images, and I_2^* is the pixel intensity of the reconstructed second image. This function should be at the maximum where

$dC/du = 0$, where the correlation functions at a small $\pm\Delta x$ (typically $\Delta x = 1$ pixel) are equal. In other words, $C_+ = C_-$, and $\Delta C = C_+ - C_- = \sum(I_1(x,y)I_2^*(x+\Delta x, y)) - \sum(I_1(x,y)I_2^*(x-\Delta x, y)) \cong 0$. If this function does not converge, a Gaussian fit to C_-, C, and C_+ will yield convergence. Thus, the formulation now becomes:

$$\Delta C = \sum \Delta C_i = \sum(I_1(x,y)I_2^*(x+\Delta x, y)) - (I_1(x+\Delta x, y)I_2^*(x,y)) \tag{2.16}$$

In this equation, each ΔC_i represents the contributions to the overall ΔC, and any discrepancy means a deviation from a perfect image match between I_1 and I_2^*. Therefore, the standard deviation of ΔC here is indicative of some uncertainty. By taking the sum of the covariance matrix of ΔC_i, the standard deviation is found to be the following.

$$\sigma_{\Delta C}^2 \sum_{\Delta x, \Delta y} S_{\Delta x, \Delta y} \tag{2.17}$$

where $\sigma_{\Delta C}$ is the standard deviation of ΔC and S is the covariance. This is then transformed to give the uncertainty approximation of the displacement field using the Gaussian function between u and C.

This method was subject to a number of typical PIV uncertainties such as random noise (typically found in cameras), particle image sizes, and in-and-out of plane motion. This was accomplished by imposing these errors on a typical PIV image that was numerically generated. As such, the true value of the uncertainties was known, and could be compared to the uncertainties calculated using the correlation statistics approach. They obtained very good uncertainty predictions using this method, particularly when using 32×32 pixel interrogation windows. Again, for details on this approach please refer to the cited paper by Wieneke [58].

The maximum uncertainty in velocity was calculated using the correlation statistics approach to be 2.5% of the free stream flow.

Chapter 3: Results and Discussion

The results presented in this work are separated into four main categories. The first section (Section 3.1) presents the motion of the foil throughout the oscillation cycle. This includes the instantaneous pitching and heaving motions as well as the effective angle of attack of the foil. Section 3.2 then discusses force measurement results for a purely rigid foil. In this section, the energy extraction efficiency, η, power extraction coefficient, C_P, and lift coefficient, C_L, results are shown in order to assess the energy harvesting performance of an oscillating rigid foil operating at low reduced frequencies. Additionally, the influence of pitching angle, θ_0, the phase between pitching and heaving motions, Φ, and the reduced frequency, k, on the performance of the foil are discussed. Section 3.3 then relates the force measurement trends to PIV flow field results for a rigid oscillating foil in order to better understand the fluid-structure interaction responsible for increased extraction performance. Some of the results discussed here pertain to the leading edge vortex (LEV) evolution and corresponding forces exerted on the foil. Finally, Section 3.4 discusses the flow fields and force trends corresponding to two different leading edge (LE) flexibility conditions.

3.1 Foil Motion

The time-varying effective angle of attack of the foil is utilized in order to generate dynamic stall in the flow, resulting in increased lift forces acting along the foil surface. These increased lift forces are the primary mechanism used to harvest flow energy in these systems. Therefore it is important to understand the motion dynamics of the foil before delving into the performance results.

The instantaneous pitching angle θ (solid lines) and effective angle of attack α_{eff} (dashed lines) are shown over one cycle in Fig. 3.1 for: (a) the rigid foil, (b) $\kappa = 0.13\ N-m/rad$ LE, and (c) $\kappa = 0.07\ N-m/rad$ LE configurations. It should be noted that only the $\theta_0 = 45^\circ$ condition is shown here, and the $\theta_0 = 60^\circ$ and 75° pitching angles are shown in Figs. E.1 (b) and (c) of Appendix E due to nearly identical trends for

this range of θ_0. Each curve corresponds to different phase shifts between the pitching and heaving motions. As such, the heaving position h is also shown for reference. Here, h has been non-dimensionalized with the heaving amplitude h_0 and multiplied by the pitching amplitude θ_0 in order to amplify the heaving motion such that it is visible on this scale. As expected, changing Φ results in a shift of the pitching curves relative to the foil trajectory. Additionally, as θ_0 is increased, the motion phase remains unaltered from Φ.

The effective angle of attack is nearly identical to the pitching motion of the foil body for all Φ and θ_0. This is due to the nearly negligible contribution of the heaving motion used to calculate α_{eff} (see Eqn. 2.14) at these low values of k. Because of this, θ is an appropriate indicator of the effective angle of the foil for $k = 0.042$ to 0.083. However, this may not be true when Φ becomes sufficiently large (past $\Phi = 120°$). When Φ approaches 120°, α_{eff} deviates slightly from θ, where the magnitude of α_{eff} slightly decreases, however the timing remains unaltered.

Larger foil pitching angles are expected to generate larger lift forces. However, it is known from static foil studies that at sufficiently high pitching angles the flow around the foil will separate resulting in aerodynamic stall. The intention here is to utilize the large aerodynamic forces resulting from pitching angles past the static stall point dynamically with the foil motion. As the flow begins to stall, the pitching angle of the foil is reduced in order to maintain flow attachment throughout as much of the cycle as possible. This idea is further developed by incorporating a flexible LE, where the LE is allowed to passively respond to the foil kinematics and fluid forces, resulting in a more dynamic effective pitching angle profile. This is explored in more detail in Section 3.4.

Although subtle, the flexible LE configurations show an increase in α_{eff} relative to the rigid foil configuration, raising α_{eff} towards θ. When $\kappa = 0.07\ N - m/rad$, the effective angle of attack is nearly identical to the foil pitching motion. Because of this, it is expected to see slight increases in lift coefficients during the cycle. However, this was found to be not the case and is discussed further in Section 3.4. Because the flexible LE configurations show minute differences in α_{eff} compared to the rigid foil, it is instead useful to look at the deflection angle of the LE relative to the foil body.

The deflection angle θ_{LE} is shown in Fig. 3.2 (a) and (b) for $\kappa = 0.13$ and $0.07\ N - m/rad$, respectively, when $\theta_0 = 45°$. For $\theta_0 = 60°$ and 75°, and $\kappa = 0.13$ and $0.07\ N - m/rad$, see Figs. E.4 and E.5. When $\theta_0 = 45°$ and $\kappa = 0.13\ N - m/rad$,

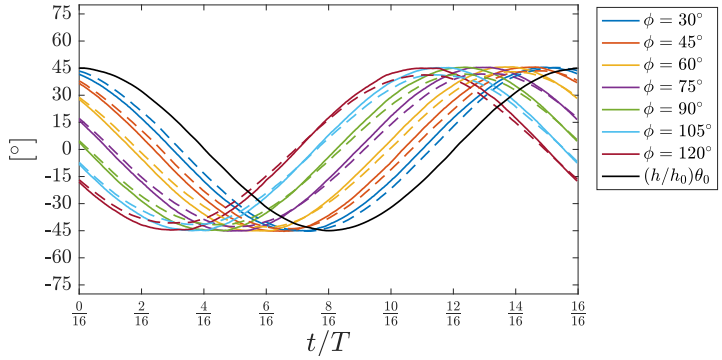

(a)

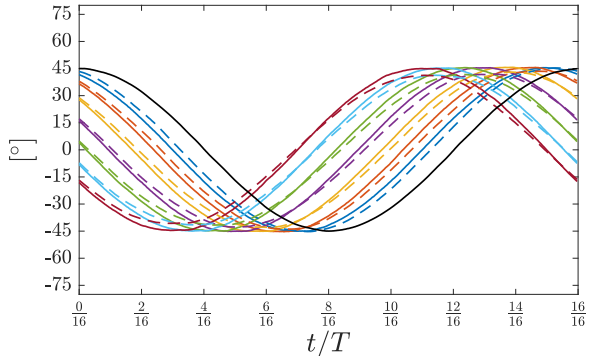

(b)

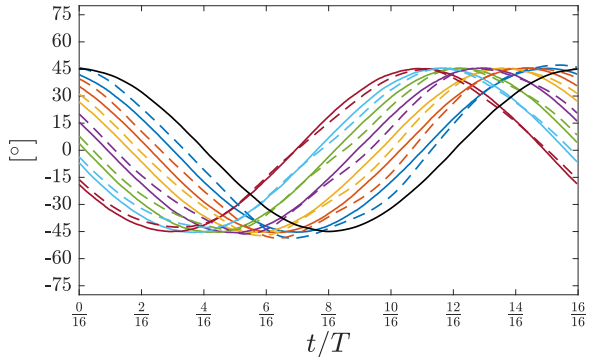

(c)

Figure 3.1: The instantaneous pitching angle θ (solid lines) and the effective angle of attack α_{eff} (dashed lines) over a cycle for the (a) rigid, (b) $\kappa = 0.13\ N-m/rad$ LE, and (c) $\kappa = 0.07\ N-m/rad$ LE foil configurations. The instantaneous position of the foil is also shown for reference, where the position is non-dimensionalized with the heaving amplitude and multiplied by the pitching amplitude in order to amplify it on this scale.

the maximum deflection angle of the LE is $\theta_{LE} = \pm 12°$ relative to the foil body. The point at which this peak LE deflection occurs depends on the motion phase Φ. However for all Φ the LE oscillates at a frequency of 5 times the motion frequency of the foil. Again, Φ incurs a shift in the LE deflection and does not significantly alter the deflection magnitudes. This suggests that the LE deflection is significantly influenced by the foil motion (inertially-induced deflection) and less influenced by the free stream flow. Although the LE shows a fluctuating deflection, in general the deflections maintain a positive and negative contribution when the foil has a positive and negative pitching angle, respectively. This results in an additive contribution to the overall foil angle throughout the foil motion.

When $\kappa = 0.07\ N - m/rad$, a slightly different behavior is observed. In this case, peak deflection angles vary from 30° to 39° at a frequency of 3 times the foil oscillation frequency. Additionally, LE deflections are more random in amplitude and timing, suggesting a higher contribution of the free stream flow than that of the $\kappa = 0.13\ N-m/rad$ case. In the case of $\theta_0 = 45°$, $\kappa = 0.07\ N - m/rad$, and $\Phi = 45°$, the instantaneous deflection angles of the LE drastically vary from cycle to cycle, resulting in lower overall deflection angles when cycle averaged (as in Fig. 3.2 (b)). When $\theta_0 = 60°$ and 75° (Figs. E.5 (b) and (c)), the deflections are less chaotic and revert to inertia-dominant motion.

3.2 Rigid Foil Force Measurements

3.2.1 Efficiency and Power

Figure 3.3 shows the energy extraction efficiency η for a rigid foil operating at reduced frequencies of (a) $k = 0.083$, (b) $k = 0.063$, and (c) $k = 0.042$. The parametric space shown consists of $\theta_0 = 45°$, 60°, and 75°, and $\Phi = 30°$ to 120° in steps of 15°. For the case of $k = 0.083$ (Fig. 3.3 (a)), peak energy extraction efficiency occurs at $\theta_0 = 45°$ and $\Phi = 90°$, with $\eta = 15.5\%$. Efficiencies quickly decrease as Φ is raised past 90°, and decrease more moderately as Φ is decreased below 90°. Additionally, efficiencies are generally higher when $\theta_0 = 45°$ and decrease with increasing θ_0, consistent with the results presented in Zhu [69]. In Zhu [69], extraction efficiencies decrease from roughly 12% at $\theta_0 = 45°$ to 7% at $\theta_0 = 75°$ for $k = 0.083$ for a similar configuration. It should be noted that in Zhu's paper, $h_0/c = 0.25$ and $x_p/c = 0.35$ versus the higher values of

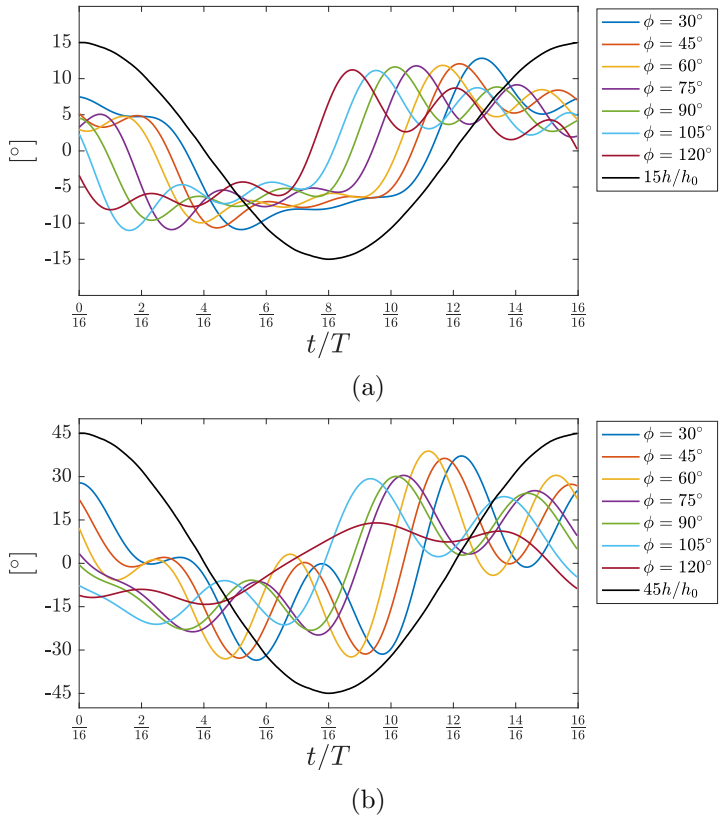

Figure 3.2: The instantaneous LE angle relative to the foil body θ_{LE} over a cycle for the (a) $\kappa = 0.13\ N - m/rad$ LE, and (b) $\kappa = 0.07\ N - m/rad$ LE configurations. The instantaneous position of the foil is also shown for reference, where the position is non-dimensionalized with the heaving amplitude and multiplied by a constant shown in the legend in order to amplify it on this scale.

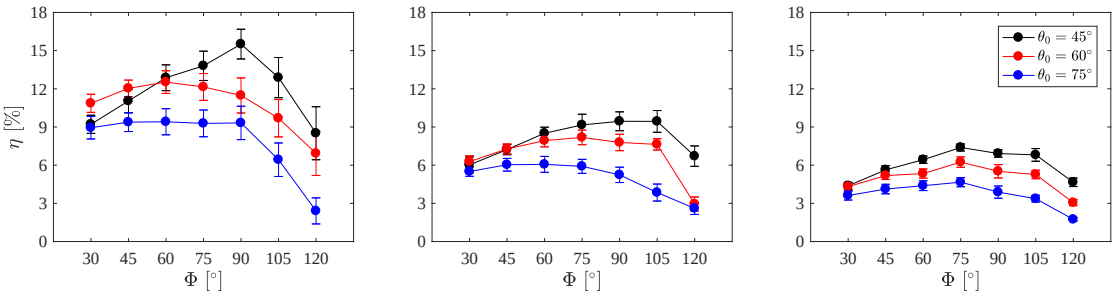

(a) (b) (c)

Figure 3.3: Energy extraction efficiency versus motion phase for $k =$ (a) 0.083, (b) 0.063, (c) 0.042. Additionally, three pitching angles of $\theta_0 = 45°$, 60°, and 75° are shown in each subfigure.

$h_0/c = 0.30$ and $x_p/c = 0.5$ used in this study.

As k decreases to 0.063 and 0.042 (Figs. 3.3 (b) and (c), respectively), overall efficiencies in the parameter space quickly drop. At these k values, overall efficiencies become less sensitive to θ_0 and have significantly reduced sensitivity to Φ. For $k = 0.063$ the peak efficiency is 9.45%, and 7.39% for $k = 0.042$. Additionally, peak efficiencies occur near $\theta_0 = 90°$ and $\Phi = 45°$ for $k = 0.063$ similar to the $k = 0.083$ condition. When $k = 0.042$ the peak efficiency shifts to a lower phase of $\Phi = 75°$. However, because the efficiency has reduced sensitivity to Φ at $k = 0.042$ and $k = 0.063$, peak efficiencies can occur in the range of $\Phi = 75°$ to 105°. A more direct comparison across the three reduced frequencies is also shown in Fig. 3.4, where the dashed, dashed-dot, and dotted lines (black, blue, and red for color copies) correspond to reduced frequencies of 0.083, 0.063, 0.042, respectively.

Figure 3.5 shows the power coefficient C_P for the same parameter space as Fig. 3.3. Although peak efficiencies were shown to occur near $\theta_0 = 45°$ and $\Phi = 90°$, a peak C_P of 0.173 is shown near $\theta_0 = 60°$ and $\Phi = 60°$ when $k = 0.083$. Additionally, overall power coefficients decrease rapidly with decreasing reduced frequency, where peak power coefficients fall from 0.173 to 0.109 and 0.085 for $k = 0.083$, 0.063, and 0.042, respectively. However, the location of peak power extraction tends towards a smaller pitching angle of $\theta = 45°$ and an increased phase of $\Phi = 75°$. Again, a combined plot is shown in Fig. 3.6, where the dashed, dashed-dot, and dotted lines (black, blue, and red for color copies)

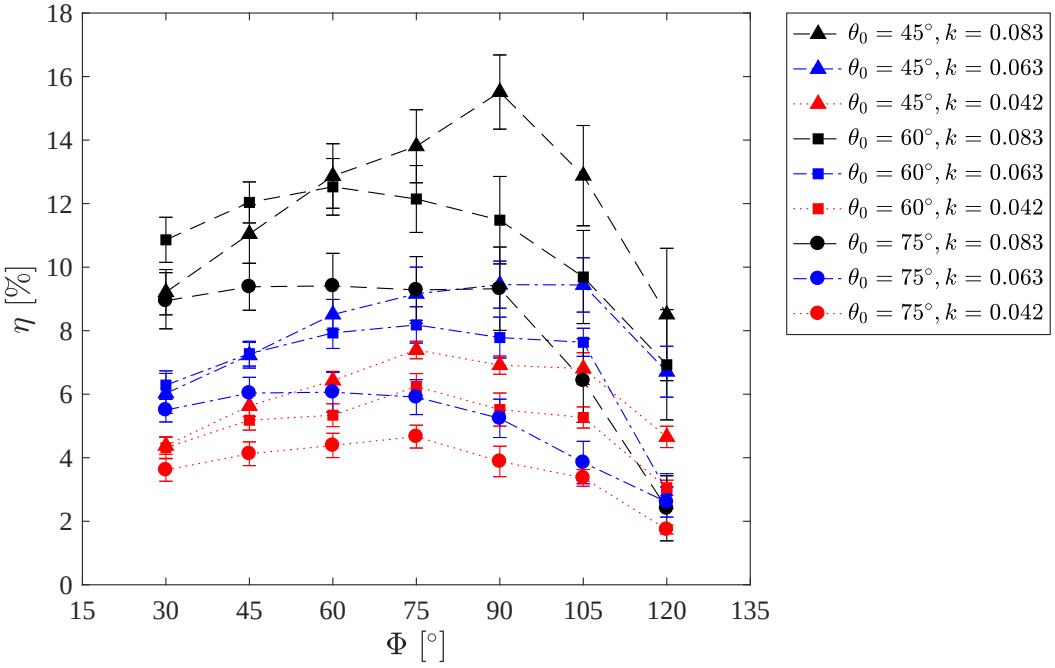

Figure 3.4: Energy extraction efficiency as a function of phase angle Φ, for $\theta_0 = 45°$, 60°, and 75°, and reduced frequencies of $k = 0.083$, 0.063, and 0.042.

correspond to reduced frequencies of 0.083, 0.063, and 0.042, respectively.

The differences between η and C_P are a direct result of the foil motion. Because η contains the total swept height of the foil, which is not constant across different operating conditions, η can be thought of as a "dynamic" performance metric whereas C_P is a "static" metric. Therefore, the changing swept height of the foil is expected to have a significant influence on η as θ_0 and Φ are varied. The efficiency results in Fig. 3.4 show that the increased swept height at $\Phi \neq 90°$ significantly lower the efficiency performance of energy harvesting, despite peak energy extraction occuring at lower Φ (see Fig. 3.6). This trade off must be considered during the designing of these systems as C_P may be a more important metric over η.

The relationships between the energy extraction efficiency and the power coefficient for the range of parameters tested is shown in Fig. 3.7. Note that each line in the figure corresponds to a certain pitching amplitude and reduced frequency, with all motion

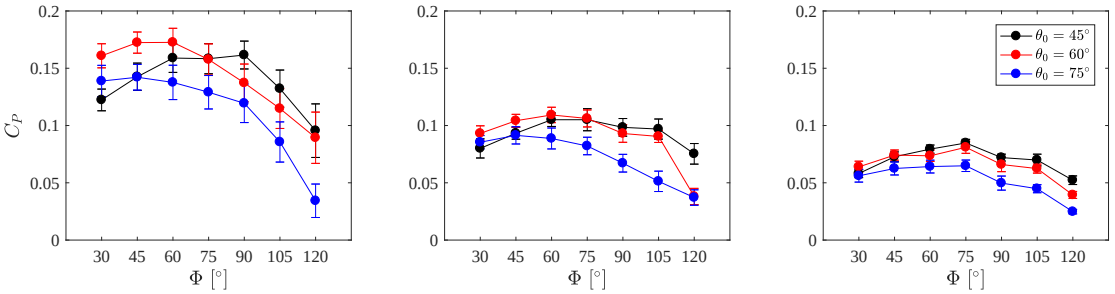

(a) (b) (c)

Figure 3.5: Power coefficient versus motion phase for $k =$ (a) 0.083, (b) 0.063, and (c) 0.042. Additionally, three pitching angles of $\theta_0 = 45°$, 60°, and 75° are shown in each subfigure.

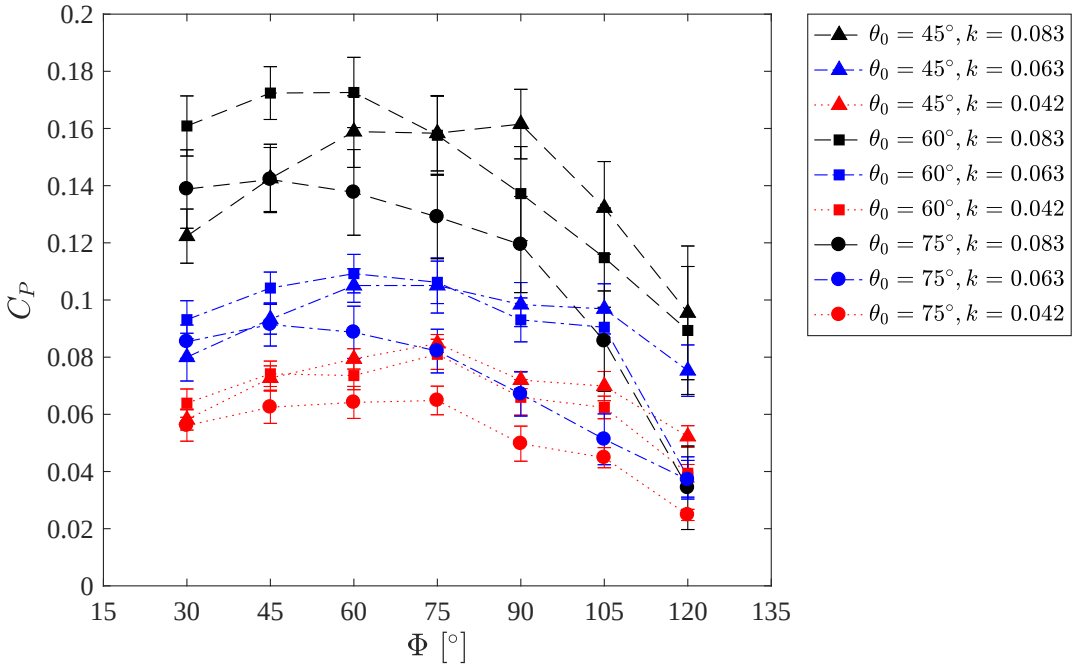

Figure 3.6: Power coefficient as a function of phase angle Φ, for $\theta_0 = 45°$, 60°, and 75°, and reduced frequencies of $k = 0.083$, 0.063, and 0.042.

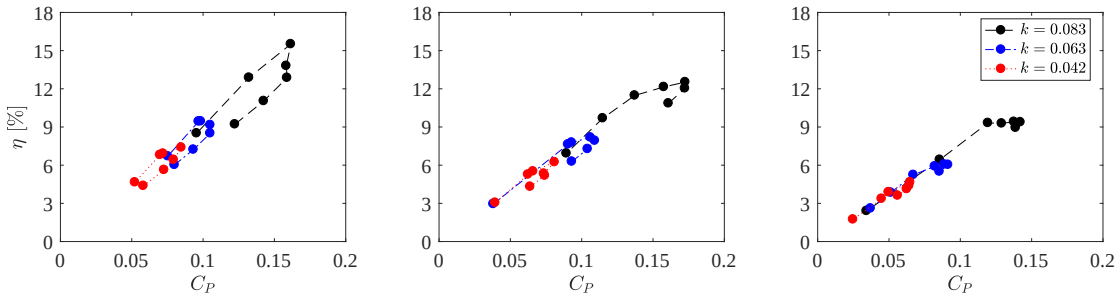

(a) (b) (c)

Figure 3.7: Energy extraction efficiency versus the power coefficient for θ_0 = (a) 45°, (b) 60°, (c) 75°. Also, error bars are not shown in order to reduce clutter. However, the error in η and C_P can be found in Figs. 3.3 and 3.5, respectively.

phases included. The pitching phase increases in the counter-clockwise direction of each curve (follow the lines between the dots). For the low reduced frequencies considered, nearly proportional increases in efficiency and power are observed for all θ_0 runs. Additionally, peak η and C_P increase as k is increased for all three θ_0. However, as θ_0 is increased, peak η and C_P points occur at lower Φ. For example, consider the $\theta_0 = 45°$ curve in Fig. 3.7 (a). The point with the largest η and C_P occurs at a pitching phase of $\Phi = 90°$, whereas this point occurs at a $\Phi = 60°$ and $\Phi = 45°$ for $\theta_0 = 60°$ and $\theta_0 = 75°$, respectively (Figs. 3.7 (b) and (c)). Another interesting observation is that the efficiency remains relatively constant at approximately 9.3% to 9.4% for $\Phi = 30°$ to 90°. A final observation can be made by fitting a linear trend line to each figure in Fig. 3.7. These linear fits are plotted in Fig. 3.8, and show decrease in slope as θ_0 increases. This suggests a weaker sensitivity to efficiency with increasing θ_0 over the parameter space considered.

3.2.2 Lift Curves

In order to understand the efficiency and power trends, the data are broken down into their fundamental lift curves. However, due to the large amount of force data, snippets of these data are presented in order to discuss trends in the lift curves and how the parameters influence the overall foil lift. The lift curves for all data are shown in Appendix

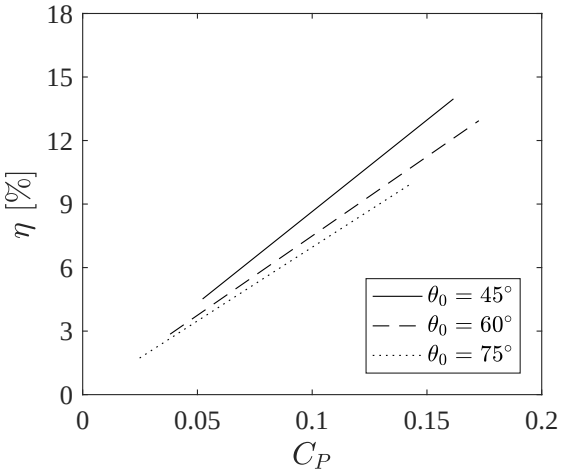

Figure 3.8: Linear fits of the η versus C_P curves in Fig. 3.7 (a), (b), (c).

F for the rigid foil. Additionally, the heaving amplitude is held constant for all tests. As such, the heaving velocity shown in the following figures is simply non-dimensionalized with the maximum heaving velocity and is shown as a reference. This will help determine which force curves are more in phase with the foil velocity and thus which set of conditions are more likely to yield higher energy harvesting.

This section is split into three parts; Section 3.2.2.1 discusses the contributions of the phase Φ, Section 3.2.2.2 discusses the contributions of the pitching angle θ_0, and Section 3.2.2.3 discusses the three reduced frequencies considered.

3.2.2.1 Phase

Figure 3.9 shows the influence of Φ on the overall C_L curves for $k = 0.083$, 0.063, 0.042, and $\theta_0 = 45°$, 60°, and 75° over the oscillation cycle. Here, only motion phases of $\Phi = 75°$, 90°, and 105° are shown in order to reduce figure clutter. It is shown that the influence of the motion phase does not significantly change the force time history profiles, but more so incurs a shift in the timing of the lift curves with respect to the heaving motion for all k and θ_0. It can be seen that as Φ is increased, peak lift forces occur earlier in the cycle period, and a decrease in Φ results in delayed peak lift to later in the oscillation cycle.

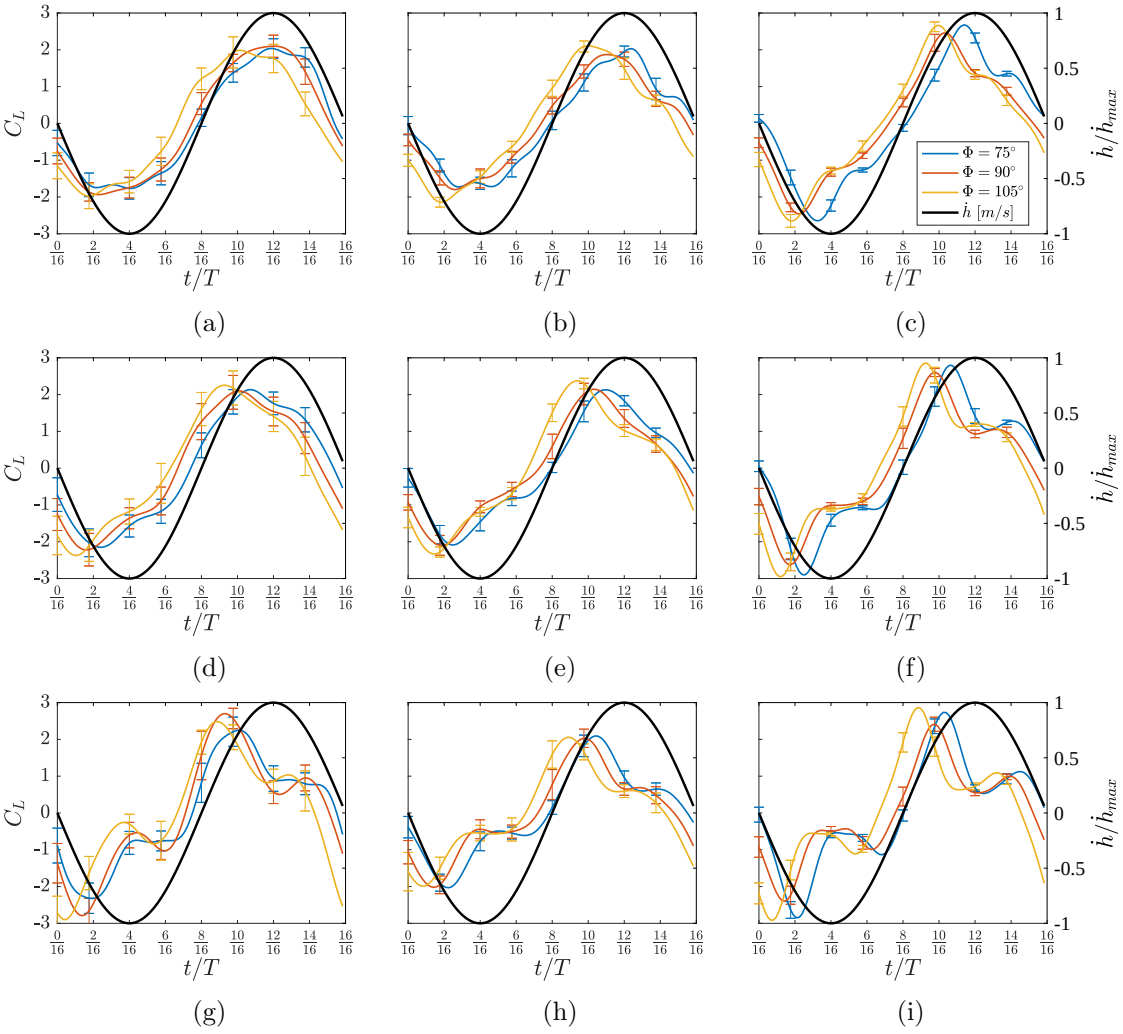

Figure 3.9: Lift coefficient versus the cycle period. The rows correspond to changing θ_0, where the top, middle, bottom rows are for $\theta_0 = 45°$, $60°$, and $75°$, respectively. The columns correspond to changing k, where the left, middle, and right columns are for $k = 0.083$, 0.063, and 0.042, respectively. Φ of $75°$, $90°$, and $105°$ are shown in each sub-figure.

When $k = 0.083$ and $\theta_0 = 45°$ (Fig. 3.9 (a)), the $\Phi = 90°$ lift curve is well aligned with the heaving motion of the foil. As k is decreased (with $\theta_0 = 45°$, Fig. 3.9 (b) and (c)), the required motion phase which results in synchronized lift and foil velocity also decreases to roughly $\Phi = 80°$ and $\Phi = 70°$ (no data collected at these Φ). This means that the foil needs to delay the pitching motion such that the largest effective angle of attack occurs later in the cycle (see Fig. 3.1 (a) for α_{eff} profiles of the rigid foil). This is investigated in more detail in Section 3.3, where the flow field is used to describe the resulting force trends. When the pitching amplitude is increased to $\theta_0 = 60°$ and 75°, the motion phase still controls the timing of the force curves. However, all curves exhibit peak forces at about 2/16 t/T and 3/16 t/T earlier in the cycle than $\theta_0 = 45°$ for $\theta_0 = 60°$ and 75°, respectively.

3.2.2.2 Pitching Angle

The contributions of θ_0 on the overall force histories for $k = 0.083$, 0.063, 0.042, and $\Phi = 75°$, 90°, and 105° as a function of the oscillation period in the cycle are shown in Fig. 3.10. Because it has been established that Φ controls the timing of the lift curves relative to the foil motion, only three of the seven Φ's are shown. For $k = 0.083$, θ_0 has a significant influence on the overall force time history. When $\theta_0 = 45°$, there is a clear single-peak in C_L per half-cycle. As θ_0 is increased to 75°, C_L shows a clear shift towards a two-peak distribution per half-cycle.

Additionally, peak forces are increased with θ_0. However, the overall width of these peak forces become more narrow, a result of the valley present between the two peaks in each half cycle. Although it is not clear if this larger (in magnitude) but narrow peak yields greater energy extraction in this figure, the timing of the force histories clearly show a loss of synchronization with the foil heaving velocity. This alone results in a decrease in overall energy extraction and efficiency (Figs. 3.5 and 3.3), regardless of the increased forces. These trends are also observed at $k = 0.063$ and 0.042, however sensitivity to θ_0 is reduced. As such, for these relatively low k oscillating foil energy harvesters, lower pitching angles ($\theta_0 = 45°$) with a motion delay near $\Phi = 90°$ are desirable.

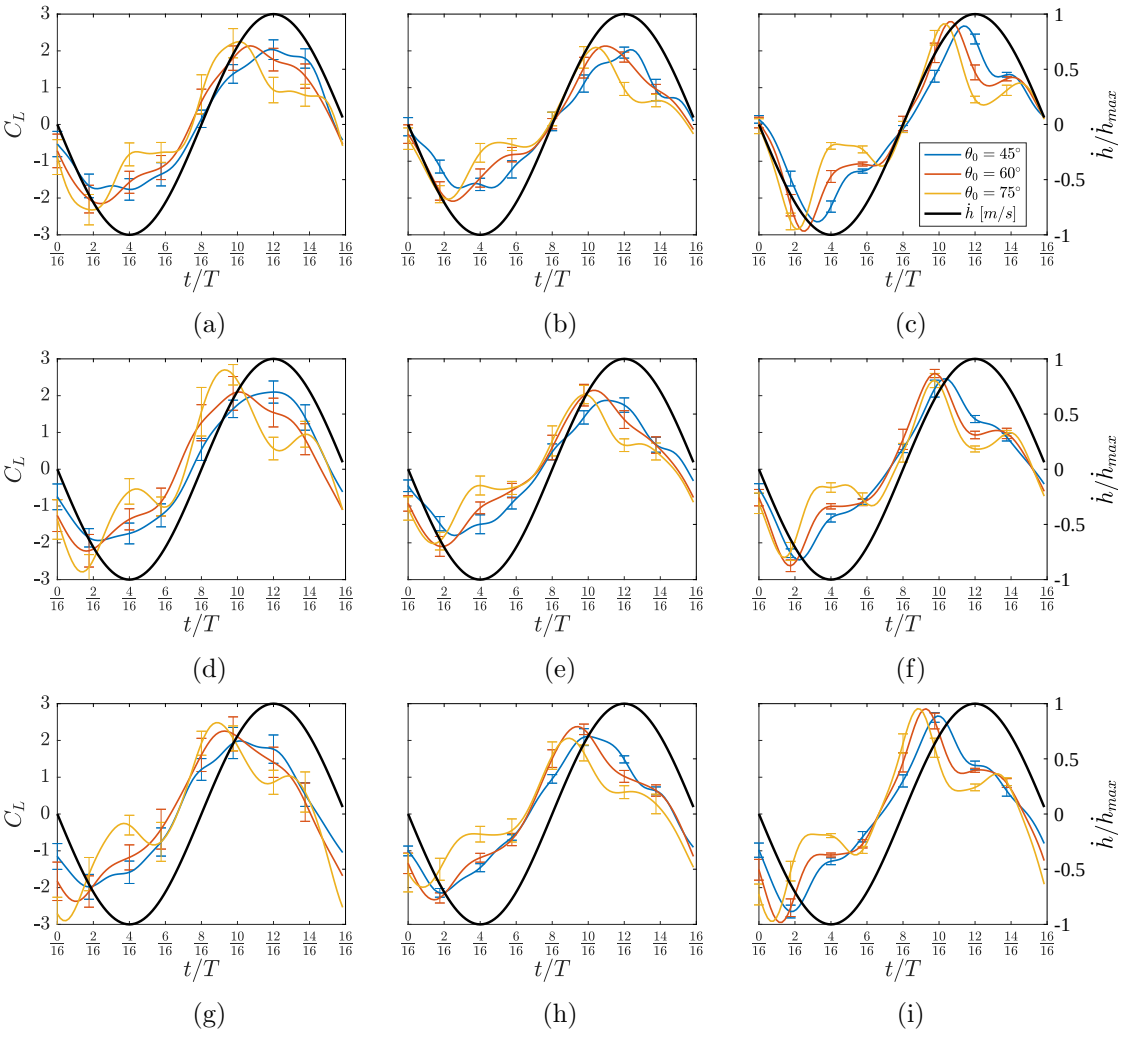

Figure 3.10: Lift coefficient versus the cycle period. The rows correspond to changing Φ, where the top, middle, bottom rows are for $\Phi = 75°$, $90°$, and $105°$, respectively. The columns correspond to changing k, where the left, middle, and right columns are for $k = 0.083$, 0.063, and 0.042, respectively. θ_0 of $45°$, $60°$, and $75°$ are shown.

3.2.2.3 Reduced Frequency

In addition to the pitching angle, the reduced frequency has considerable affect to the overall lift curves. As k is decreased, peak lift forces occur earlier in the cycle, resulting in a loss of synchronization with the foil motion and thus, lower energy harvesting. Additionally, decreased k yield larger peak lift forces due to the corresponding increase in the effective angle of attack α_{eff}. However, peak forces form closer together across different motion phases, showing a slightly reduced sensitivity to Φ as k is decreased. The sensitivity in the force time history is also decreased with varying θ_0 when k is decreased to 0.042. At this operating point, the lift curves nearly collapse into a single curve for each Φ.

It is commonly accepted that the optimal operating space for energy harvesting is near $k = 0.15$. Therefore it is no surprise that larger energy extraction and efficiency occur at the larger k tested in this study ($k = 0.083$). However, there may be situations where operating at $k = 0.15$ is not an option, but moderate harvesting is desired. These results show that θ_0 and Φ may be used to control the evolution of the force curves to yield reasonable energy extraction. Furthermore, the pitching and motion phase may be modified in order to yield stabilized energy harvesting performance as free stream conditions change.

Because peak C_P and η tend towards lower θ_0 and larger Φ with a decrease in k, there may be additional operating points outside of the parameter space tested that yield increased energy extraction performance. Thus it is necessary to investigate the flow field around the foil in order to understand the flow features responsible for these dynamic lift trends. This information can then be used to determine the mechanisms which result in the discussed forces, thus providing guidance on how to design these systems to operate with moderate or controlled energy harvesting at low k.

3.3 Rigid Foil PIV Measurements

3.3.1 General Results

PIV results are shown for the rigid foil in order to link flow field characteristics with force trends. These results are used to explain the timing and magnitude of forces in terms of the flow features, and the influence of the parameter space on the development

of these force trends. Therefore it is useful to begin this discussion using the flow field for the highest efficiency case of $k = 0.083$, $\theta_0 = 45°$, and $\Phi = 90°$, where $\eta = 15.5\%$ as a reference. This is shown in Fig. 3.11, where the phase-averaged vorticity and flow velocity vectors are shown for eight phases throughout the first half of the oscillation cycle. The corresponding lift (C_L) and foil velocity ($\dot{h}$) curves are shown in Fig. 3.9 (a), where the lift and velocity curves are the red and black curves, respectively.

At $t/T = 0/16$ to $1/16$, the foil is near the top heaving position and is just beginning its descent in heave and pitch. There is no indication of a leading edge vortex (LEV) on the bottom half of the foil and the flow remains closely attached to the foil surface, corresponding to low levels of lift and low foil velocity. However, an LEV is detected at the LE when $t/T = 2/16$. The LEV at this time is small and compact with its core close to the foil surface, resulting in peak lift generation. When $t/T = 3/16$, the LEV has quickly grown and has convected approximately $0.3c$ down the foil. Because the LEV is still fairly compact and near the foil surface, the resulting lift is still relatively large at 96% of the peak lift. This position marks the initiation of the LEV detachment process.

When $t/T = 4/16$ and $5/16$, the shear layer that feeds vorticity into the LEV is cut off from the vortex, resulting in the detachment of the LEV from the foil surface. This can be seen by the distinct decrease in vorticity to near 0 between the shear layer and the LEV. This results in a 21% decrease in lift from the peak C_L when the foil is heaving at its maximum velocity. At $t/T = 6/16$ and $7/16$, the LEV is no longer coherent, resulting in fully separated flow in the foil wake. Aerodynamic stall is reached at this point yielding significantly decreased lift forces. However, this occurs when the foil velocity is near zero so a decrease in power extraction performance is not significant.

From these flow field characteristics, two distinct observations are deemed essential for increased energy extraction performance. The first is that the LEV should remain compact and near the foil surface, resulting in a low pressure region just under the foil surface. Because of the higher pressure on the top side of the foil and decreased pressure on the underside, an enhanced lift force in the direction of the foil motion is generated. By maintaining a coherent, concentrated vortex near the foil surface, the magnitude of lift is increased thus resulting in higher energy harvesting.

The second observation is that the LEV forms and detaches itself from the foil surface relatively quickly at low k compared to $k = 0.15$ [69]. As k is decreased, the free stream flow becomes more dominant ($k = fc/U_\infty$) in the flow evolution resulting in elevated

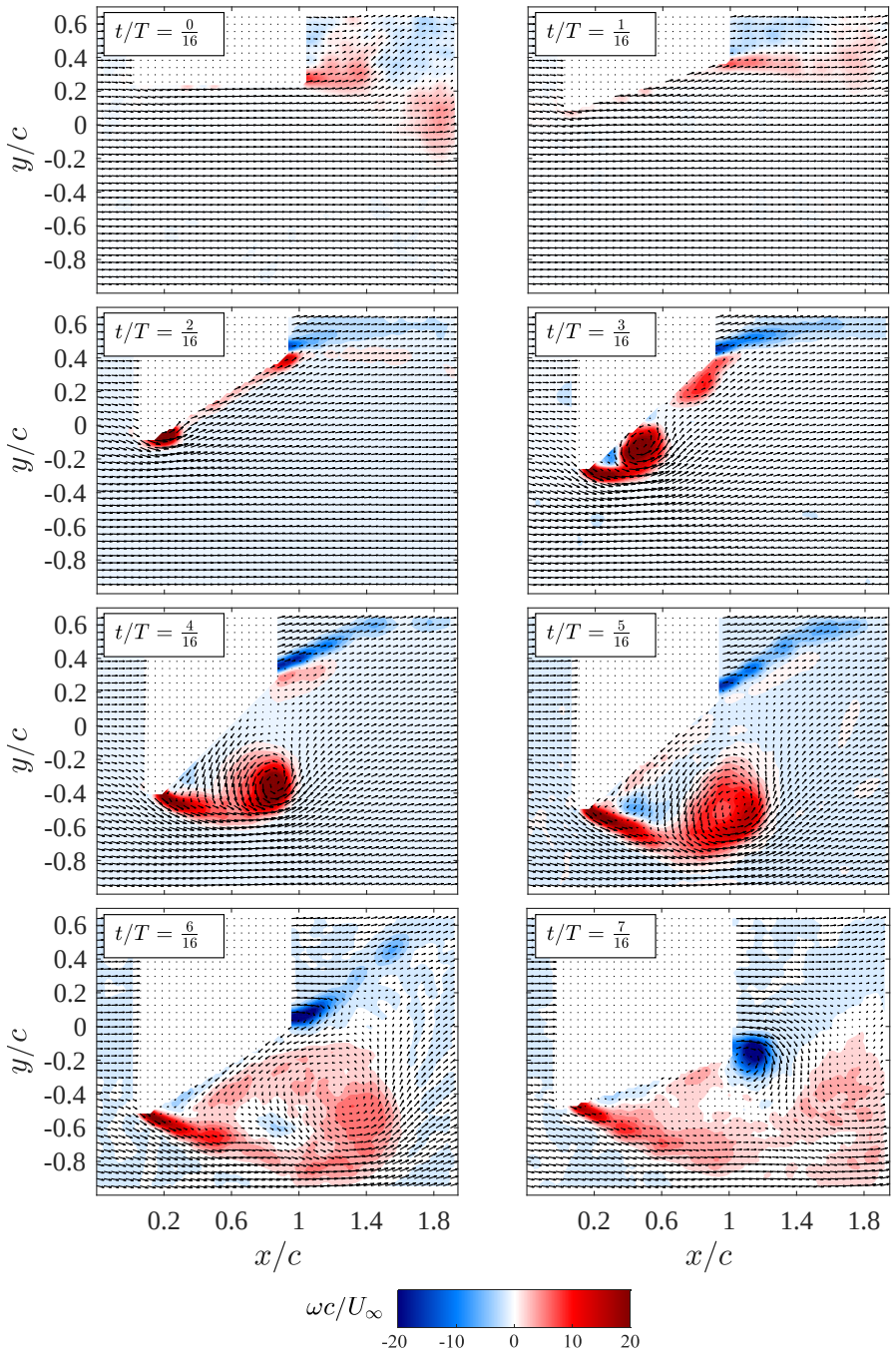

Figure 3.11: Vorticity distribution overlaid with velocity vectors around the rigid foil with $k = 0.083$, $\theta_0 = 45°$, and $\Phi = 90°$.

shear in the flow direction. This elevated shear layer feeds the vortex structure at a heightened rate, resulting in quicker formation and detachment of the vortex from the foil. At $k = 0.083$, the LEV is attached to the surface at only two phases in the half cycle. Consequently, this decreases attachment time of the LEV and leads to diminished forces. Because the intention is to utilize the high lift from the LEV throughout the duration of the half cycle, it is advantageous to impede the LEV growth at k below 0.15 such that the LEV maintains attachment for a prolonged period of time. This sustained attachment will yield higher energy harvesting performance as the foil advances through the oscillation cycle.

3.3.2 Influence of Parameter Space on the Flow Structure

Using these observations, the contributions of the flow field on the energy harvesting performance of the oscillating foil over the broader parameter space can be discussed. The influence of ranging Φ from 75° to 105°, increasing θ_0 from 45° to 60° and 75°, and decreasing k from 0.083 to 0.063 and 0.042 are investigated using the PIV measurements. In a manner similar to Sections 3.2.2.1, 3.2.2.2, and 3.2.2.3, Sections 3.3.2.1, 3.3.2.2, and 3.3.2.3 discusses the contributions of Φ, θ_0, and k on the overall flow field, respectively. Because of the large amount of flow field data, the results in this section focus on t/T where the LEV has been shown to contribute to energy harvesting for the optimal case tested in this study. These t/T values are: 2/16, 3/16, 4/16, and 5/16. For all t/T in the parameter space listed in Table 2.3, refer to Appendix G.

3.3.2.1 Phase

The influence of the motion phase Φ on the flow structure evolution is shown in Fig. 3.12, where the top row corresponds to $\Phi = 75°$, $\Phi = 90°$ is in the middle row, and $\Phi = 105°$ is in the bottom row. For each t/T in the cycle, it can be seen that larger phase delays between the pitch and heave motions result in earlier development of the LEV structure. For example, when $\Phi = 75°$ and $t/T = 2/16$, no LEV is detected, whereas at a Φ of 105° at the same t/T shows a clear LEV structure at roughly $0.25c$ down the foil chord. Additionally, the LEV at $\Phi = 105°$ and $t/T = 2/16$ closely resembles the LEV detected when $\Phi = 90°$ and $t/T = 3/16$ as well as $\Phi = 75°$ and $t/T = 4/16$. This implies that

Φ plays a significant role in the formation and timing on the LEV structure. It should be noted that these flow fields are not expected to be identical because of the slight difference between Φ and t/T, where Φ is varied by 15° and t/T varies by 22.5° (1/16 of a full cycle).

It is interesting to note that the strength and size of the LEV does not significantly vary for Φ near 90°. This observation can again be attributed to the low heaving velocity relative to the free stream flow speed. Because of the large flow speed, vorticity is fed into the LEV at an elevated rate compared to the optimal $k = 0.15$ condition so long as the foil has an effective angle of attack past stall. Consequently, the LEV forms early in the motion cycle and is thus fairly independent of the heaving motion contributions. The implication of this is that controlling the phase shift between the pitch and heave motions does not change the force curve shape or magnitudes significantly, but instead simply shifts the force timing by the specified motion phase.

In order to assess the validity of this discussion, these observations are supported by lift data trends. The relevant force trends are shown in Fig. 3.9 (a), which corresponds to the following operating parameters: $\theta_0 = 45°$, $k = 0.083$, and Φ ranging from 75°, 90°, and 105°. As discussed in Section 3.2.2.1, the motion phase was shown to not significantly alter the lift history shape or magnitude but instead control the timing of the lift curves relative to the foil motion. This directly supports the trends observed and discussed from the flow field data, where Φ simply controls the timing of the LEV but has little influence on the growth rate or detachment time of the vortex. Additionally, the trends observed in the flow field are assumed to also hold true for increased θ_0 as they do in the aerodynamic lift curves.

3.3.2.2 Pitching Angle

By increasing the pitching angle of the foil, the effective angle of attack is also increased throughout the motion cycle. This increased pitching angle has a significant influence on the development of the LEV and thus the resulting flow field characteristics, as seen in Fig. 3.13. As the pitching angle is increased, the LEV develops earlier in the motion cycle which is clearly seen when looking at any single t/T. For example, consider $t/T = 3/16$. When $\theta_0 = 45°$, the LEV is closely attached to the foil surface and is near its maximum strength resulting in near peak lift force. However, when $\theta_0 = 75°$, the LEV has already

begun its detachment from the shear layer resulting in an overall decreased strength. The LEV is also located further away from the foil surface. Because of this, it is expected that the decreased strength and increased distance from the foil will result in decreased lift at $t/T = 3/16$ compared to $\theta_0 = 45°$, which is confirmed with Fig. 3.10 (d).

Additionally, two other observations from the lift curves of Fig. 3.10 (d) need to be discussed using the flow field results. These two observations include the increased peak lift as well as the two-peak lift distribution in the lift history when $\theta_0 = 75°$. In order to explore these trends, the flow vorticity distribution and velocity vectors should be compared between $\theta_0 = 45°$ and $\theta_0 = 75°$ for additional t/T not shown in Fig. 3.13. This is shown in Fig. 3.14, where t/T from 0/16 to 7/16 are shown for both θ_0.

From Fig. 3.10 (d), the peak lift for $\theta_0 = 45°$ occurs between $t/T = 2/16$ and 3/16, whereas peak lift occurs between $t/T = 1/16$ and 2/16 for $\theta_0 = 75°$. In terms of the flow field results of Fig. 3.14, the LEV is expected to achieve peak strength and reside near the foil surface at these t/T. The distinguishing characteristic between these two θ_0 is that the LEV has increased vorticity when $\theta_0 = 75°$, resulting in larger peak lift forces. However, the LEV detaches itself from the foil surface earlier in the motion cycle compared to the $\theta_0 = 45°$ case, resulting in a quick loss of lift force throughout the rest of the motion cycle. Additionally, the earlier development and detachment of the LEV when $\theta_0 = 75°$ results in the de-synchronization of the lift forces and foil heaving velocity. Between $t/T = 4/16$ and 5/16, which corresponds to the cycle time where peak foil velocity occurs, lift forces are substantially reduced even when compared with $\theta_0 = 45°$.

The secondary peak in the lift forces for $\theta = 75°$ does not surpass the lift of the $\theta_0 = 45°$ curve (at $t/T = 6/16$). Because of this, the overall cycle lift is reduced with increasing θ_0 and loses synchronization with the foil heaving velocity, resulting in drastically lower overall energy harvesting efficiencies. Nonetheless, the presence of this secondary bump helps keep cycle efficiencies from decreasing below 9% when $k = 0.083$. This peak appears to be a result of the increased shear on the foil surface near the LE between $t/T = 5/16$ to 7/16, which results in a small clockwise-rotating vortex. This vortex acts in a similar manner as the LEV, where the increased flow velocity results in a low pressure region. Because the low pressure vortex core is located near the foil surface, the contributions of this vortex are detected by the foil load cells resulting in this secondary peak.

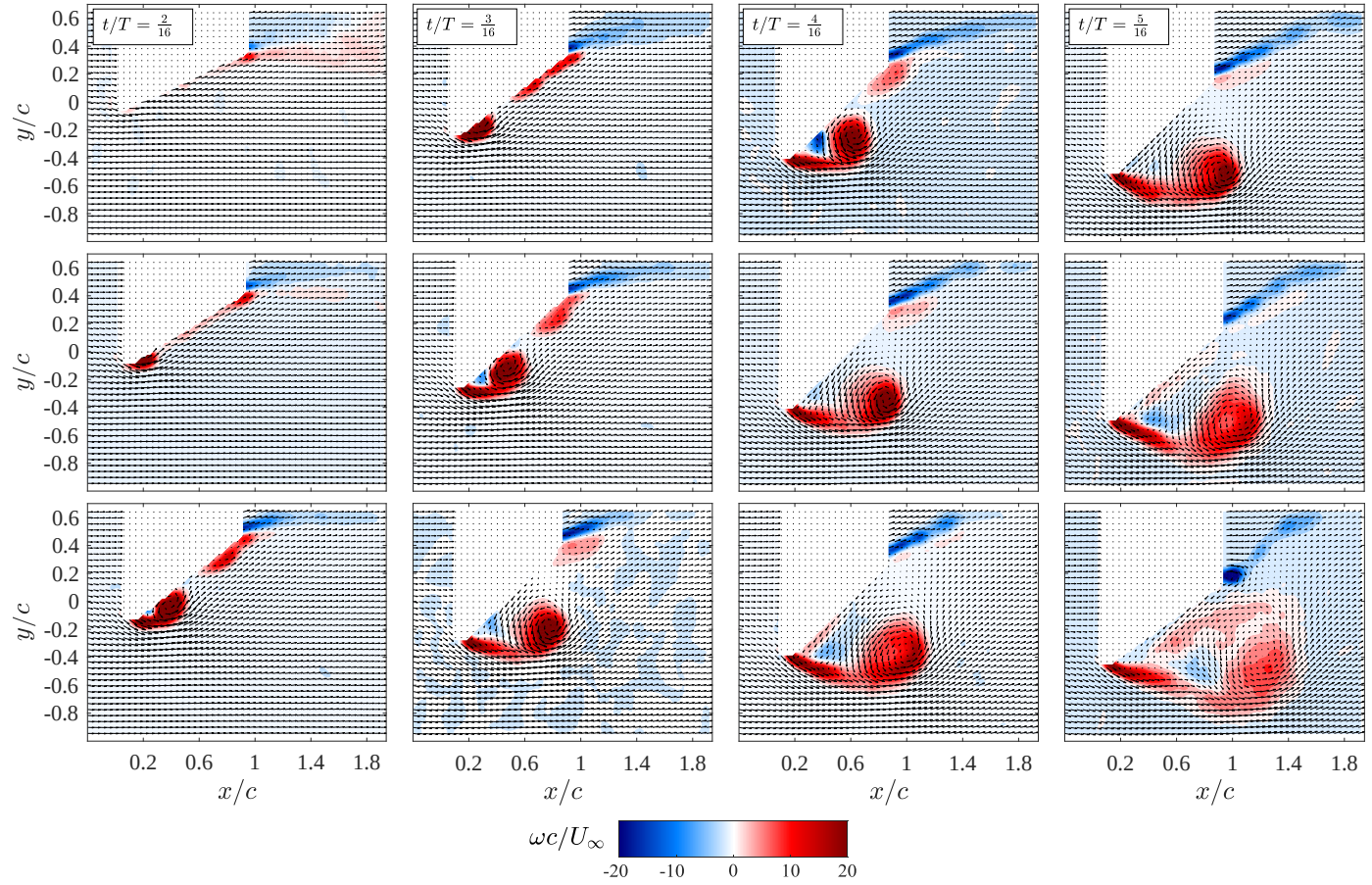

Figure 3.12: Vorticity distribution overlaid with velocity vectors around the rigid foil with $k = 0.083$, $\theta_0 = 45°$, and $\Phi = 75°$ (top row), $90°$ (middle row), and $105°$ (bottom row).

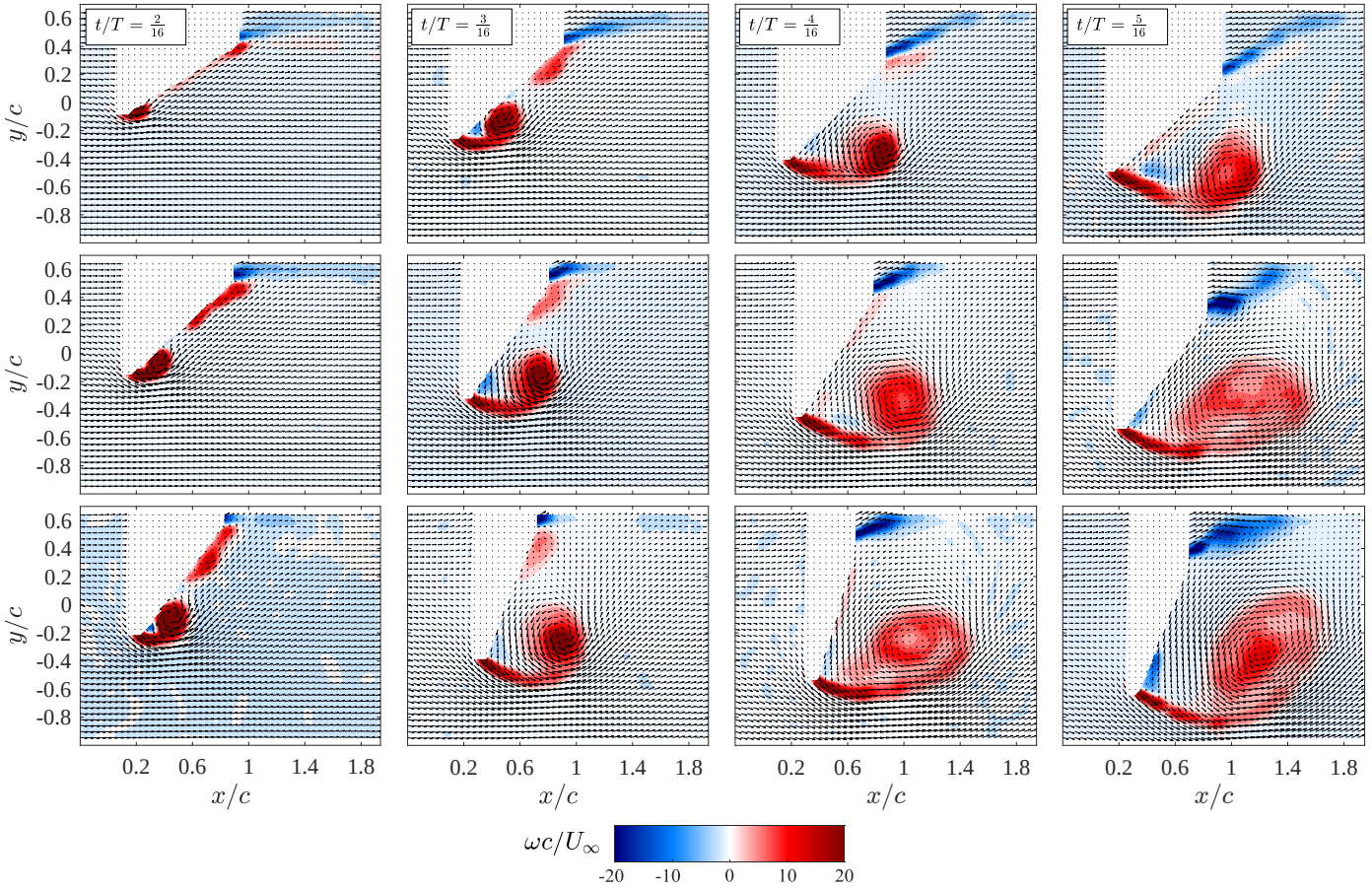

Figure 3.13: Vorticity distribution overlaid with velocity vectors around the rigid foil with $k = 0.083$, $\Phi = 90°$, and $\theta_0 = 45°$ (top row), $60°$ (middle row), and $75°$ (bottom row).

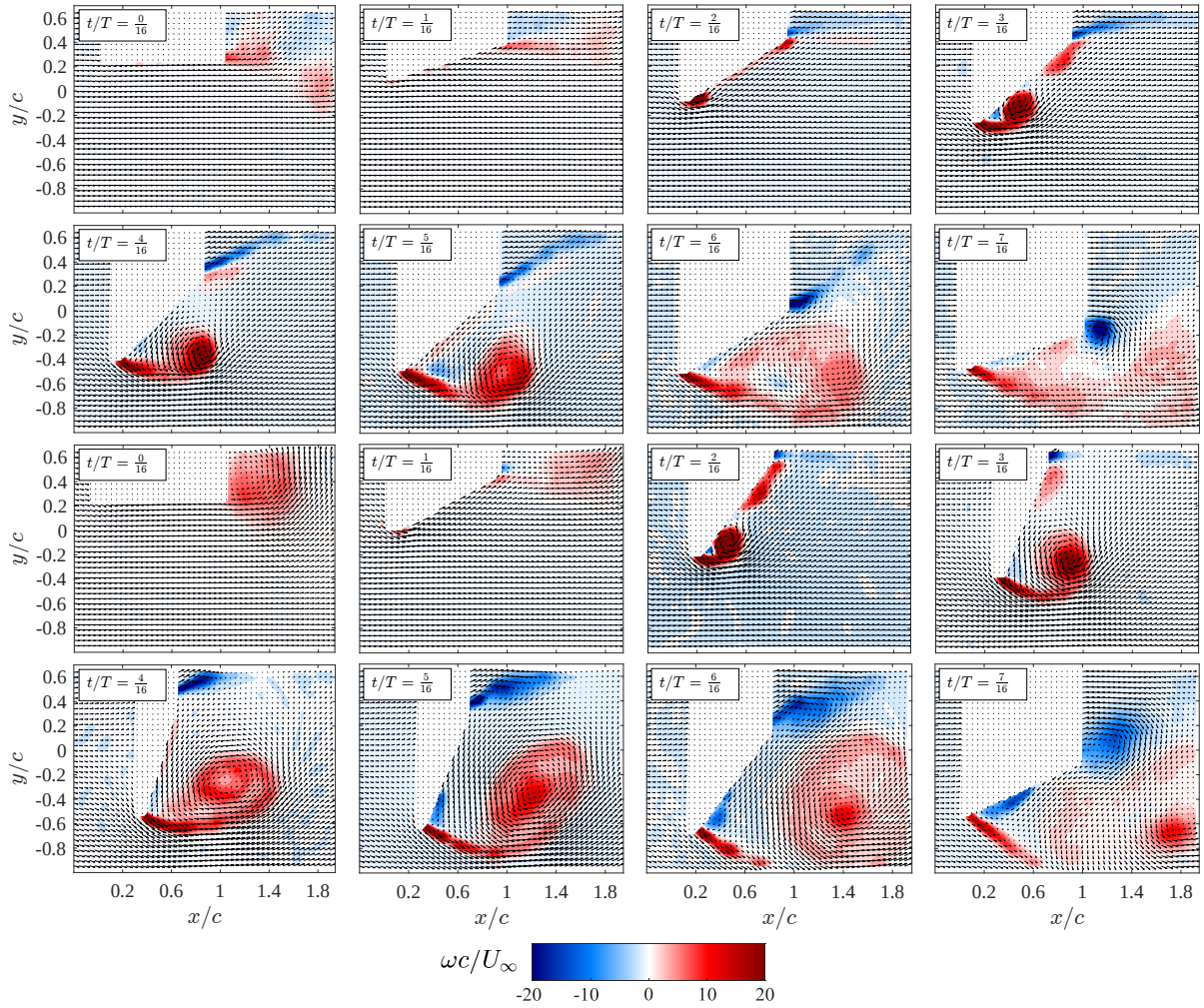

Figure 3.14: Vorticity distribution overlaid with velocity vectors around the rigid foil with $k = 0.083$, $\Phi = 90°$, and $\theta_0 = 45°$ (top 2 rows), $75°$ (bottom 2 rows) for t/T from 0/16 to 7/16.

3.3.2.3 Reduced Frequency

The phase averaged vorticity is also shown for the three reduced frequencies tested in Fig. 3.15. Again, only $t/T = 2/16$ to $5/16$ are shown in this figure in order to clearly show the LEV development process. For results showing t/T from $0/16$ to $7/16$, refer to Appendix G. Additionally, only data where $\theta_0 = 45°$ and $\Phi = 90°$ are shown in order to provide a clear comparison across the three k about the highest performing case tested in this study.

As k is decreased from $k = 0.083$ to 0.042, three observations are made. The first observation is that a decrease in k (through an increase in U_∞) results in quicker LEV development and detachment. Because the incoming flow is faster and contains more energy, the resulting shear layer at the LE of the foil supplies energy to the LEV at an elevated rate. This increased feeding rate then results in a stronger LEV that develops earlier in the motion cycle, similar to the trends discussed where θ_0 and Φ were varied over the parameter space. The second observation is that a decrease in k results in fully separated regions occurring earlier on in the cycle, where $t/T =$ ranges from $4/16$ to $5/16$. The shear layer bounding the separation region shows increased vorticity as k is decreased and develops a distinct trailing edge vortex (TEV) similar to that of the LEV. This TEV quickly grows and sheds into the wake well before the foil reaches the bottom heaving position. The third observation is that a decrease in k also results in a more pronounced clockwise rotating vortex between the LEV and the foil surface. The combined effects of this secondary vortex and the TEV may also contribute to the development of a secondary peak in the C_L curves, as the secondary peaks are not present when there is no clear TEV or secondary vortex.

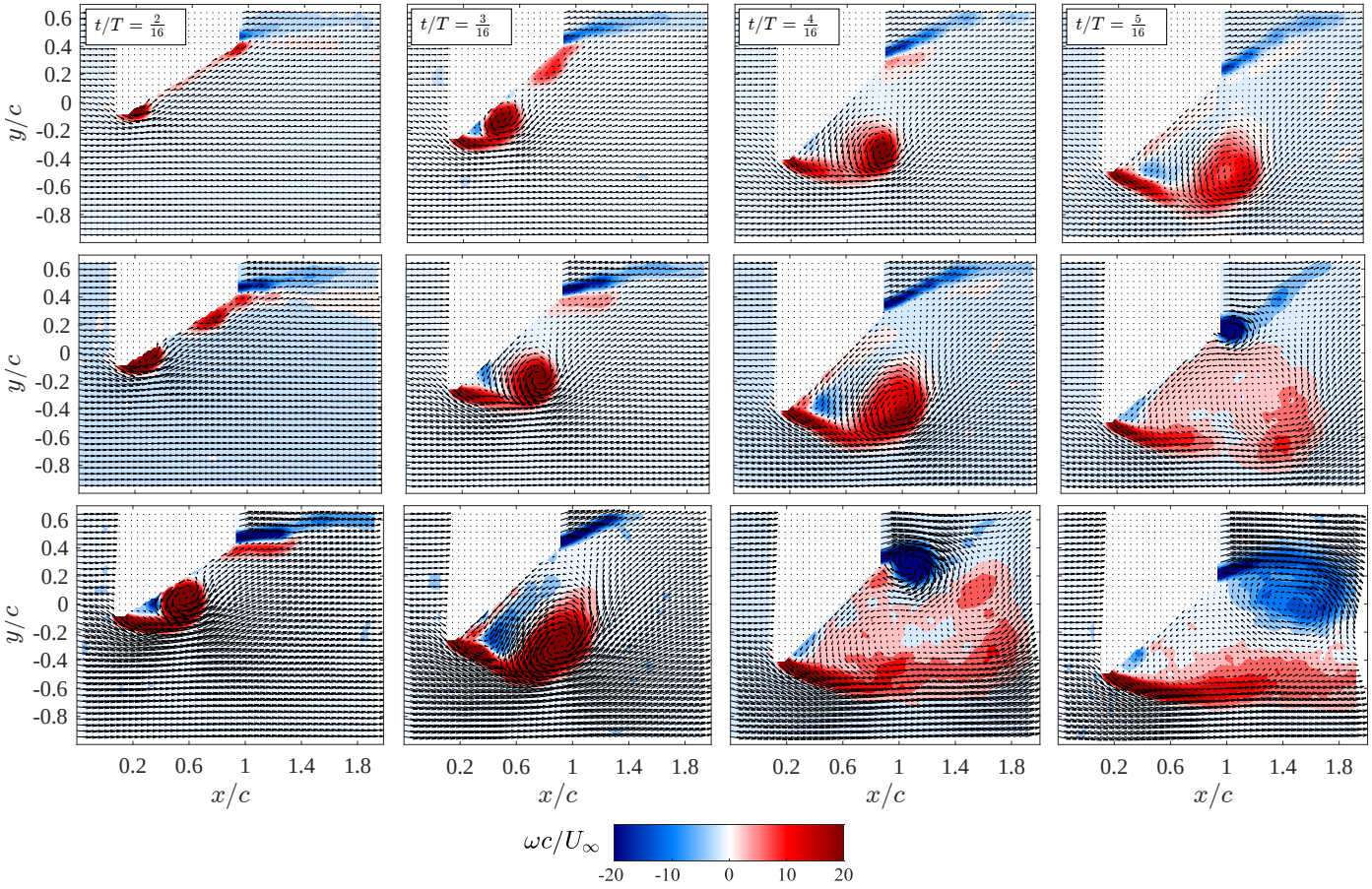

Figure 3.15: Vorticity distribution overlaid with velocity vectors around the rigid foil with $\theta_0 = 45°$, $\Phi = 90°$, and $k = 0.083$ (top row), 0.063 (middle row), and 0.042 (bottom row).

3.4 Flexible Foil Performance

In this section, force measurements and PIV data are presented for the three foil configurations. These conditions correspond to the flexible LE where $\kappa = \infty$, 0.13 $N-m/rad$, and 0.07 $N-m/rad$. Results are compared against the rigid foil configuration ($\kappa = \infty$) as a baseline. For flexible LE force and PIV measurements, the reduced frequency was fixed at $k = 0.042$ in order to decrease the uncertainty in the force measurements. This was necessary because the uncertainties when $k = 0.083$ were fairly large, and the increased degree of freedom of the foil motion (the flexible LE) was expected to increase the uncertainty. Therefore, to get more reliable measurements when the LE is allowed to passively flap, it was deemed necessary to increase the free stream flow speed.

The remainder of this section is organized according to the following: Section 3.4.1 discusses the performance of the three flexible LE configurations in terms of the extraction efficiency and power coefficient. Then, Section 3.4.2 shows the C_L curves along with the foil heaving velocity in order to better understand the contributions of the flexible edges on the cycle lift. Section 3.4.3 then shows the flow vorticity and velocity vectors obtained from PIV measurements. The goal here is to use the flow field along with the foil motion in order to understand why the resulting force trends occur. Finally, Section 3.4.4 provides some concluding remarks in regards to the flexible LE contributions and its potential uses. Note that not all force and PIV measurements collected for the flexible foil configurations are presented in this section. For all flexible LE force measurement data and PIV measurements, refer to Appendices H and I, respectively.

3.4.1 Efficiency and Power

The energy extraction efficiency for the three foil configurations is shown in Fig. 3.16. In addition to the three flexibility conditions, pitching amplitudes of $\theta_0 = 45°$, $60°$, and $75°$ are shown, similar to Fig. 3.3. As the pitching angle is increased, the energy extraction efficiency decreases regardless of the LE configuration. However, the sensitivity of the extraction efficiency is decreased as more passive flexibility at the LE is introduced. This result is similar to the trends seen in Fig. 3.3, where the sensitivity to the energy harvesting efficiency is reduced as k is decreased. The root cause of this for the rigid foil originates from the elevated shear feeding rate into the LEV from the LE. With an

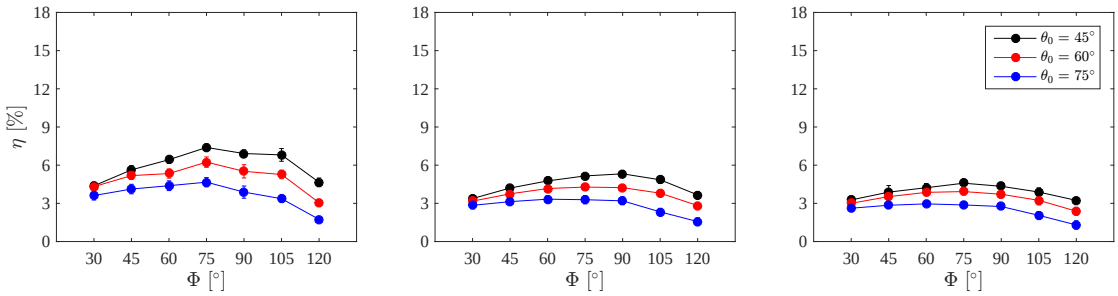

(a) (b) (c)

Figure 3.16: Energy extraction efficiency versus motion phase for $\kappa =$ (a) ∞, (b) 0.13 $N-m/rad$, (c) 0.07 $N-m/rad$. Additionally, three pitching angles of $\theta_0 = 45°$, $60°$, and $75°$ are shown in each sub-figure.

increased feeding rate into the LEV, the LEV detaches from the foil surface early in the cycle leading to reduced performance. The increased effective angle of the foil from the passive flapping of the LE is expected to elevate the feeding shear layer resulting in premature LEV detachment from the foil surface, and thus, reduced extraction efficiency as well as reduced sensitivity.

The corresponding power coefficients for the three foil configurations when $k = 0.042$ is shown in Fig. 3.17. Again, similar trends are observed between the rigid and flexible LE cases, where $\theta_0 = 45°$ yields the highest overall power extraction, and energy harvesting decreases with increasing θ_0. In addition, C_P becomes less sensitive to the operating parameters when the degree of LE flexibility is increased. Therefore, the degree of energy harvesting as well as the efficiency of extraction decrease with increasing LE flexibility. However, it is important to note that the LE obtains passive flexibility through inertially induced deflection from the foil motion. Because of this, the LE deflection timing and amplitude may not occur in a manner which would result in enhanced energy harvesting. Thus it is useful to investigate the lift curves along with the foil motion in order to determine why the power extraction decreases with LE flexibility.

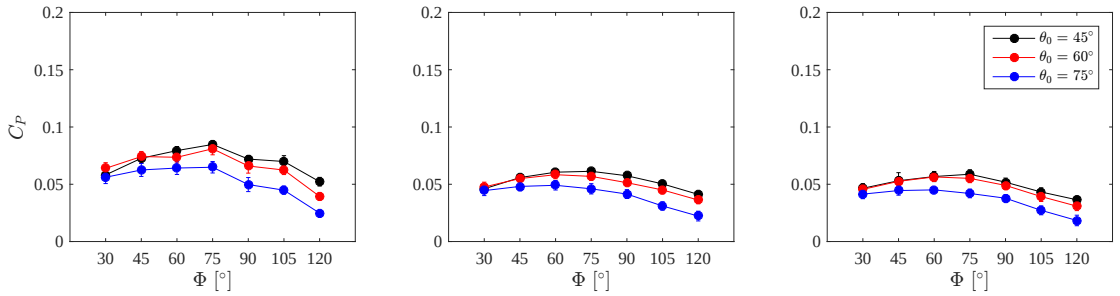

(a) (b) (c)

Figure 3.17: The power coefficient versus motion phase for κ = (a) ∞, (b) 0.13 $N - m/rad$, (c) 0.07 $N - m/rad$. Additionally, three pitching angles of $\theta_0 = 45°$, $60°$, and $75°$ are shown in each sub-figure.

3.4.2 Lift Curves

The energy harvesting capabilities of an oscillating foil operating at $k = 0.042$ shows a decrease in both energy extraction and efficiency when the LE is allowed to passively actuate due to inertia. Although some of these trends have been explained already using observations from Sections 3.2 and 3.3, again, it is useful to look at the force curves in order to determine the influence of LE flexibility on the force time history. These lift curves are shown in Fig. 3.18, where C_L is shown throughout the oscillation cycle with varying Φ, θ_0, and κ.

By looking at the three rows in Fig. 3.18, the influence of the motion phase Φ is shown. The top, middle, and bottom rows correspond to $\Phi = 75°$, $90°$, and $105°$, respectively. As can be seen, the influence of Φ is the same as discussed in Section 3.2.2.1, where Φ simply controls the timing of the force curves relative to the heaving motion of the foil. However, this is only true for Φ between approximately $45°$ to $105°$. For values of Φ outside of this range, the peak force magnitudes begin to deviate and in some cases the force history shape changes altogether. Additionally, as flexibility is introduced at the LE, Φ still acts as a time shifting mechanism, controlling the time lag between the force curves and the foil motion. Thus the flexible LE condition does not have a significant contribution to the overall force timing relative to the heaving motion. Because these results are similar to the results of the rigid foil, the influence of the motion phase is not discussed any further.

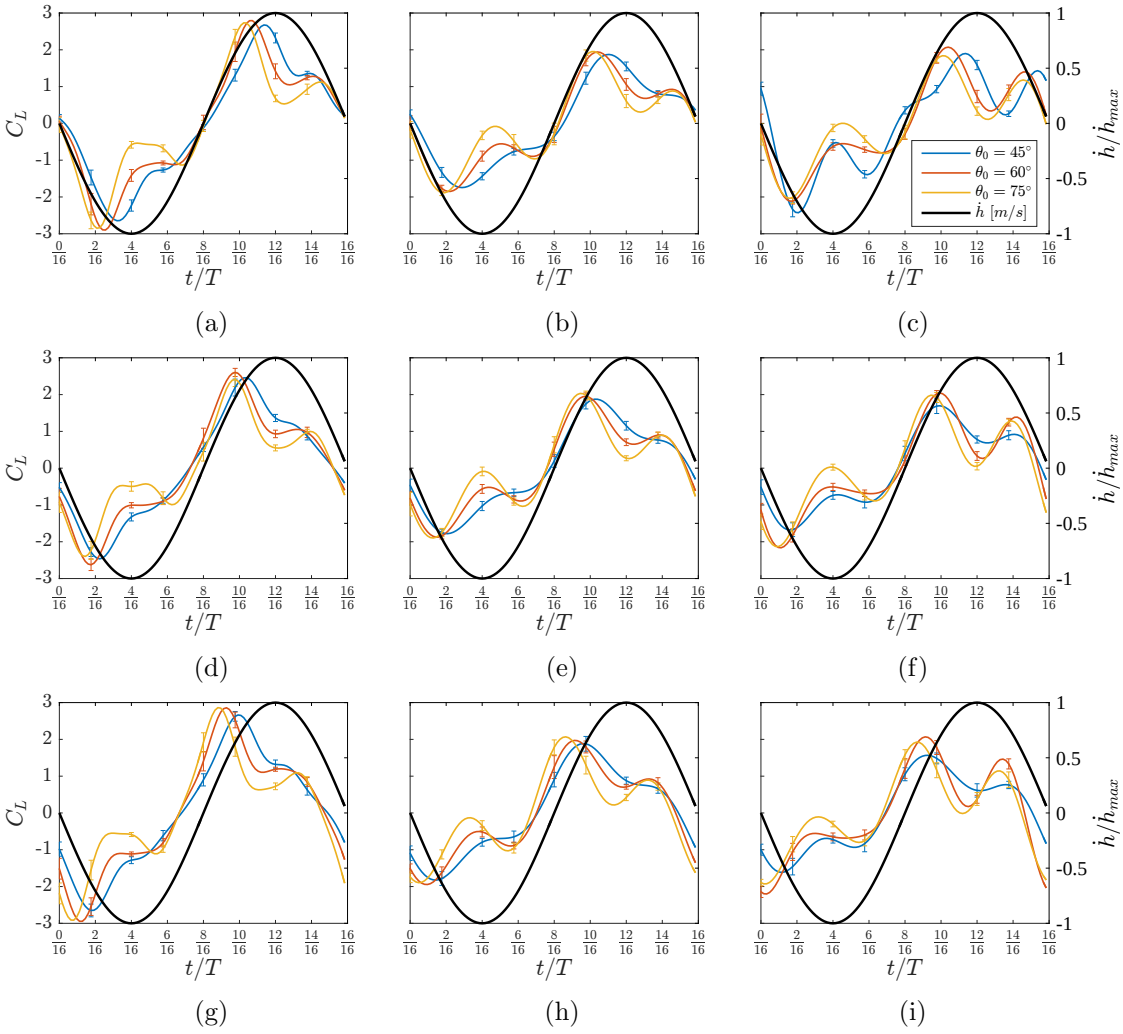

Figure 3.18: Lift coefficient versus the cycle period for $k = 0.042$. The rows correspond to changing Φ, where the top, middle, bottom rows are for $\Phi = 75°$, $90°$, and $105°$, respectively. The columns correspond to changing the foil flexibility configuration, where the left, middle, and right columns are for the $\kappa = \infty$, 0.13, and 0.07 configurations, respectively. θ_0 of 45°, 60°, and 75° are shown.

As θ_0 is increased from 45° to 75°, the secondary peaks in C_L are still present. However, as LE flexibility is increased, the contributions of increasing θ_0 show diminishing changes in the C_L curves. This means that as LE flexibility is increased, the force trends become less sensitive to changing θ_0. Therefore, θ_0 does not play a significant role at $k = 0.042$ when LE flexibility is present, and the degree of LE flexibility seems to dominate the force curve development. As such, the contributions of LE flexibility can now be discussed.

The most striking observation pertaining to the flexible LE measurements is that the peak forces in the C_L curves decrease with added flexibility. This is counter-intuitive, as the increase in the effective foil angle of attack should yield a increase in peak forces, particularly as this is leveraged through dynamic stall. However, this is not the case and a substantial decrease in lift is observed for $\kappa = 0.13\ N - m/rad$ and $0.07\ N - m/rad$. This results in a decreased extraction performance of the foil.

Additionally, the secondary peak present in each half cycle gains prominence as flexibility is increased. Although the lift at this secondary peak increases with flexibility, the overall energy harvesting performance of the foil decreases. This is likely attributed to two things. Consider the case of Fig. 3.18 (f), when $\Phi = 90°$. First, the primary and secondary peaks in each half cycle are located approximately $\pm 2/16\ t/T$ out of phase with the foil heaving velocity. Therefore any increase in force magnitude at these locations will not result in significant performance gains. Secondly, the valley present between the two peaks is increased in magnitude, i.e. the valley has a lower minima. When $\Phi = 90°$, this minimum is also located at $t/T = 12/16$, which is the point of maximum foil velocity. Thus the decrease in lift when the foil motion has the largest velocity results in a large decrease in extraction performance, outweighing the contribution of the increased lift at the secondary peak.

3.4.3 Flow Field Measurements

For the rigid foil configuration, peak energy extraction efficiency occurs when $\theta_0 = 45°$, $\Phi = 90°$, and $k = 0.083$, and peak energy extraction occurs when $\theta_0 = 60°$, $\Phi = 60°$, and $k = 0.083$. However, PIV data for the flexible LE configurations were not collected at $k = 0.083$, but instead were collected at $k = 0.042$. There are a number of reasons for this which are not discussed here. As such, this section presents PIV results pertaining

to the same operating conditions as the peak performance cases of the rigid foil, but at lowered k of 0.042.

The flow vorticity and velocity vectors are shown in Fig. 3.19 for $\theta_0 = 45°$, $\Phi = 90°$, and $k = 0.042$ at all t/T in the half cycle. This corresponds to the force measurements represented by the blue lines in Fig. 3.18 (d) and (e). At this operating point, the flexible LE case where $\kappa = 0.07\ N - m/rad$ results in sporadic and unrepeatable LE deflection. Because of this, PIV measurements for the $\kappa = 0.13\ N - m/rad$ LE condition only is investigated here. Although the degree of LE flexibility when $\kappa = 0.13\ N - m/rad$ is fairly small, changes in the flow development are evident.

The general flow topology is fairly similar, where $t/T = 1/16$ to $2/16$ pertain to the LEV formation and growth, $t/T = 3/16$ is near the LEV detachment point, and $t/T = 4/16$ to $7/16$ show fully separated flow. However, the LEV evolution when $\kappa = 0.13\ N - m/rad$ is slightly earlier in time relative to the rigid foil. When looking at $t/T = 2/16$, it is clearly seen that the LEV has already departed from the foil surface for the $\kappa = 0.13\ N - m/rad$ configuration, whereas the LEV is still near the foil when $\kappa = \infty$. This point corresponds to the peak loading on the foil, however because the LEV develops earlier in the cycle when $\kappa = 0.13\ N - m/rad$, the maximum loads reached are roughly 27% smaller than when $\kappa = \infty$. Therefore, the peak loads for an inertially induced passive LE deflection are decreased due to the premature LEV development and detachment.

The secondary peak present in the force measurements does not significantly change between the $\kappa = \infty$ and $\kappa = 0.13\ N - m/rad$ conditions at this operating point. In terms of the flow evolution, there is no clear difference between the two foil configurations at $t/T = 6/16$, which corresponds to the point where the secondary peaks appear. However, a decrease in C_L of 22% is seen at the $t/T = 4/16$ position between the two flexibilities, which corresponds to the valley between the two peaks. Looking at the flow field at this t/T, the TEV is significantly larger for the flexible LE condition. Thus, the presence of a TEV appears to decrease the loads at the $t/T = 4/16$ position in the cycle, which corresponds to peak foil velocity. As the TEV grows in size and strength, flow is entrained by the TEV and directed upward towards the bottom surface of the foil, impinging on the foil surface as the foil heaves downward. This in turn decreases the overall lift generated in the negative y direction, as the pressure is increased on the bottom side of the foil, resulting in a decrease in total pressure differential across the top and bottom surfaces.

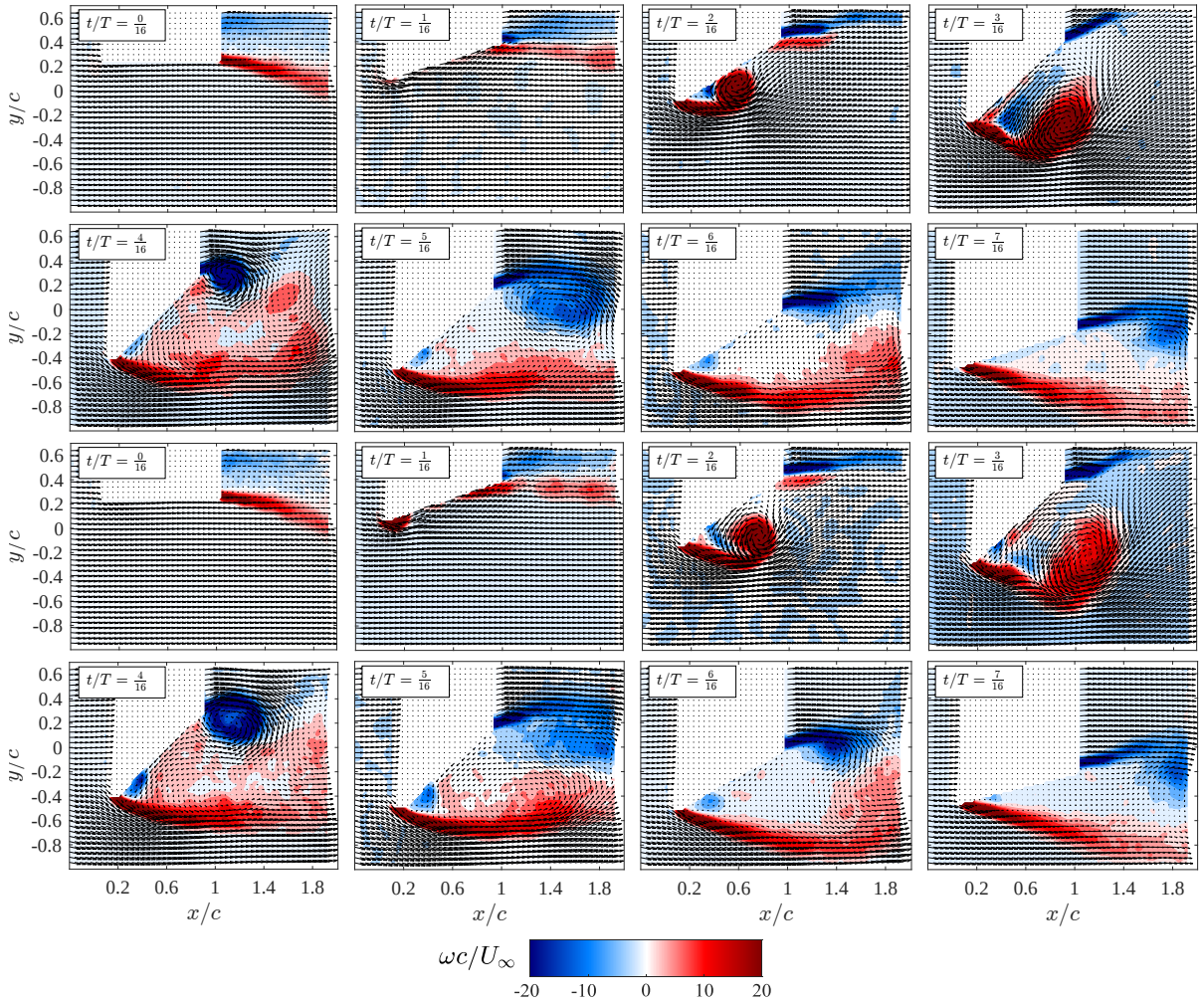

Figure 3.19: Vorticity distribution overlaid with velocity vectors for the $\kappa = \infty$ (top 2 rows) and $\kappa = 0.13\ N{-}m/rad$ (bottom 2 rows) foil configurations. Additionally, $k = 0.042$, $\Phi = 90°$, and $\theta_0 = 45°$ for t/T from 0/16 to 7/16.

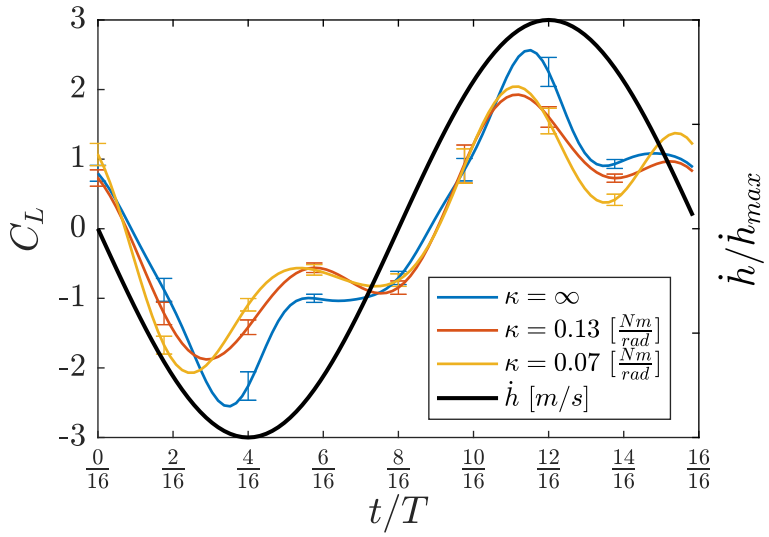

Figure 3.20: Lift coefficients for $\theta_0 = 60°$, $\Phi = 60°$, $k = 0.042$, and the three foil configurations. The three foil configurations are: $\kappa = \infty$ (rigid), $\kappa = 0.13\ N - m/rad$, and $\kappa = 0.07\ N - m/rad$.

As such, in order to obtain reasonable energy harvesting efficiency at low k, this TEV should be suppressed such that the lift forces are not significantly decreased by this redirection of flow.

Before discussing the results of the higher power extraction case ($\theta_0 = 60°$, $\Phi = 60°$), the lift curves must be presented as they have not been discussed for $\Phi = 60°$. Figure 3.20 shows the C_L curves for the $\theta_0 = 60°$, $\Phi = 60°$, and $k = 0.042$ operating point, which corresponds to the lower k variant of the peak power extraction parameter space. As can be seen, the flexible LE does play a significant role in the C_L curves. Peak lift forces are shown to decrease as the degree of flexibility increases, and the presence of a secondary peak becomes more prominent. This is similar to the previous discussion in Section 3.4.2, indicating that the added flexibility results in overall lower energy harvesting performance. However, the flow field at this operating case shows some interesting trends that need to be discussed.

The vorticity distributions for the $\theta_0 = 60°$, $\Phi = 60°$, and $k = 0.042$ case are shown in Fig. 3.21, where the top, middle, and bottom rows correspond to the $\kappa = \infty$, $\kappa = 0.13\ N - m/rad$, and $\kappa = 0.07\ N - m/rad$ foil flexibility conditions, respectively.

Starting with the $\kappa = \infty$ case, the LEV is nearly fully developed by the $t/T = 3/16$ time in the cycle which is similar to trends discussed before. However, instead of a clear separation zone occurring at the $t/T = 4/16$ and $5/16$ mark, a strong TEV forms and pulls the LEV back towards the foil. This results in severe stretching of the LEV, decreasing the vorticity magnitude of the LEV. Because the TEV is much stronger than the stretched out LEV, the lift at $t/T = 5/16$ still decreases resulting in a small valley in the C_L curves.

When $\kappa = 0.013\ N - m/rad$, the LEV evolution is very similar to that of the rigid foil, but slightly expedited. The biggest variation in LEV development can be seen when $\kappa = 0.07\ N - m/rad$. With this degree of flexibility, the LEV rapidly forms before the $t/T = 2/16$ time in the cycle. This occurs because of the added angle the LE is generating for the overall foil pitch (note the masked out region near the LE is angles downward slightly). As a result, the LEV is fully developed and detached from the foil surface by $t/T = 3/16$. The LEV then stretches and completely disperses into the foil wake. Because the LEV is no longer coherently pulled toward the foil surface by the TEV, only the contributions from the TEV are felt on the foil. As such, the valley in the C_L curve becomes more pronounced due to the decreased lift forces. In terms of the power extraction performance, this has a negative contribution and results in lower C_P.

3.4.4 Further Discussion

The results in this section show that for $k = 0.042$, the LEV develops and departs from the foil surface early on in the motion cycle, before the foil achieves peak velocity. With the addition of LE deformation, the LEV develops even more quickly. Although some degree of surface deformation has been shown to drastically improve the energy harvesting performance of oscillating foils near the $k = 0.15$ range, a majority of these studies were performed computationally with a specified LE deflection trajectory. However, with an inertially induced, passive LE deflection where $\kappa = 0.13\ N-m/rad$ and $0.07\ N-m/rad$, the timing of the LE deflection is such that it aids LEV growth. This is actually contradictory to what is required for k in the range of 0.083 to 0.042, since the LEV already develops so quickly.

Therefore, the intention of including LE deflection should be such that it delays the detachment time of the LEV. This will in turn allow the LEV to grow larger and stronger,

as the shear layer from the LE will continue to supply vorticity into the vortex. The combined effect of a stronger LEV and decreased distance between the LEV and the foil will result in larger sustained lift forces along the foil as the foil undergoes the heaving motion. As a result, peak energy extraction and energy harvesting efficiency will increase at these lower k values. The main issue, is then, how to control the LE deflection.

There are a multitude of methods to achieve LE deflection, however here are three possible combinations. The first, is to utilize driven motion control in order to generate the desired LE trajectory throughout the foil motion. This may be more practical during the application of these energy harvesting systems in order to compensate for the dynamically varying water or air currents. As the free stream flow speeds change, the degree of LE deflection can be varied using a feedback system such that LEV growth is enhanced while maintaining attachment of the LEV to the foil surface. The second method is using a fully passive system where a combination of spring and dampers are used to control the degree of deflection as well as the response time of the deflection. This is similar to the case used here, where the torsion rod acts as the spring component and the LE mass acts as the damper. However, careful selection of spring components, foil materials, or more complex configurations involving additional springs or dampers can be used to generate an ideal LE deflection for a narrow range of free stream currents. A third possible method is the use of a combined passive-controlled LE deflection. For example, a spring allowing large LE deflection passively can be used with a controlled variable damping system. By varying the degree of damping, the amplitude and timing of the LE deflection can be controlled in order to achieve the desired LE profile.

These results show promise that reasonable energy harvesting at lower k is a possibility. Through careful selection of LE parameters, the LE may be used as a tuning mechanism to achieve favorable LEV development and detachment.

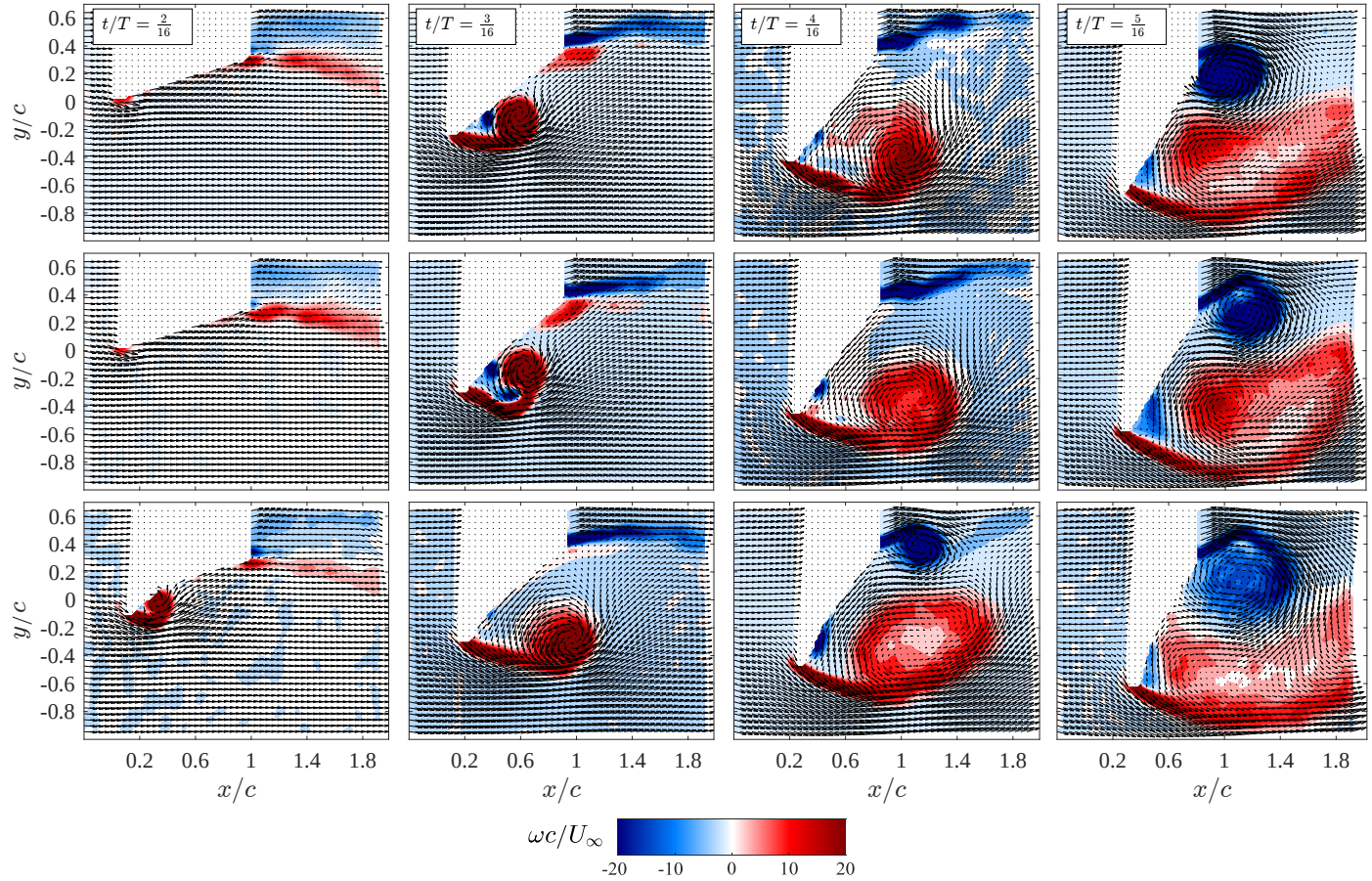

Figure 3.21: Vorticity distribution overlaid with velocity vectors for the $\kappa = \infty$ (top row), $\kappa = 0.13\ N - m/rad$ (middle row), and $\kappa = 0.07\ N - m/rad$ (bottom row) foil configurations. Additionally, $k = 0.042$, $\Phi = 60°$, and $\theta_0 = 60°$ for t/T from 0/16 to 7/16.

Chapter 4: Summary and Conclusions

Wind tunnel experiments of an oscillating foil energy converter (OFEC) device were conducted. In these experiments, direct force measurements of the aerodynamic loading on the oscillating foil were collected in order to quantify the energy extraction and energy extraction efficiency of the OFEC system. Additionally, flow field measurements were collected using particle image velocimetry (PIV) in order to visualize the flow fields which result in various force trends. This approach is used to qualitatively assess the flow contributions which lead to efficient OFEC performance, and provides insight as to how these systems should be designed in order to generate efficient energy harvesting. These force and PIV measurements were then used to investigate the contributions of inertially-induced passive surface deformation at the leading edge of the oscillating foil. This work, to the best of the author's knowledge, is the first of its kind in which passive surface deformation is experimentally investigated for an OFEC system. As a result of this work, the following conclusions are drawn:

1. Under the parameters considered, overall extraction efficiencies are fairly low, with a maximum efficiency of $\eta = 15.5\%$, and a maximum power coefficient of $C_P = 0.173$. An increase in OFEC performance tends towards lower pitching angles ($\theta_0 = 45°$) and higher reduced frequency ($k = 0.083$).

2. Increased energy harvesting occurs by keeping the leading edge vortex (LEV) close to the foil surface for as long as possible throughout the oscillation cycle. To a degree, the strength of the LEV isn't as important as the proximity of the LEV to the foil surface.

3. The timing of the LEV formation, evolution, and separation is vital for increased energy harvesting. At reduced frequencies in the range of $0.042 \leq k \leq 0.083$, the LEV develops and sheds from the foil surface early on in the oscillation cycle. Therefore, at these k values, efforts should focus on delaying the LEV formation such that it does not shed from the foil surface prematurely. This will enhance

the energy extracted by the foil as the lift force will be increased and sustained throughout more of the motion cycle.

4. Inertially-induced, passive surface deformation at the leading edge of an oscillating foil has negative contribution to the overall energy harvesting performance at low reduced frequencies. This is due to the LEV departing from the foil surface at earlier times in the motion cycle.

5. For enhanced energy harvesting, passive flexibility at the leading edge in this range of k should be used to delay LEV detachment, and not necessarily aid its growth. This will allow the LEV to grow larger and stronger, as well as maintain its proximity to the foil surface for a prolonged period of time, due to the delayed detachment of the LEV. As a result, the lift forces and thus energy harvesting performance will increase.

6. The proper tuning of leading edge deflection is necessary in order to enhance energy extraction. This can be accomplished in a variety of ways, some of which include: implement full control of the leading edge deformation such that it delays premature detachment, use a completely passive system of springs and dampers which control the amplitude and response time of leading edge deflection, or use a combination of passive and controlled leading edge deformation through variable spring rates or damping.

Bibliography

[1] Hisanori Abiru and Akira Yoshitake. Study on a flapping wing hydroelectric power generation system. *Journal of Environment and Engineering*, 6(1):178–186, 2011.

[2] MA Ashraf, J Young, JC S. Lai, and MF Platzer. Numerical analysis of an oscillating-wing wind and hydropower generator. *AIAA journal*, 49(7):1374–1386, 2011.

[3] Tommaso Astarita. Analysis of interpolation schemes for image deformation methods in piv: effect of noise on the accuracy and spatial resolution. *Experiments in fluids*, 40(6):977–987, 2006.

[4] Yeon Sik Baik, Luis P Bernal, Kenneth Granlund, and Michael V Ol. Unsteady force generation and vortex dynamics of pitching and plunging aerofoils. *Journal of Fluid Mechanics*, 709:37–68, 2012.

[5] Albert Betz. Schraubenpropeller mit geringstem energieverlust. mit einem zusatz von l. prandtl. *Nachrichten von der Gesellschaft der Wissenschaften zu Göttingen, Mathematisch-Physikalische Klasse*, 1919:193–217, 1919.

[6] Shaoqing Chen, Bin Chen, and Brian D Fath. Assessing the cumulative environmental impact of hydropower construction on river systems based on energy network model. *Renewable and Sustainable Energy Reviews*, 42:78–92, 2015.

[7] Scott T Davids et al. *A computational and experimental investigation of a flutter generator*. PhD thesis, Monterey, California: Naval Postgraduate School, 1999.

[8] Jian Deng, CP Caulfield, and Xueming Shao. Effect of aspect ratio on the energy extraction efficiency of three-dimensional flapping foils. *Physics of Fluids (1994-present)*, 26(4):043102, 2014.

[9] Jian Deng, Lubao Teng, Dingyi Pan, and Xueming Shao. Inertial effects of the semi-passive flapping foil on its energy extraction efficiency. *Physics of Fluids*, 27(5):053103, 2015.

[10] G Dumas and T Kinsey. Eulerian simulations of oscillating airfoils in power extraction regime. *WIT Transactions on Engineering Sciences*, 52, 2006.

[11] Dominique Egré and Joseph C Milewski. The diversity of hydropower projects. *Energy Policy*, 30(14):1225–1230, 2002.

[12] Charles P Ellington, Coen Van Den Berg, Alexander P Willmott, and Adrian LR Thomas. Leading-edge vortices in insect flight. *Nature*, 384(6610):626, 1996.

[13] Yongxiu He, Yang Xu, Yuexia Pang, Huiying Tian, and Rui Wu. A regulatory policy to promote renewable energy consumption in china: Review and future evolutionary path. *Renewable Energy*, 89:695–705, 2016.

[14] Sam Heathcote and Ismet Gursul. Flexible flapping airfoil propulsion at low reynolds numbers. *AIAA journal*, 45(5):1066–1079, 2007.

[15] Sam Heathcote, Z Wang, and Ismet Gursul. Effect of spanwise flexibility on flapping wing propulsion. *Journal of Fluids and Structures*, 24(2):183–199, 2008.

[16] Charles M Hoke, John Young, and Joseph Lai. Time-varying flexible airfoil shape effects on flapping airfoil power extraction. In *32nd ASME Wind Energy Symposium*, page 1217, 2014.

[17] CM Hoke, J Young, and JCS Lai. Effects of time-varying camber deformation on flapping foil propulsion and power extraction. *Journal of Fluids and Structures*, 56:152–176, 2015.

[18] J.T. Houghton, Y. Ding, D.J. Griggs, M. Noguer, P.J. van der Linden, X. Dai, K. Maskell, and C.A. Johnson. Climate change 2001: the scientific basis. 2001.

[19] White House. United states mid-century strategy for deep decarbonization. 2016.

[20] GH Huxham, S Cochard, and J Patterson. Experimental parametric investigation of an oscillating hydrofoil tidal stream energy converter. In *18th Australasian Fluid Mechanics Conference (AFMC), Launceston, Australia, Dec*, pages 3–7, 2012.

[21] Kakkattukuzhy M Isaac, Anthony Colozza, and Jessica Rolwes. Force measurements on a flapping and pitching wing at low reynolds numbers. In *44th AIAA Aerospace Sciences Meeting*, pages 1–14, 2006.

[22] K Jones, M Platzer, K Jones, and M Platzer. Numerical computation of flapping-wing propulsion and power extraction. In *35th Aerospace Sciences Meeting and Exhibit*, page 826, 1997.

[23] Kevin D Jones, ST Davids, and Max F Platzer. Oscillating-wing power generation. In *3rd ASME/JSME joint fluids engineering conference, San Francisco, CA*, 1999.

[24] Kevin D Jones, K Lindsey, and MF Platzer. An investigation of the fluid-structure interaction in an oscillating-wing micro-hydropower generator. *WIT Transactions on The Built Environment*, 71, 2003.

[25] HR Karbasian, Javad Abolfazli Esfahani, and E Barati. The power extraction by flapping foil hydrokinetic turbine in swing arm mode. *Renewable Energy*, 88:130–142, 2016.

[26] T Kinsey and G Dumas. Optimal operating parameters for an oscillating foil turbine at reynolds number 500,000. *AIAA Journal*, 52(9):1885–1895, 2014.

[27] T Kinsey, G Dumas, G Lalande, J Ruel, A Mehut, P Viarouge, J Lemay, and Y Jean. Prototype testing of a hydrokinetic turbine based on oscillating hydrofoils. *Renewable Energy*, 36(6):1710–1718, 2011.

[28] Thomas Kinsey and Guy Dumas. Parametric study of an oscillating airfoil in a power-extraction regime. *AIAA journal*, 46(6):1318–1330, 2008.

[29] Thomas Kinsey and Guy Dumas. Testing and analysis of an oscillating hydrofoils turbine concept. In *ASME 2010 3rd Joint US-European Fluids Engineering Summer Meeting collocated with 8th International Conference on Nanochannels, Microchannels, and Minichannels*, pages 9–22. American Society of Mechanical Engineers, 2010.

[30] Thomas Kinsey and Guy Dumas. Computational fluid dynamics analysis of a hydrokinetic turbine based on oscillating hydrofoils. *Journal of fluids engineering*, 134(2):021104, 2012.

[31] Thomas Kinsey and Guy Dumas. Three-dimensional effects on an oscillating-foil hydrokinetic turbine. *Journal of fluids engineering*, 134(7):071105, 2012.

[32] Keon Lindsey. A feasibility study of oscillating-wing power generators. Technical report, DTIC Document, 2002.

[33] Wendi Liu, Qing Xiao, and Fai Cheng. A bio-inspired study on tidal energy extraction with flexible flapping wings. *Bioinspiration & biomimetics*, 8(3):036011, 2013.

[34] Wendi Liu, Qing Xiao, and Qiang Zhu. Passive flexibility effect on oscillating foil energy harvester. *AIAA Journal*, 54(1):1172–1187, 2016.

[35] William McKinney and James DeLaurier. Wingmill: an oscillating-wing windmill. *Journal of energy*, 5(2):109–115, 1981.

[36] Anthony J McMichael, Diarmid Campbell-Lendrum, Sari Kovats, Sally Edwards, Paul Wilkinson, Theresa Wilson, Robert Nicholls, Simon Hales, Frank Tanser, David Le Sueur, et al. Global climate change. 2004.

[37] Andrew M Mountcastle and Thomas L Daniel. Aerodynamic and functional consequences of wing compliance. *Experiments in fluids*, 46(5):873–882, 2009.

[38] United Nations / Framework Convention on Climate Change. Adoption of the paris agreement. 2016.

[39] Zhangli Peng and Qiang Zhu. Energy harvesting through flow-induced oscillations of a foil. *Physics of fluids*, 21(12):123602, 2009.

[40] P Prempraneerach, FS Hover, and MS Triantafyllou. The effect of chordwise flexibility on the thrust and efficiency of a flapping foil. *Proceedings Unmanned, Untethered Submersible Technology*, 2003.

[41] Magdi Ragheb and Adam M Ragheb. *Wind turbines theory-the betz equation and optimal rotor tip speed ratio*. INTECH Open Access Publisher, 2011.

[42] Kirill V Rozhdestvensky and Vladimir A Ryzhov. Aerohydrodynamics of flapping-wing propulsors. *Progress in aerospace sciences*, 39(8):585–633, 2003.

[43] R Saidur, NA Rahim, MR Islam, and KH Solangi. Environmental impact of wind energy. *Renewable and Sustainable Energy Reviews*, 15(5):2423–2430, 2011.

[44] Andrea Sciacchitano, Bernhard Wieneke, and Fulvio Scarano. Piv uncertainty quantification by image matching. *Measurement Science and Technology*, 24(4):045302, 2013.

[45] Eriko Shimizu, Koji Isogai, and Shigeru Obayashi. Multiobjective design study of a flapping wing power generator. *Journal of Fluids Engineering*, 130(2):021104, 2008.

[46] Kourosh Shoele and Qiang Zhu. Numerical simulation of a pectoral fin during labriform swimming. *Journal of Experimental Biology*, 213(12):2038–2047, 2010.

[47] Kourosh Shoele and Qiang Zhu. Leading edge strengthening and the propulsion performance of flexible ray fins. *Journal of Fluid Mechanics*, 693:402–432, 2012.

[48] Wei Shyy, Hikaru Aono, Satish Kumar Chimakurthi, P Trizila, C-K Kang, Carlos ES Cesnik, and Hao Liu. Recent progress in flapping wing aerodynamics and aeroelasticity. *Progress in Aerospace Sciences*, 46(7):284–327, 2010.

[49] Wei Shyy and Hao Liu. Flapping wings and aerodynamic lift: the role of leading-edge vortices. *AIAA journal*, 45(12):2817–2819, 2007.

[50] Firas Siala, Alexander D Totpal, and James Liburdy. Wake dynamics and structure of a heaving flexible foil based on piv measurements. In *54th AIAA Aerospace Sciences Meeting*, page 0830, 2016.

[51] Firas F Siala, Alexander D Totpal, and James A Liburdy. Characterization of vortex dynamics in the near wake of an oscillating flexible foil. *Journal of Fluids Engineering*, 138(10):101202, 2016.

[52] Bradley J Simpson, Franz S Hover, Michael S Triantafyllou, et al. Experiments in direct energy extraction through flapping foils. In *The Eighteenth International Offshore and Polar Engineering Conference*. International Society of Offshore and Polar Engineers, 2008.

[53] Thomas F. Stocker, Dahe Qin, Gian-Kasper Plattner, Melinda M.B. Tignor, Simon K. Allen, Judith Boschung, Alexander Nauels, Yu Xia, Vincent Bex, Pauline M. Midgley, et al. Climate change 2013: the physical science basis. 2013.

[54] Lubao Teng, Jian Deng, Dingyi Pan, and Xueming Shao. Effects of non-sinusoidal pitching motion on energy extraction performance of a semi-active flapping foil. *Renewable Energy*, 85:810–818, 2016.

[55] Fang-Bao Tian, John Young, and Joseph CS Lai. Improving power-extraction efficiency of a flapping plate: from passive deformation to active control. *Journal of Fluids and Structures*, 51:384–392, 2014.

[56] Gabriel E Torres and Thomas J Mueller. Low aspect ratio aerodynamics at low reynolds numbers. *AIAA journal*, 42(5):865–873, 2004.

[57] CO Usoh, J Young, JCS Lai, and MA Ashraf. Numerical analysis of a non-profiled plate for flapping wing turbines. In *Proceedings of the 18th Australasian Fluid Mechanics Conference, Launceston, Australia*, 2012.

[58] Bernhard Wieneke. Piv uncertainty quantification from correlation statistics. *Measurement Science and Technology*, 26(7):074002, 2015.

[59] TYT Wu. Extraction of flow energy by a wing oscillating in waves. Technical report, 1971.

[60] Qing Xiao, Wei Liao, Shuchi Yang, and Yan Peng. How motion trajectory affects energy extraction performance of a biomimic energy generator with an oscillating foil? *Renewable Energy*, 37(1):61–75, 2012.

[61] Qing Xiao and Qiang Zhu. A review on flow energy harvesters based on flapping foils. *Journal of fluids and structures*, 46:174–191, 2014.

[62] Yonghui Xie, Kun Lu, and Di Zhang. Investigation on energy extraction performance of an oscillating foil with modified flapping motion. *Renewable Energy*, 63:550–557, 2014.

[63] Bo Yin and Haoxiang Luo. Effect of wing inertia on hovering performance of flexible flapping wings. *Physics of Fluids*, 22(11):111902, 2010.

[64] John Young, Muhammad A Ashraf, Joseph CS Lai, and Max F Platzer. Numerical simulation of fully passive flapping foil power generation. *AIAA journal*, 51(11):2727–2739, 2013.

[65] John Young, Joseph CS Lai, and Max F Platzer. A review of progress and challenges in flapping foil power generation. *Progress in Aerospace Sciences*, 67:2–28, 2014.

[66] Meilin Yu and Zhi J Wang. Numerical simulation of oscillating-wing based energy harvest mechanism using the high-order spectral difference method. In *Proceeding of the 31st AIAA applied aerodynamics conference, American Institute of Aeronautics and Astronautics, Reston, Virginia*, volume 2670, 2013.

[67] Jiapu Zhan, Bing Xu, Jie Wu, and Jing Wu. Power extraction performance of a semi-activated flapping foil in gusty flow. *Journal of Bionic Engineering*, 14(1):99–110, 2017.

[68] Qiang Zhu. Numerical simulation of a flapping foil with chordwise or spanwise flexibility. *AIAA journal*, 45(10):2448–2457, 2007.

[69] Qiang Zhu. Optimal frequency for flow energy harvesting of a flapping foil. *Journal of fluid mechanics*, 675:495–517, 2011.

[70] Qiang Zhu. Energy harvesting by a purely passive flapping foil from shear flows. *Journal of Fluids and Structures*, 34:157–169, 2012.

[71] Qiang Zhu, Max Haase, and Chin H Wu. Modeling the capacity of a novel flow-energy harvester. *Applied Mathematical Modelling*, 33(5):2207–2217, 2009.

[72] Qiang Zhu and Zhangli Peng. Mode coupling and flow energy harvesting by a flapping foil. *Physics of Fluids*, 21(3):033601, 2009.

[73] Qiang Zhu and Kourosh Shoele. Propulsion performance of a skeleton-strengthened fin. *Journal of Experimental Biology*, 211(13):2087–2100, 2008.

APPENDICES

Appendix A: Wind Tunnel Flow Calibration - Particle Image Velocimetry

Particle image velocimetry (PIV) was used to calibrate the wind tunnel velocity. A dual head ND:YLF 527 nm pulsed laser (New Wave research, Pegasus PIV) was used in conjunction with a Dantec optical module (Dantec Dynamics 9080 $\times$ 0651) to generate a roughly 1 mm thick light sheet. An Integrated Design Tools CMOS high-speed camera (iNanoSense MotionPro X-3) equipped with an internal intensifier was used to capture image pairs at a frame resolution of 1280 $\times$ 1024 pixels. A 60 mm adjustable focusing lens (Nikon AF Micro-NIKKOR f/2.8D) was used with a 532 nm bandpass light filter to achieve high resolution filtered images. The resulting field of view was approximately 208 $\times$ 166.4 mm. An in-house designed and manufactured Laskin nozzle atomizer was used for seeding particle generation using pressurized air and vegetable oil, and produces particles sized in the 2 to 6 μm range (verified using autocorrelation peak width distribution).

Image collection and post processing was performed in Dantec DynamicStudio v4.3. A multi-grid, multi-pass adaptive correlation scheme was used with a local vector neighborhood validation to filter spurious vectors. The adaptive correlation window sizes contain three refinement steps, with an initial and final interrogation window size of 256 $\times$ 256 and 32 $\times$ 32 pixels, respectively, with a 75% overlap. In addition, a central difference interrogation window offset was used with a high accuracy sub-pixel fitting algorithm. The resulting vector field is 79×63 vectors, with a vector spacing of 2.6 mm.

The time between pulses varied from 122 to 975 μs for the range of flow speeds tested, resulting in 6.5 to 7-pixel displacement. The range of wind tunnel free-stream speeds tested ranged from 1 to 8 meters per second as indicated on the wind tunnel readout, in 0.5 meter per second increments. For each flow speed, 100 image pairs were collected, which is sufficient for a simple uniform flow such as this. The resulting 100 vector fields were then averaged both temporally as well as spatially, resulting in a single representative mean flow value. The resulting calibration curve of the wind tunnel readout and the PIV measured velocity is shown in Fig. A.1. The uncertainty in the

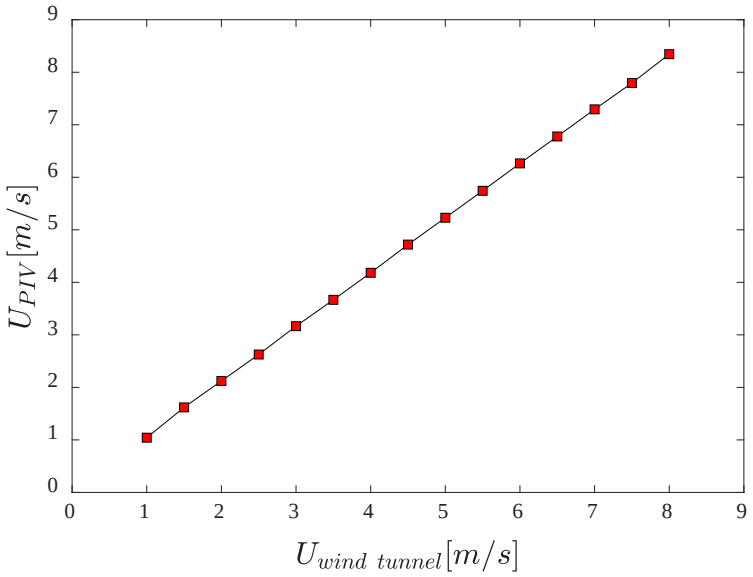

Figure A.1: Calibration plot showing the wind tunnel set point flow speed and resulting measured PIV flow speed.

longitudinal direction is calculated to be 1.32% in a similar study conducted by Siala et. al. [51].

Note that this PIV system is not the same system used to measure the flow field results presented in Sections 3.3 and 3.4 of this paper. During data collection, the camera used to calibrate the free-stream flow malfunctioned, and thus PIV systems were swapped. The flow field results in this text were measured using the PIV system outlined in Section 2.4.

Appendix B: Additional Foil Information

An exploded view of the foil components for the rigid and flexible foil configurations are shown in Fig. B.1 (a) and (b), respectively. In the rigid configuration, a rod is placed perpendicular to the to the axis of rotation of the hinge mechanism, thus inhibiting any rotation in the hinge. For the flexible LE configuration, a torsion rod is inserted into the foil hinge as previously discussed in Section 2.1.2. Additionally, the mass of each foil component are shown in Table B.1 and B.2 for the rigid and flexible LE configurations, respectively.

Table B.1: Rigid configuration foil masses.

Component	Quantity	Mass Each [g]	Mass Total [g]
LE/TE	2	3.81	7.62
Body	1	38	38
Ti Rod	1	97.5	97.5
Steel Inserts	3	2.8	8.4
Steel Rod (long)	1	3.1	3.1
Steel Rod (short)	2	2	4
Total:			227.2

Table B.2: Flexible LE configuration foil masses.

Component	Quantity	Mass Each [g]	Mass Total [g]
LE/TE	2	3.81	7.62
Body	1	38	38
Ti Rod	1	97.5	97.5
Steel Inserts	3	2.8	8.4
Steel Rod (long)	0	3.1	0
Steel Rod (short)	2	2	4
Total:			224.1

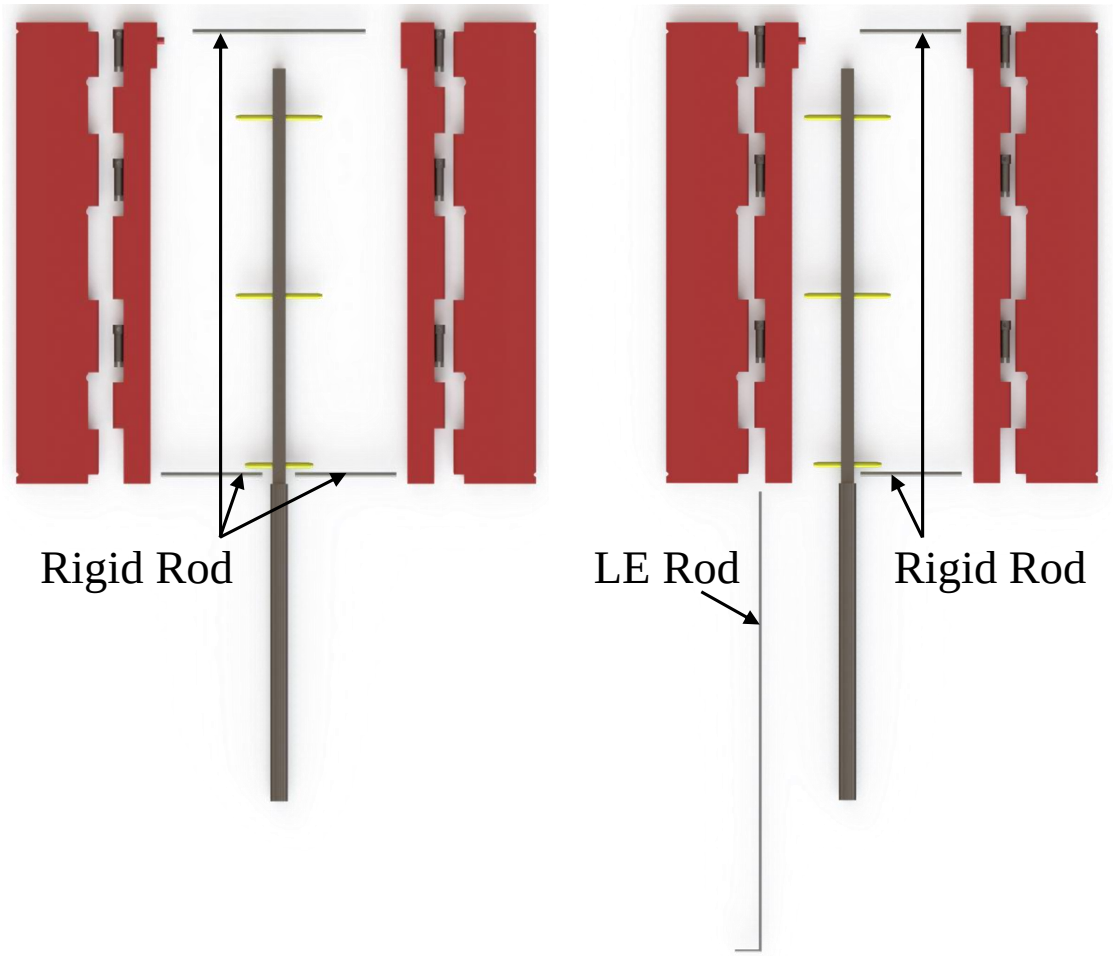

Figure B.1: The exploded view of the foil showcasing: (a) the rigid configuration, and (b) the flexible LE configuration. Note the "LE Rod", which is the torsion spring used to generate passive flexibility, and the "Rigid Rod" which inhibits rotation about the foil hinge.

Appendix C: LabVIEW Interface

All motion control and force measurement data acquisition were performed using a LabVIEW VI file created by Ali Mousavian, Ph.D. candidate of Oregon State University's Physics department. The script/program is capable of controlling the phase delay between pitching and heaving motions, recording and visualizing in-situ lift and drag forces from the load cells, and synchronizing laser pulses for phase-locked PIV measurements. The program works by sending a series of pulses to the stepper motor controllers. Because the pitching and heaving motions must operate at the same oscillation frequency, the step signals are sent to both the pitching and heaving motors at the same time. This results in a synchronization of the pitching and heaving motions. In order to obtain the desired phase relationship between the two motions, the following procedure was performed:

1. Align the heaving motor at the mid-heave position.
2. Align the pitching motor at the 0° angle of attack position.
3. Prescribe the desired phase relationship between the two motions as an input.
4. Upon running the program, the VI file steps the pitching motor ahead by the desired phase shift. Once the phase shift is satisfied, the step signals are sent to both the pitching and heaving motor simultaneously until the program is halted.

Due to the system-level prioritization of processes on the computer CPU, the timing between the stepping signals may occasionally differ resulting in the de-synchronization of pitching and heaving motions. This de-synchronization is then tabulated as an error and is displayed in the LabVIEW GUI. When this error displays a value other than 0 or ± 0.18 (corresponding to one signal impulse for the stepper motors), the system must be stopped and re-set. It took approximately 4 to 5 attempts to get the correct phase timing. Future efforts will address this issue for improved device control.

Appendix D: Tracker and ImageJ

A sample snapshot of the Tracker software can be seen in Fig. D.1. The points were tracked using the auto-tracker feature, where points are automatically tracked by the program based on a template frame. The template frame (region enclosed in the dotted-line circle) is a user-defined region selected from any image frame in the motion video. The software then searches through search windows (region enclosed in the dotted-line rectangle) which are centered about the tracked point from the previous frame for a best match against the template frame. The best match is based on a match score, determined from the inverse of the sum of squares of the differences in pixel values between the template frame and the current frame. The template frame evolution rate, a percentage-based weighting of the current match frame and the previous match frame, was set to 0% in order to avoid template drift over time. A sub-pixel algorithm was used to spatially locate the tracked points based on match scores of neighboring points. A match score of 1 (out of 10) was used as the matching criteria. This was necessary as the pixel intensities of the fiducial marks varied due to spatial variations of lighting intensity across the frames (top and bottom heaving positions had lower pixel intensity values than the mid heave region), resulting in a loss of correlation. However, most points had match scores well above 10. Additionally, the points were manually inspected to ensure sporadic matches were not obtained. Roughly 5-10 points for every 1000 frames were found to be sporadically matched, and were manually shifted to the center of the fiducial points to the author's best ability.

Motion videos were also processed in ImageJ (developed by the National Institute of Health) in order to increase lighting uniformity and detectability of the auto-tracked marks. In this software, the contrast and intensity of the pixels in select regions of the videos were tuned until the fiducial marks were clearly contrasted from any background lighting. During this process, care was taken to ensure the distribution of pixel intensity near these marks did not falsely shift the location of the fiducial marks.

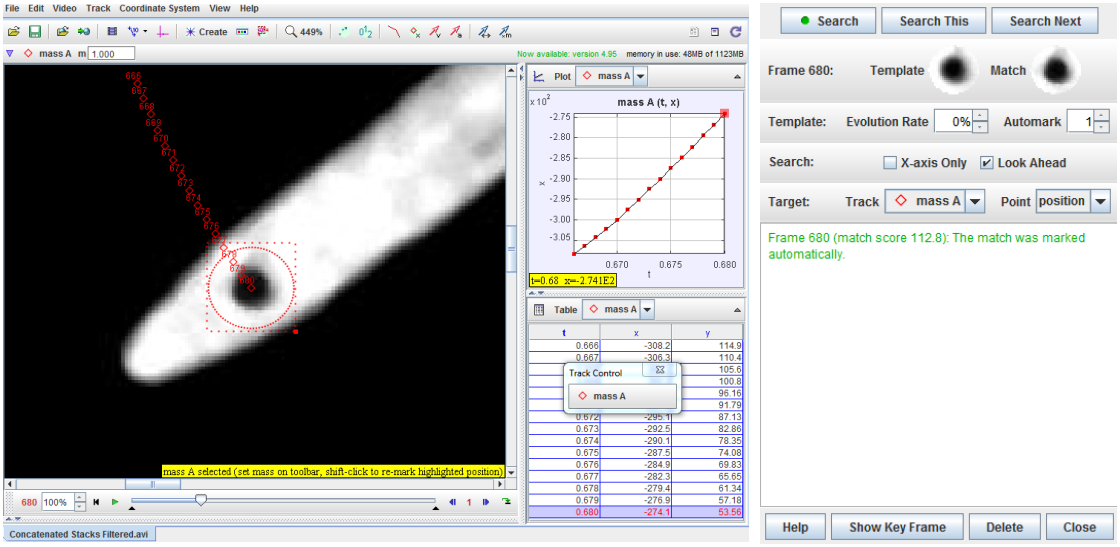

(a) (b)

Figure D.1: Tracker snapshots showing the (a) Tracker interface as well as (b) the auto-tracking function. Note that the template frame seen in (b) is the same as the circular-dotted line in (a). This template frame is used to locate the best match within the search region (dotted-line box) in each subsequent frames.

Appendix E: Foil Motion

This chapter of the appendix shows all motion tracking results of the foil. Figures E.1, E.2, and E.3, show the effective angles of attack of the foil for the $\kappa = \infty$, 0.13 $N-m/rad$, and 0.07 $N-m/rad$ LE configurations, respectively. These Figs. show the α_{eff} for all Φ and θ_0, when $k = 0.042$. Figures E.4 and E.5 show the deflection angle of the LE relative to the foil body for the $\kappa = 0.13\ N-m/rad$ and $0.07\ N-m/rad$ LE configurations, respectively. Also, these Figs. show the deflection angles for all Φ and θ_0 tested for the $k = 0.042$ case.

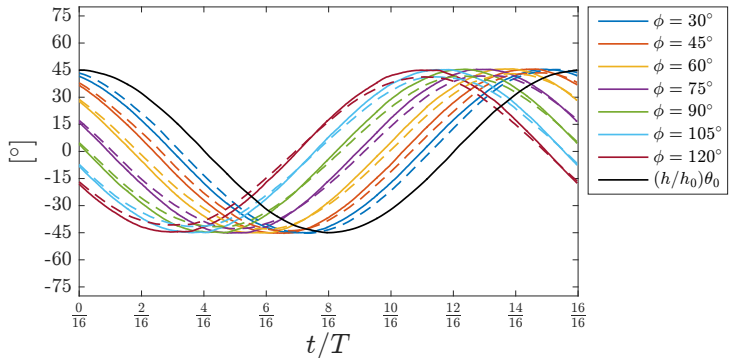

(a)

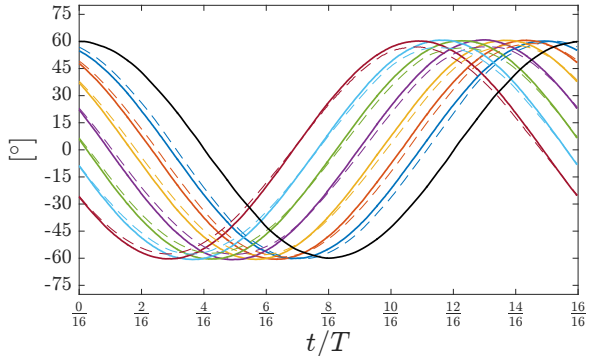

(b)

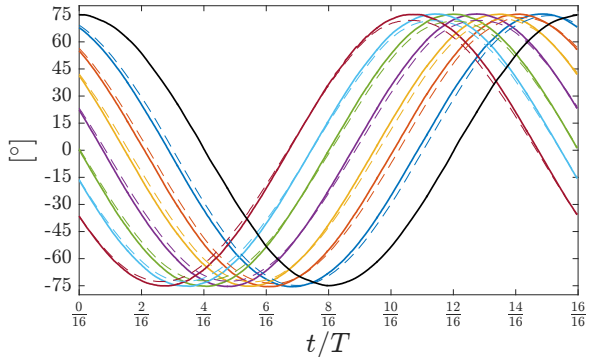

(c)

Figure E.1: The instantaneous pitching angle θ (solid lines) and the effective angle of attack α_{eff} (dashed lines) over a cycle for the rigid foil configuration. The instantaneous position of the foil is also shown for reference, where the position is non-dimensionalized with the heaving amplitude and multiplied by the pitching amplitude in order to see it on this scale. Figures (a), (b), and (c) correspond to $\theta_0 = 45°$, $\theta_0 = 60°$, and $\theta_0 = 75°$, respectively.

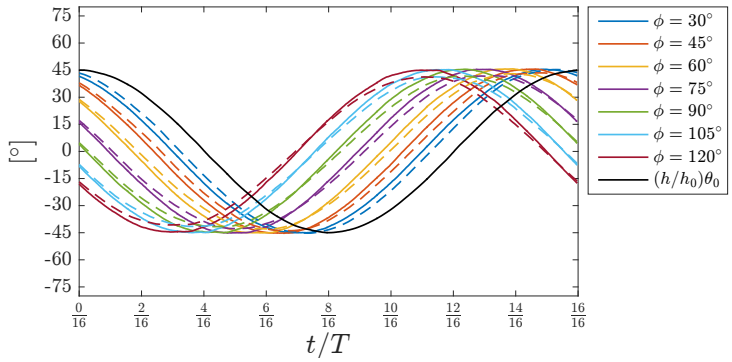

(a)

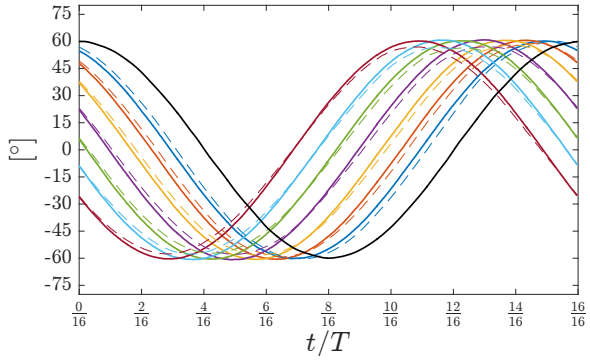

(b)

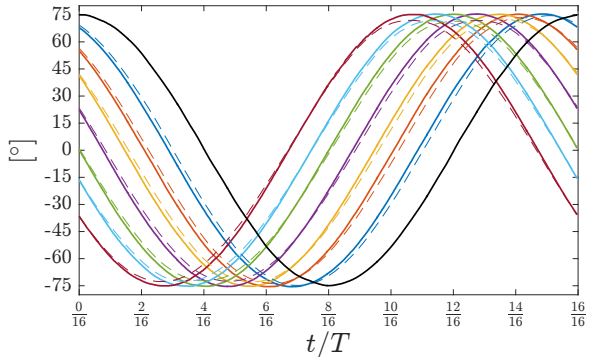

(c)

Figure E.2: The instantaneous pitching angle θ (solid lines) and the effective angle of attack α_{eff} (dashed lines) over a cycle for the $\kappa = 0.13\ N - m/rad$ flexible LE configuration. The instantaneous position of the foil is also shown for reference, where the position is non-dimensionalized with the heaving amplitude and multiplied by the pitching amplitude in order to see it on this scale. Figures (a), (b), and (c) correspond to $\theta_0 = 45°$, $\theta_0 = 60°$, and $\theta_0 = 75°$, respectively.

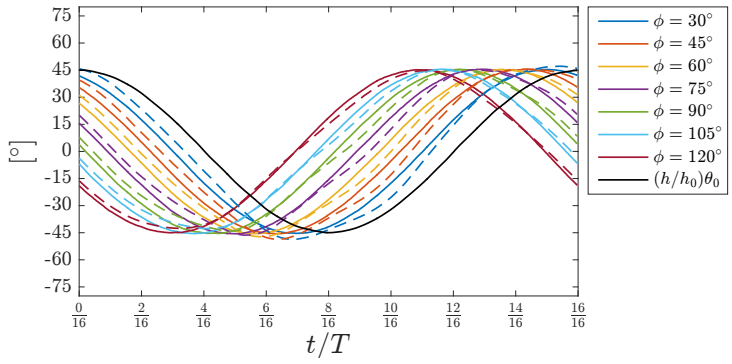

(a)

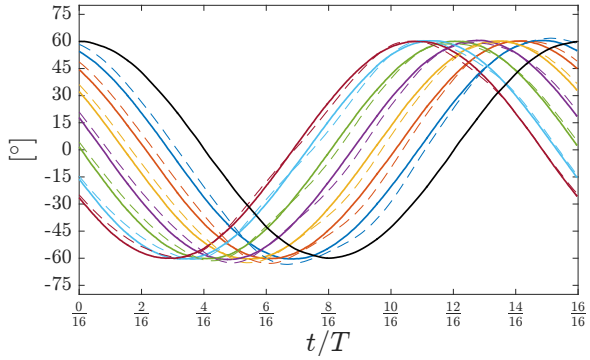

(b)

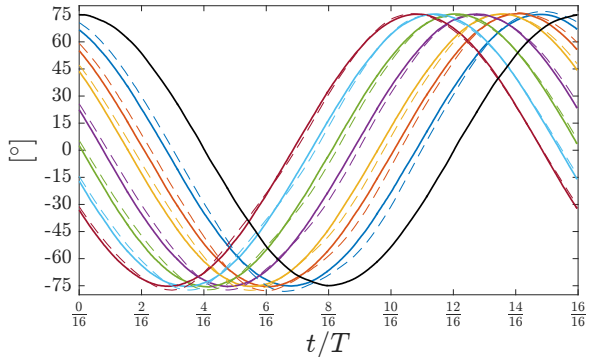

(c)

Figure E.3: The instantaneous pitching angle θ (solid lines) and the effective angle of attack α_{eff} (dashed lines) over a cycle for the $\kappa = 0.07\ N - m/rad$ flexible LE configuration. The instantaneous position of the foil is also shown for reference, where the position is non-dimensionalized with the heaving amplitude and multiplied by the pitching amplitude in order to see it on this scale. Figures (a), (b), and (c) correspond to $\theta_0 = 45°$, $\theta_0 = 60°$, and $\theta_0 = 75°$, respectively.

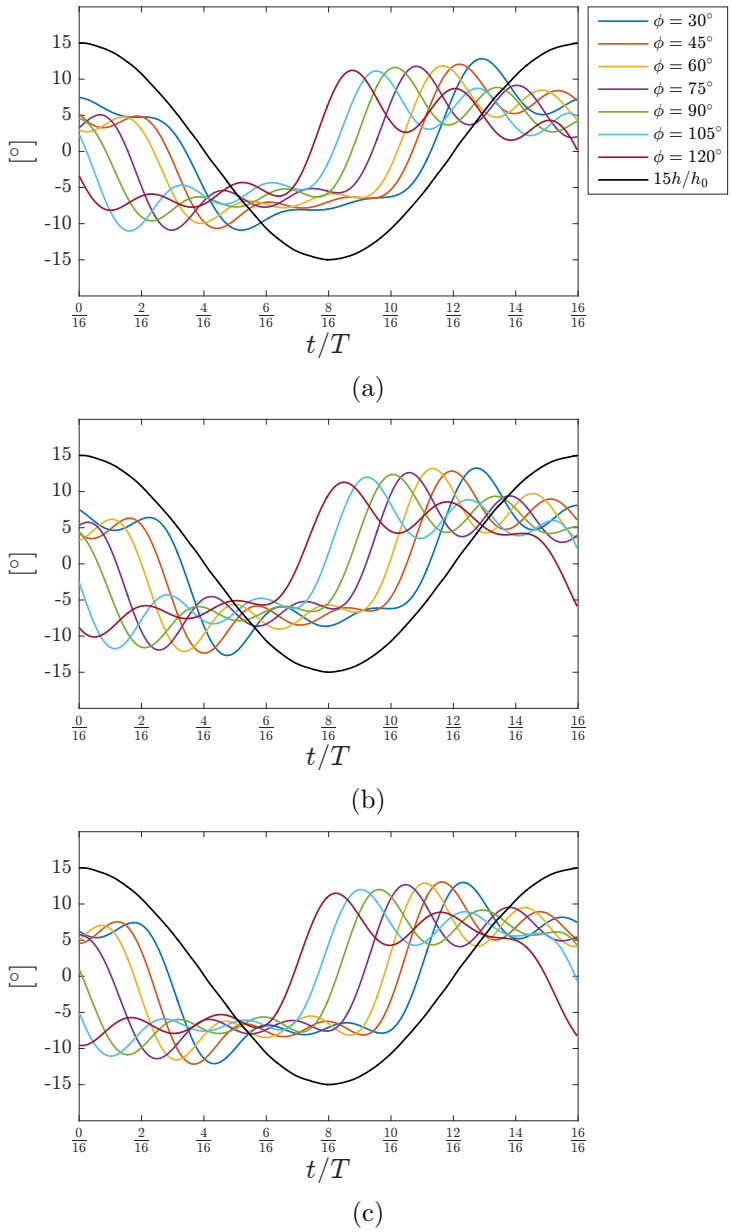

Figure E.4: The instantaneous LE angle relative to the foil body θ_{LE} over a cycle for the $\kappa = 0.13\ N-m/rad$ LE configuration, with θ_0 equal to (a) 45°, (b) 60°, and (c) 75°. The instantaneous position of the foil is also shown for reference, where the position is non-dimensionalized with the heaving amplitude and multiplied by a constant in order to amplify it on this scale.

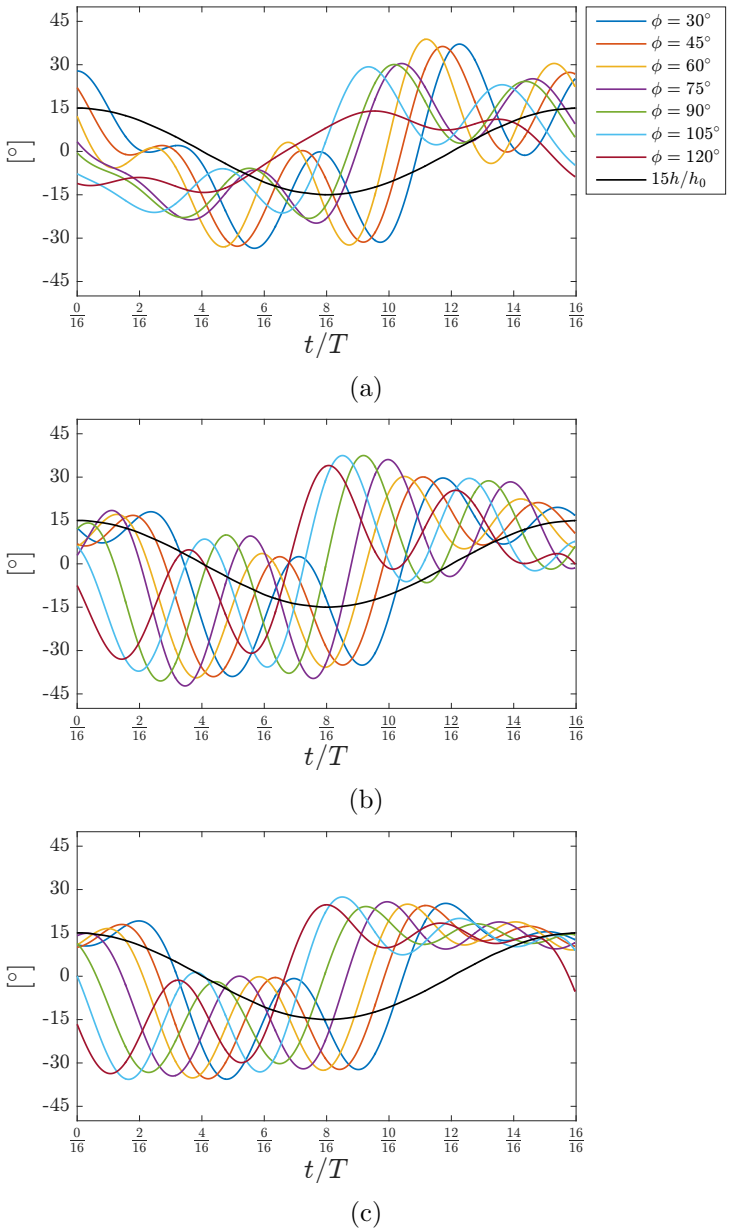

(a)

(b)

(c)

Figure E.5: The instantaneous LE angle relative to the foil body θ_{LE} over a cycle for the $\kappa = 0.07\ N-m/rad$ LE configuration, with θ_0 equal to (a) 45°, (b) 60°, and (c) 75°. The instantaneous position of the foil is also shown for reference, where the position is non-dimensionalized with the heaving amplitude and multiplied by a constant in order to amplify it on this scale.

Appendix F: Rigid Foil Force Measurements

This chapter contains all C_L curves for the rigid foil configuration after the processing techniques of Sections 2.2.4 and 2.2.5 have been applied. The results are organized according to Table F.1.

Table F.1: Table of C_L results for all force measurement runs.

Figure	θ_0 [°]	Φ [°]	k	κ $[N-m/rad]$
F.1	45	30 : 15 : 120	0.083	∞
F.2	60	30 : 15 : 120	0.083	∞
F.3	75	30 : 15 : 120	0.083	∞
F.4	45	30 : 15 : 120	0.063	∞
F.5	60	30 : 15 : 120	0.063	∞
F.6	75	30 : 15 : 120	0.063	∞
F.7	45	30 : 15 : 120	0.042	∞
F.8	60	30 : 15 : 120	0.042	∞
F.9	75	30 : 15 : 120	0.042	∞

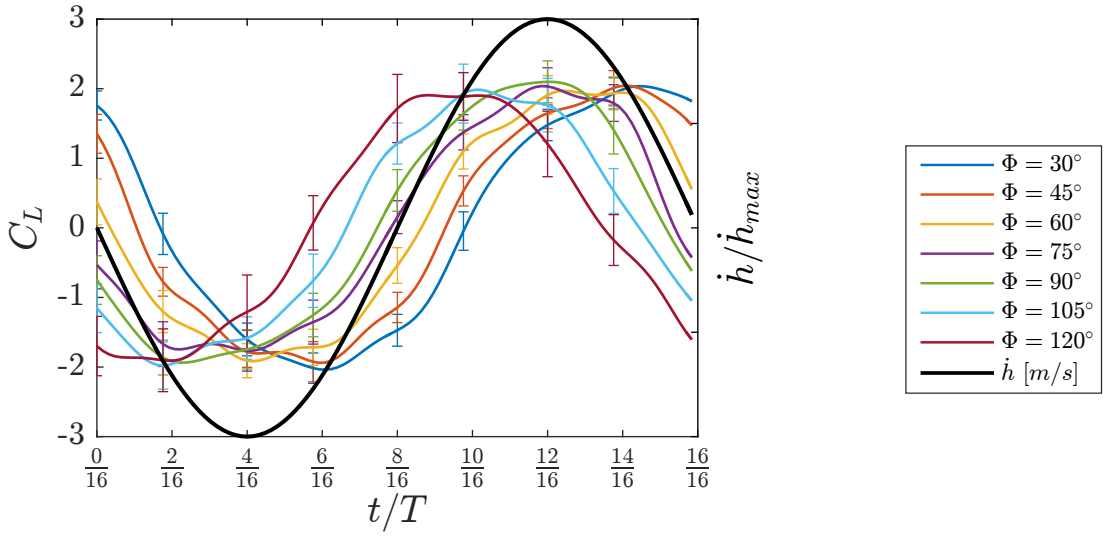

Figure F.1: Lift coefficient for all Φ tested $(30 : 15 : 105°)$, $\theta = 45°$, $k = 0.083$, $\kappa = \infty$.

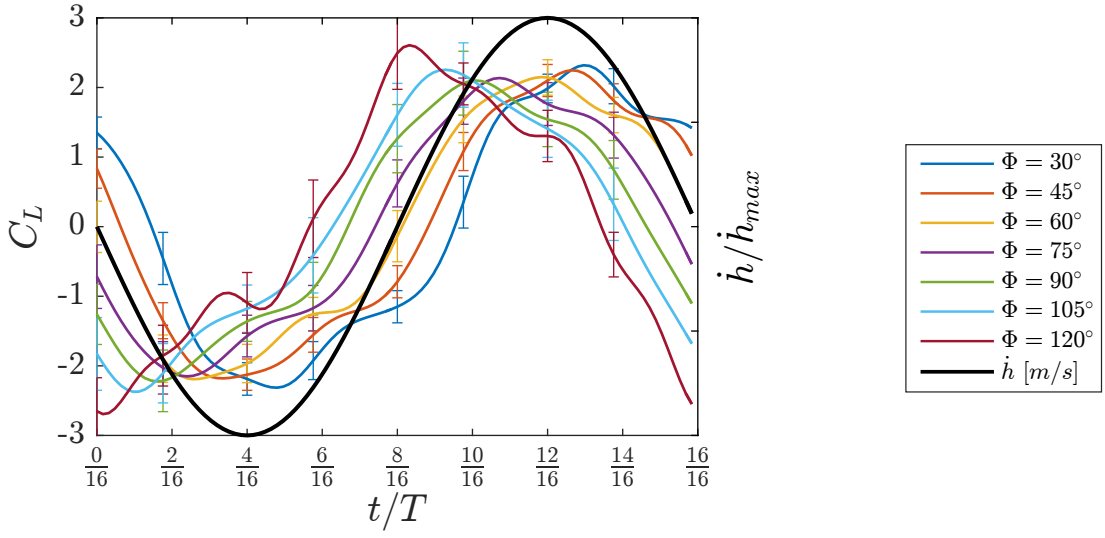

Figure F.2: Lift coefficient for all Φ tested $(30 : 15 : 105°)$, $\theta = 60°$, $k = 0.083$, $\kappa = \infty$.

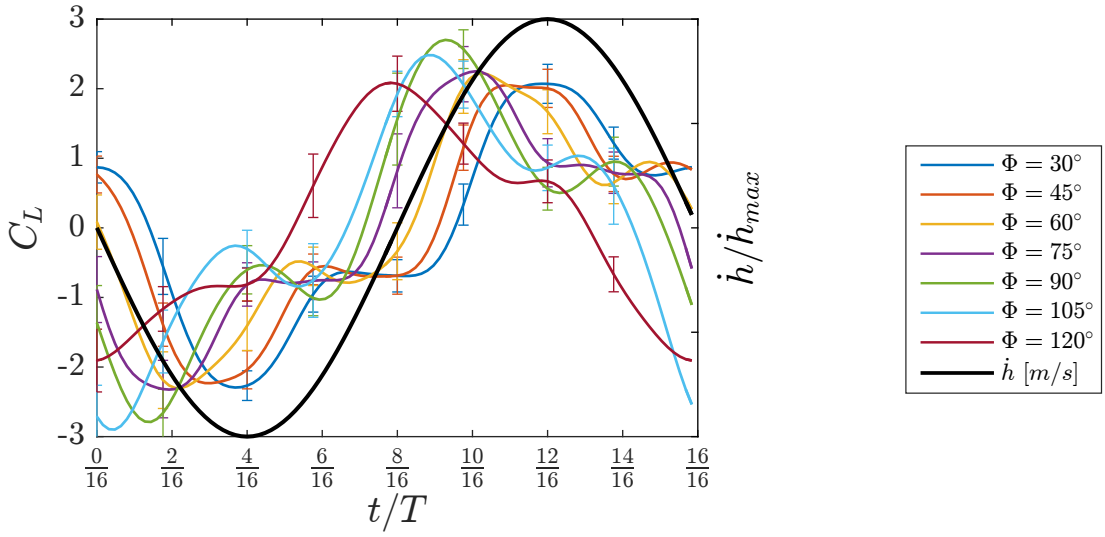

Figure F.3: Lift coefficient for all Φ tested $(30 : 15 : 105°)$, $\theta = 75°$, $k = 0.083$, $\kappa = \infty$.

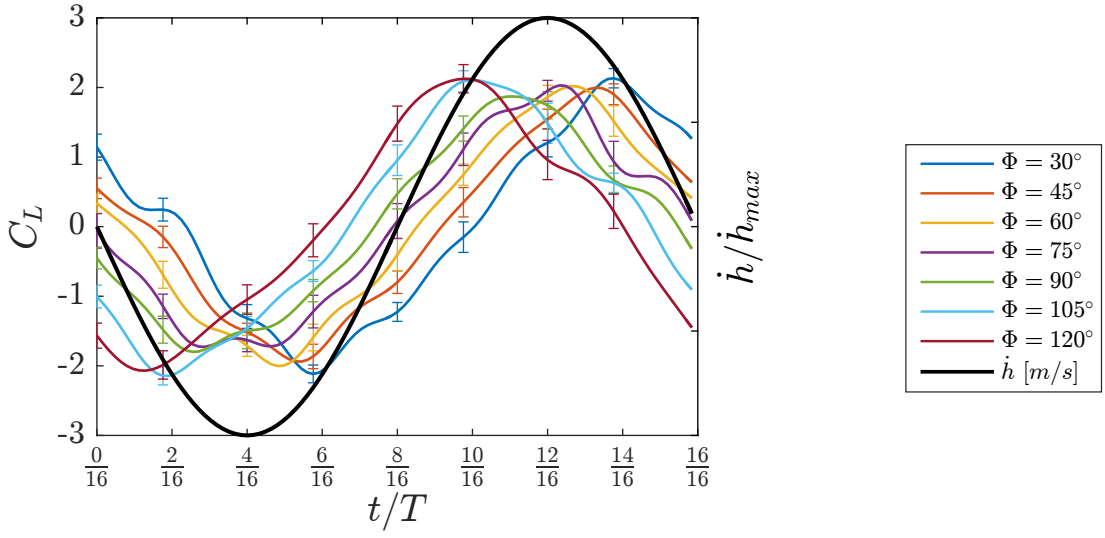

Figure F.4: Lift coefficient for all Φ tested $(30 : 15 : 105°)$, $\theta = 45°$, $k = 0.063$, $\kappa = \infty$.

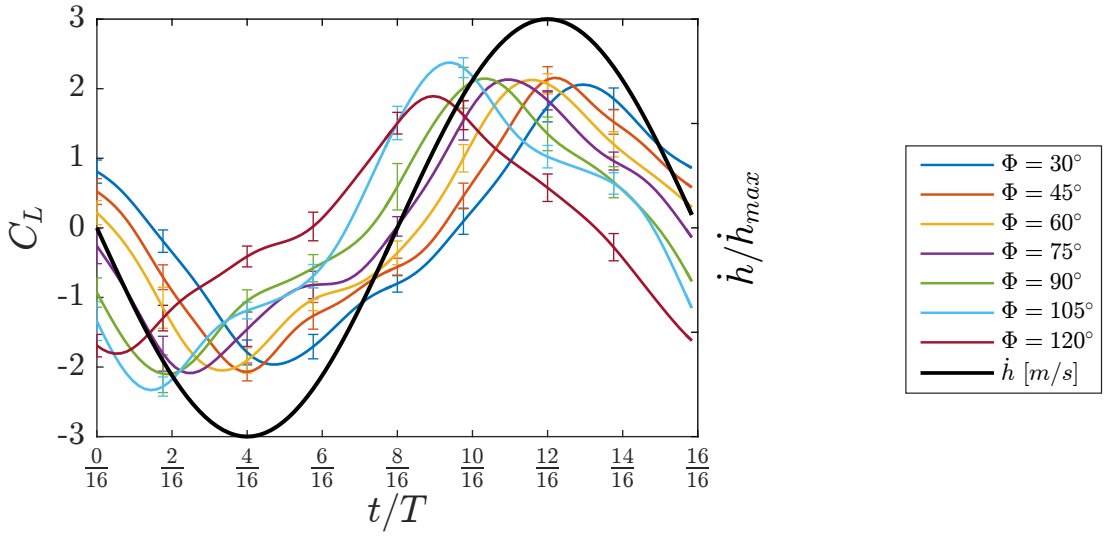

Figure F.5: Lift coefficient for all Φ tested $(30 : 15 : 105°)$, $\theta = 60°$, $k = 0.063$, $\kappa = \infty$.

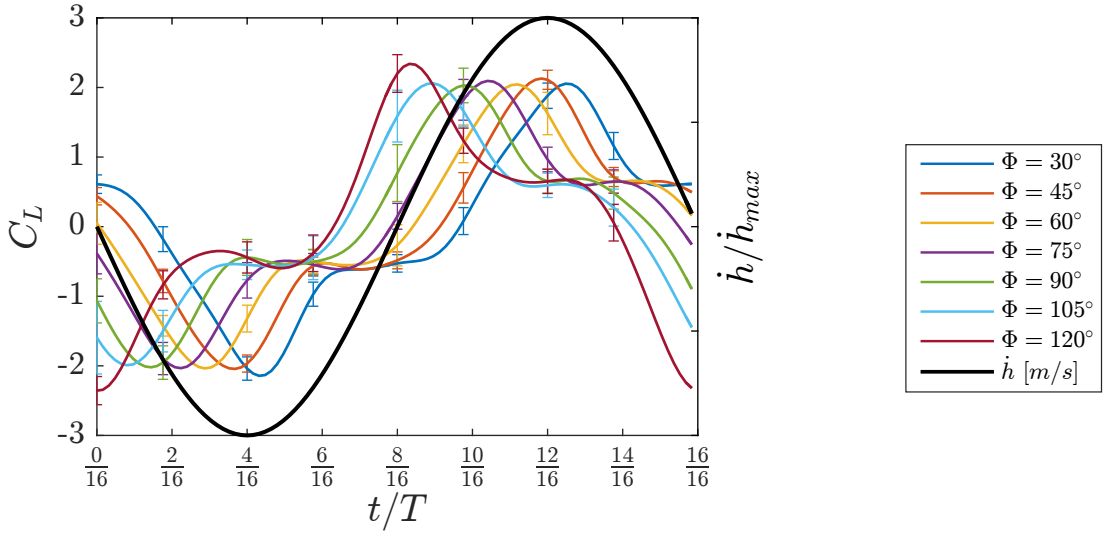

Figure F.6: Lift coefficient for all Φ tested $(30 : 15 : 105°)$, $\theta = 75°$, $k = 0.063$, $\kappa = \infty$.

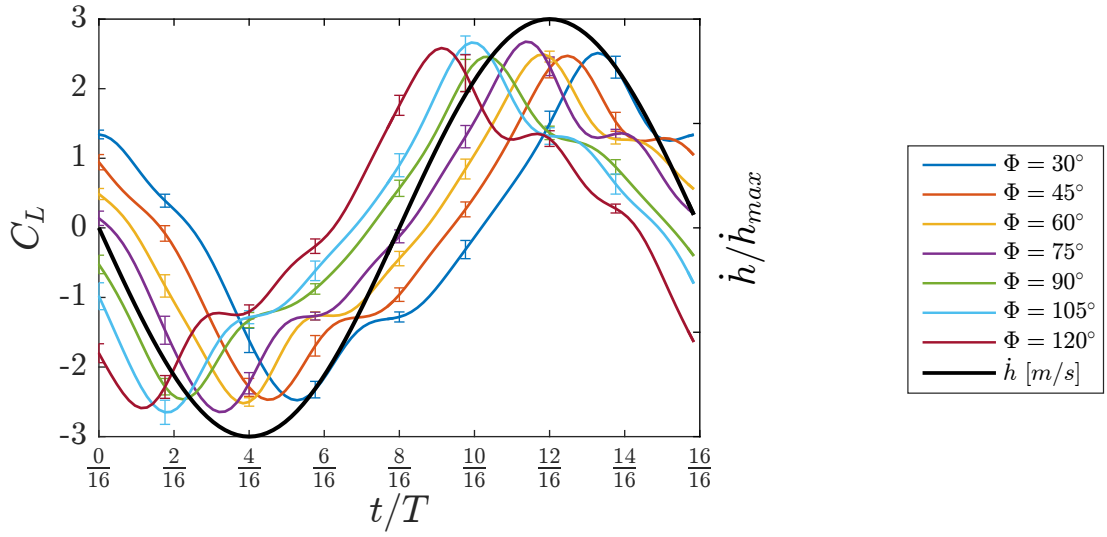

Figure F.7: Lift coefficient for all Φ tested $(30 : 15 : 105°)$, $\theta = 45°$, $k = 0.042$, $\kappa = \infty$.

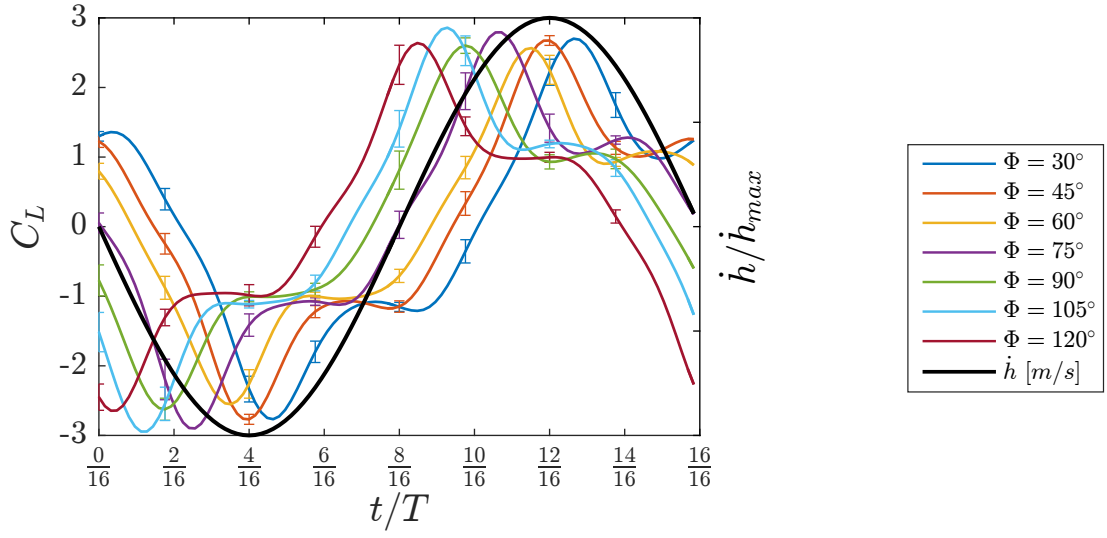

Figure F.8: Lift coefficient for all Φ tested $(30 : 15 : 105°)$, $\theta = 60°$, $k = 0.042$, $\kappa = \infty$.

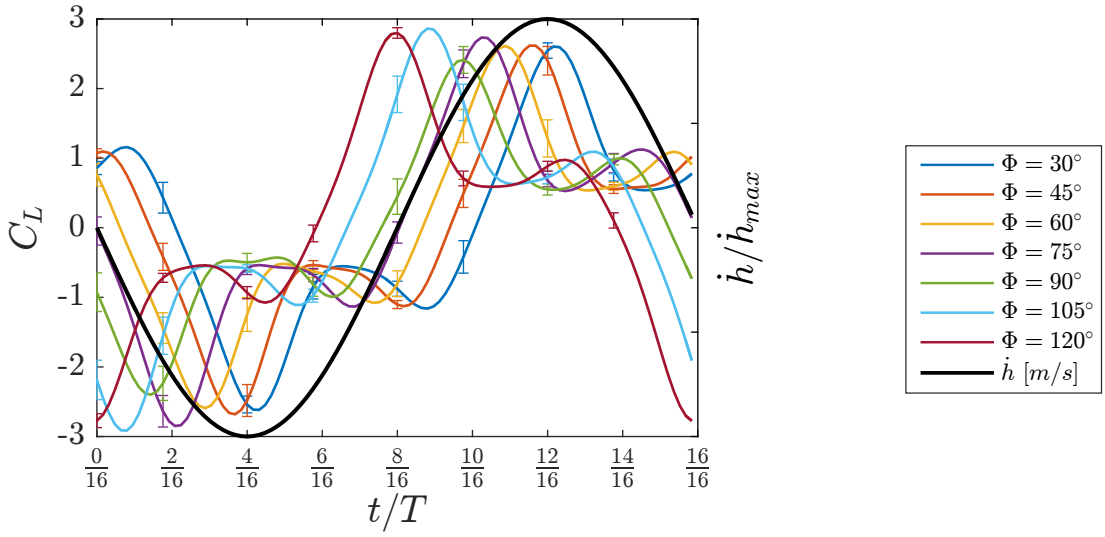

Figure F.9: Lift coefficient for all Φ tested $(30 : 15 : 105°)$, $\theta = 75°$, $k = 0.042$, $\kappa = \infty$.

Appendix G: Rigid Foil PIV Measurements

This chapter contains all PIV measurements for the rigid foil configuration after the processing techniques of Section 2.4 has been applied. The results are organized according to Table G.1.

Table G.1: Table of PIV results for all rigid foil runs.

Figure	θ_0 [°]	Φ [°]	k	κ $[N-m/rad]$
G.1	75	90	0.083	∞
G.2	60	45	0.083	∞
G.3	60	60	0.083	∞
G.4	60	75	0.083	∞
G.5	60	90	0.083	∞
G.6	45	75	0.083	∞
G.7	45	90	0.083	∞
G.8	45	105	0.083	∞
G.9	60	60	0.063	∞
G.10	45	90	0.063	∞
G.11	60	60	0.042	∞
G.12	45	90	0.042	∞

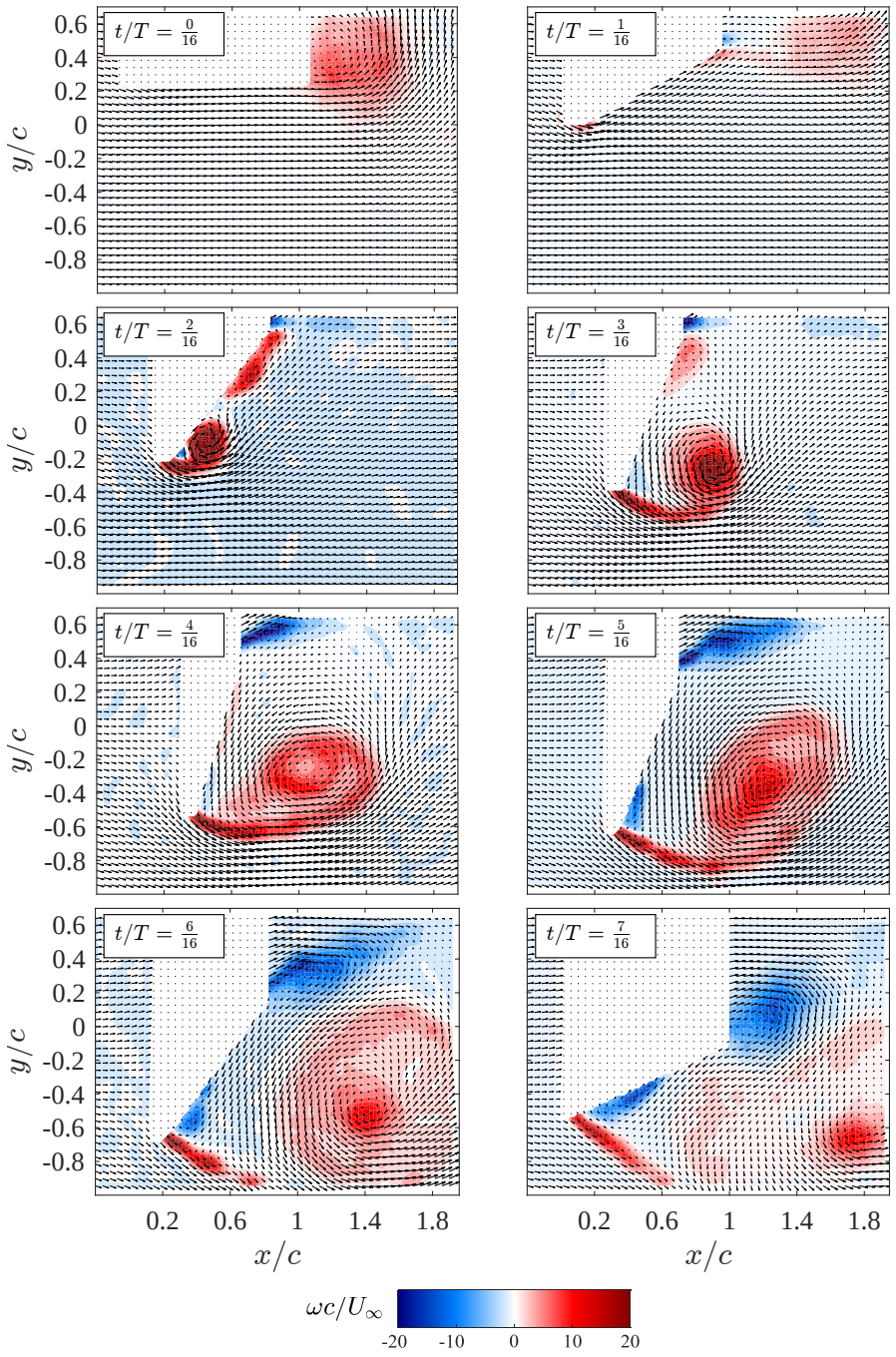

Figure G.1: Vorticity distribution overlaid with velocity vectors around the rigid foil with $k = 0.083$, $\theta_0 = 75°$, and $\Phi = 90°$.

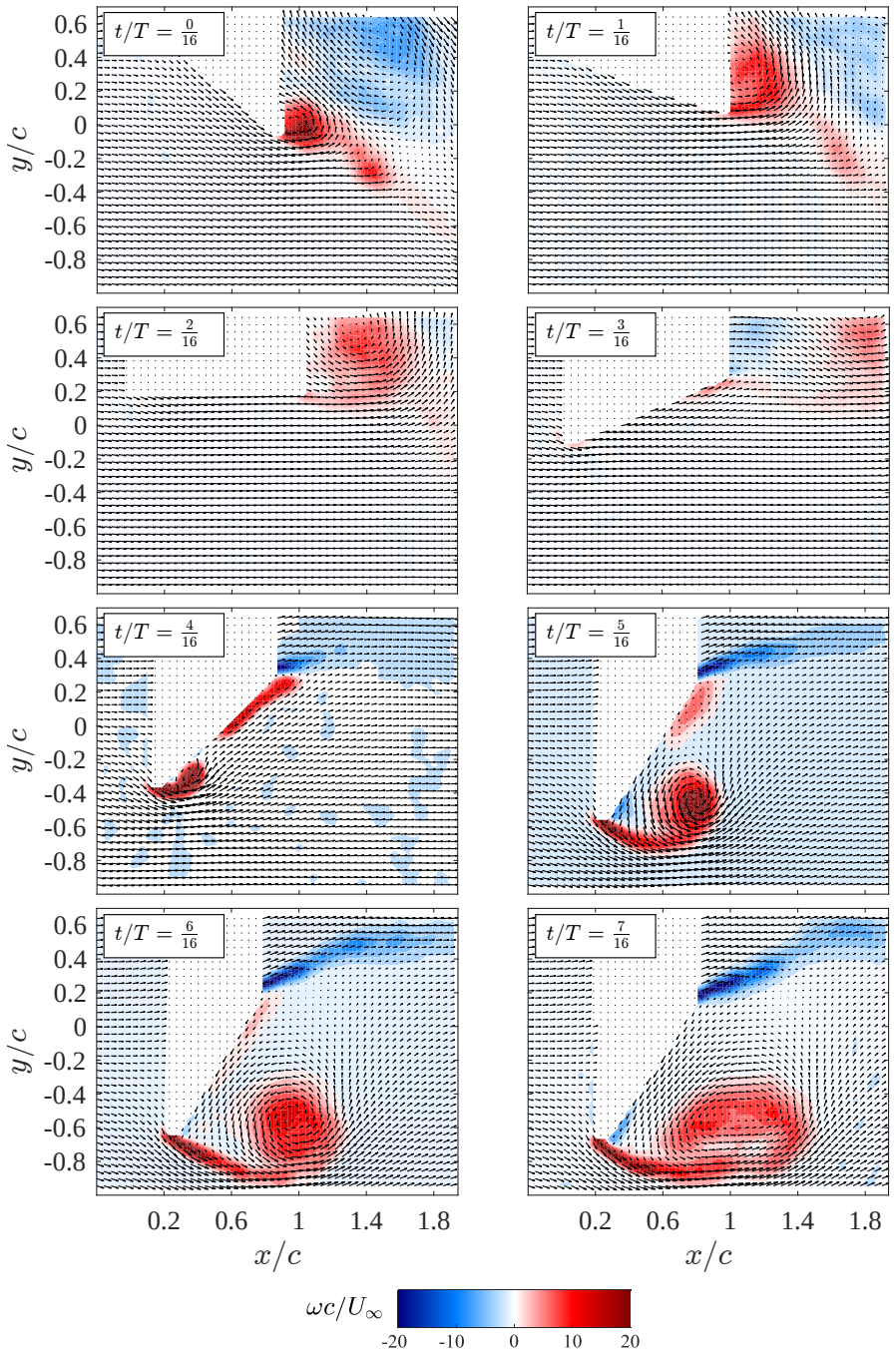

Figure G.2: Vorticity distribution overlaid with velocity vectors around the rigid foil with $k = 0.083$, $\theta_0 = 60°$, and $\Phi = 45°$.

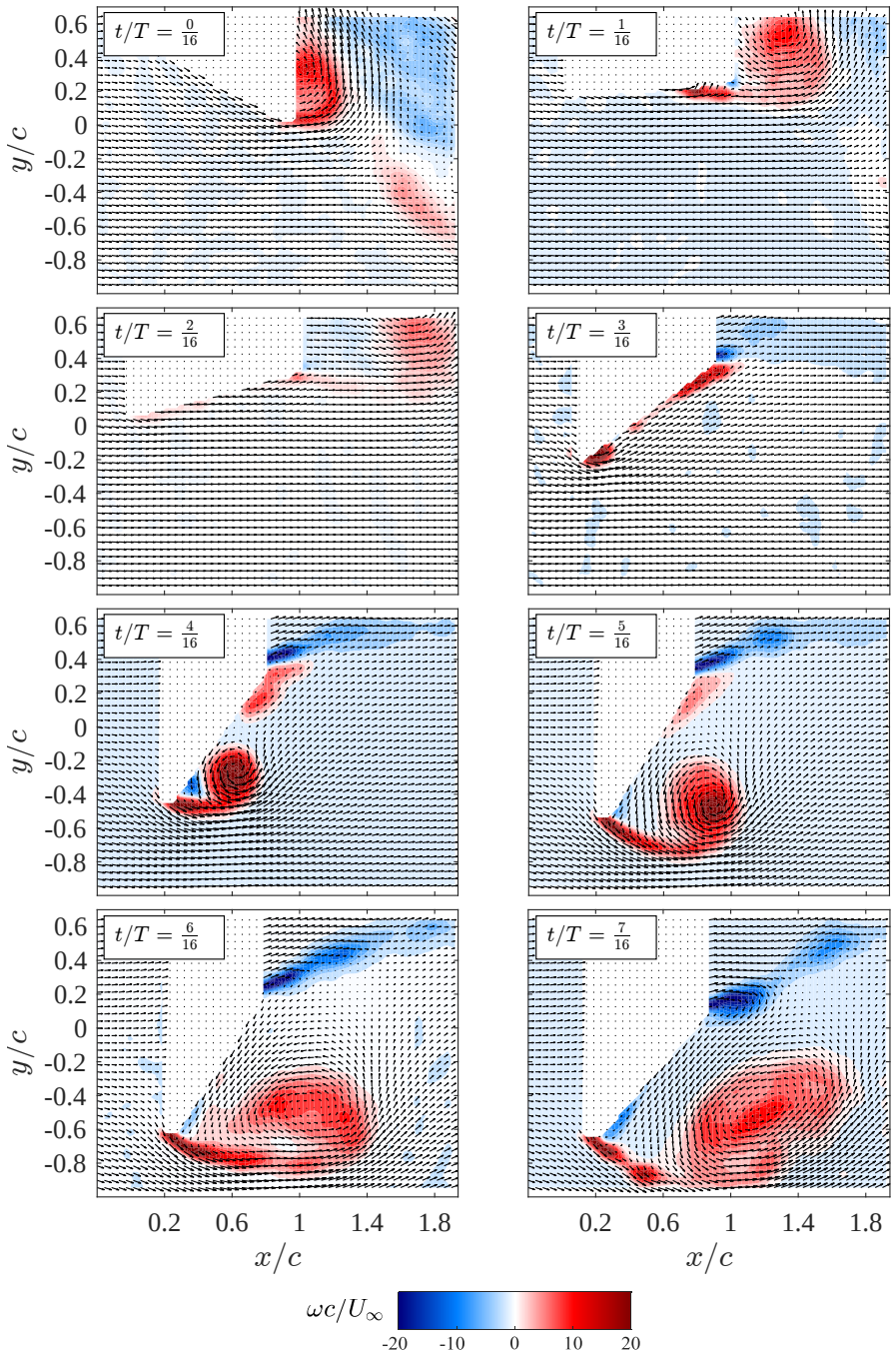

Figure G.3: Vorticity distribution overlaid with velocity vectors around the rigid foil with $k = 0.083$, $\theta_0 = 60°$, and $\Phi = 60°$.

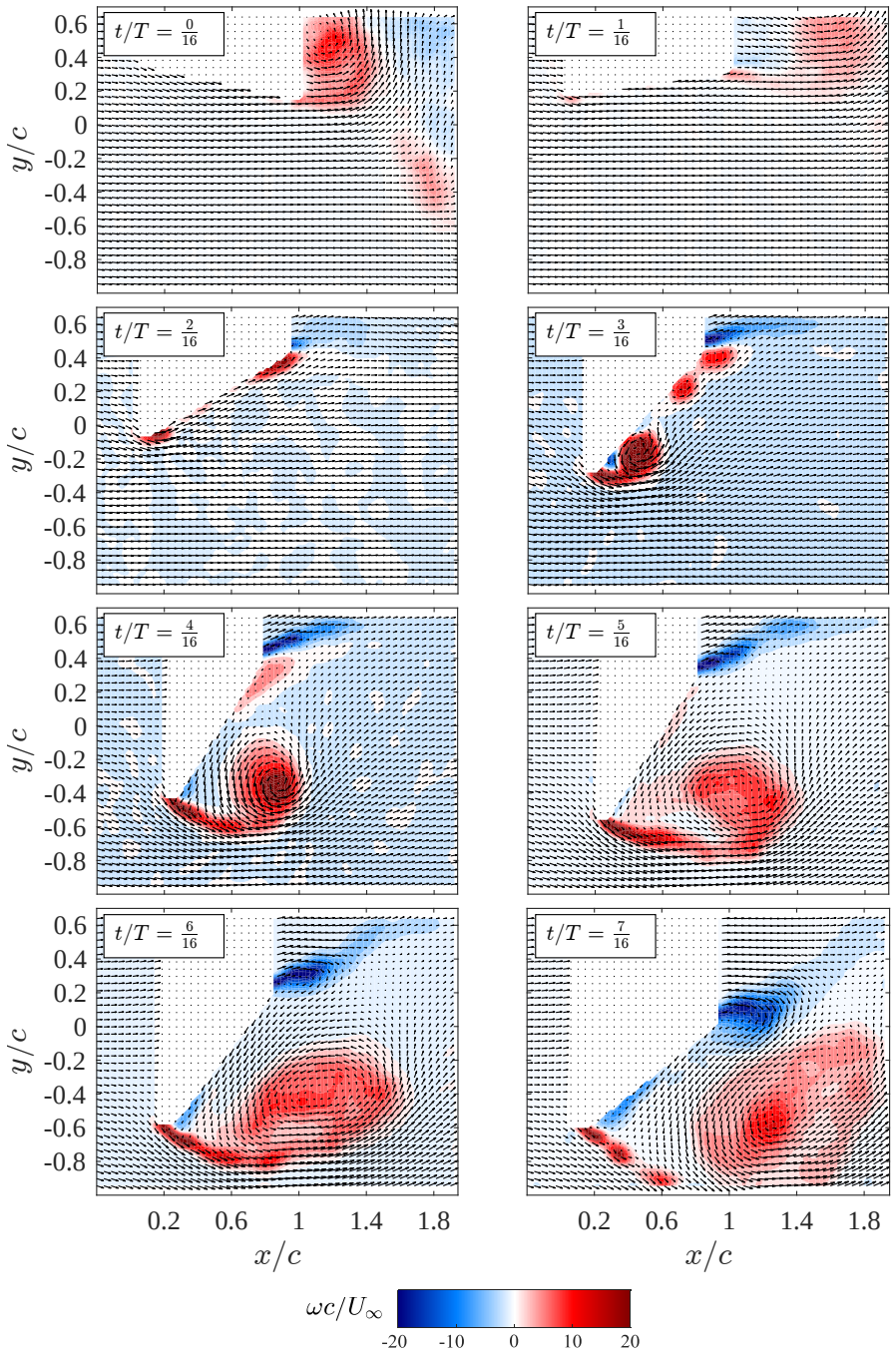

Figure G.4: Vorticity distribution overlaid with velocity vectors around the rigid foil with $k = 0.083$, $\theta_0 = 60°$, and $\Phi = 75°$.

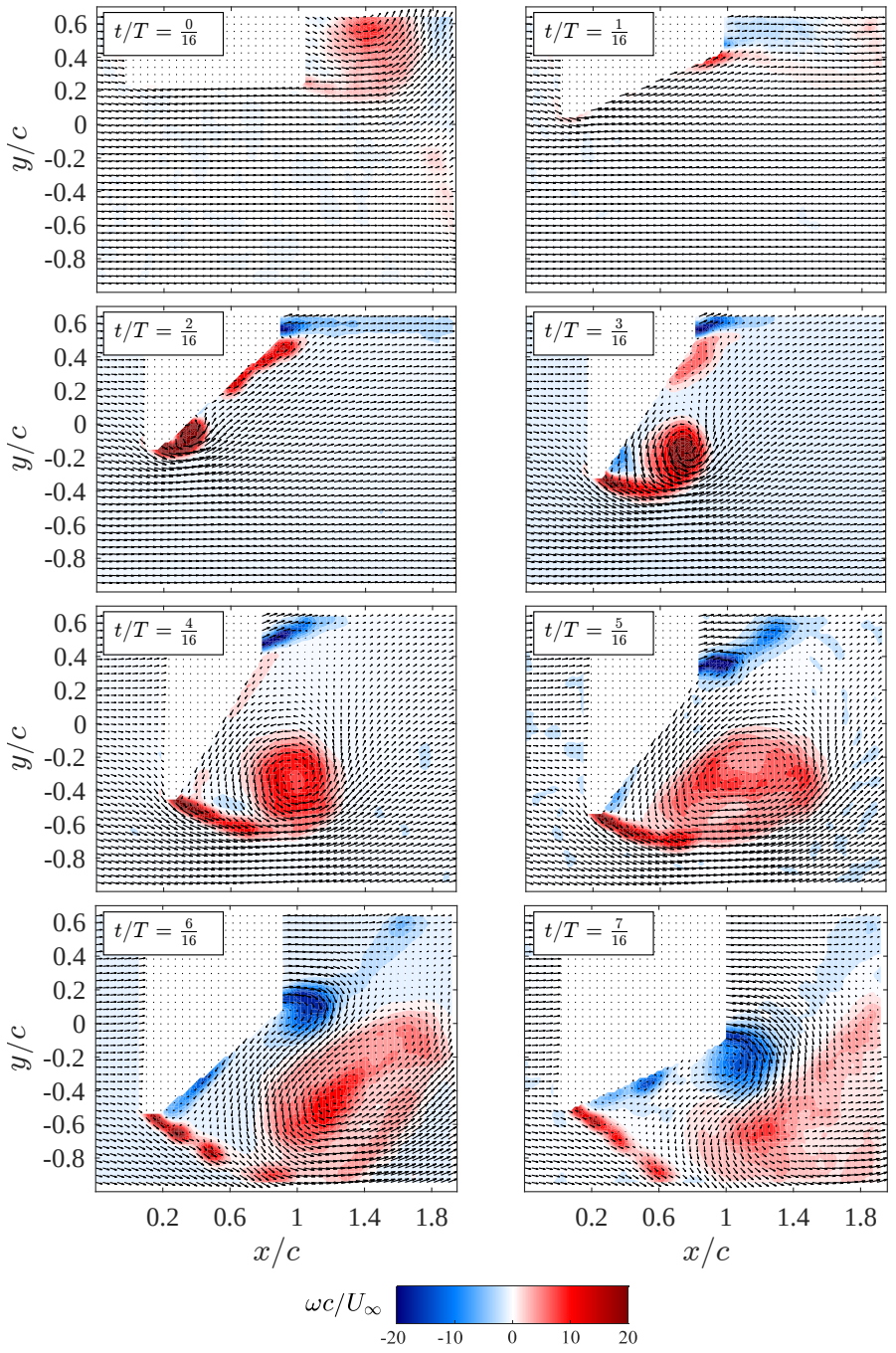

Figure G.5: Vorticity distribution overlaid with velocity vectors around the rigid foil with $k = 0.083$, $\theta_0 = 60°$, and $\Phi = 90°$.

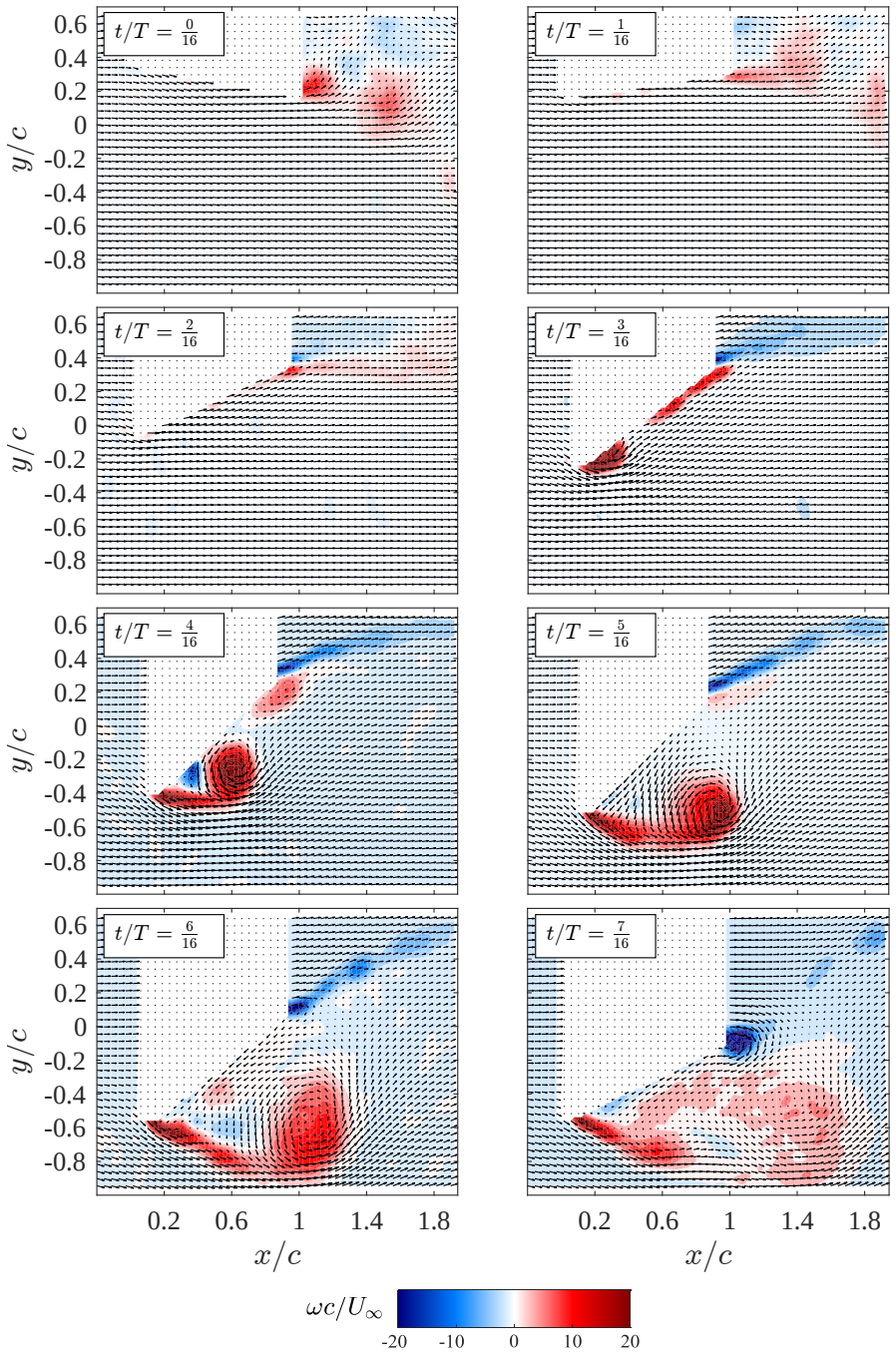

Figure G.6: Vorticity distribution overlaid with velocity vectors around the rigid foil with $k = 0.083$, $\theta_0 = 45°$, and $\Phi = 75°$.

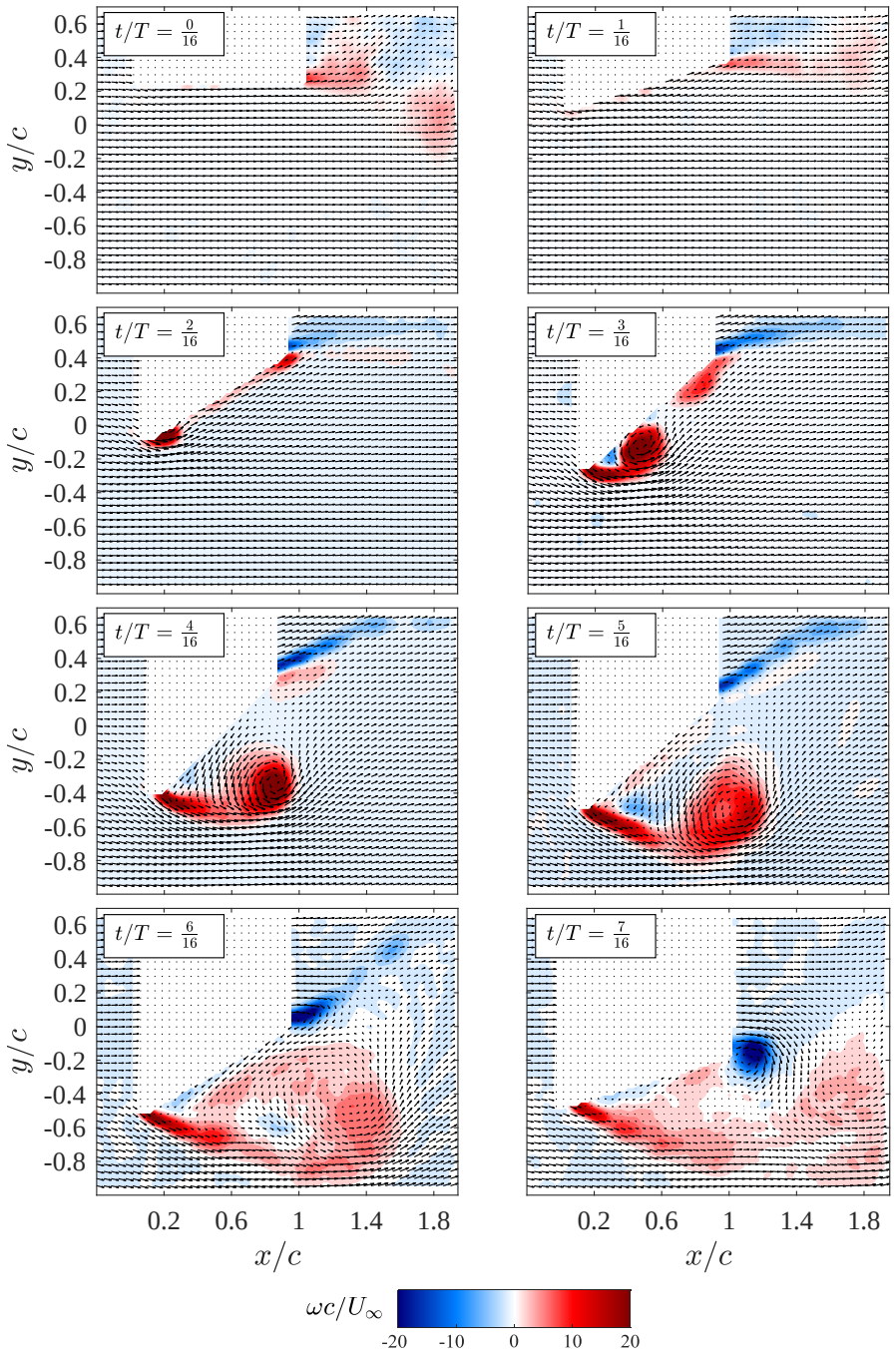

Figure G.7: Vorticity distribution overlaid with velocity vectors around the rigid foil with $k = 0.083$, $\theta_0 = 45°$, and $\Phi = 90°$.

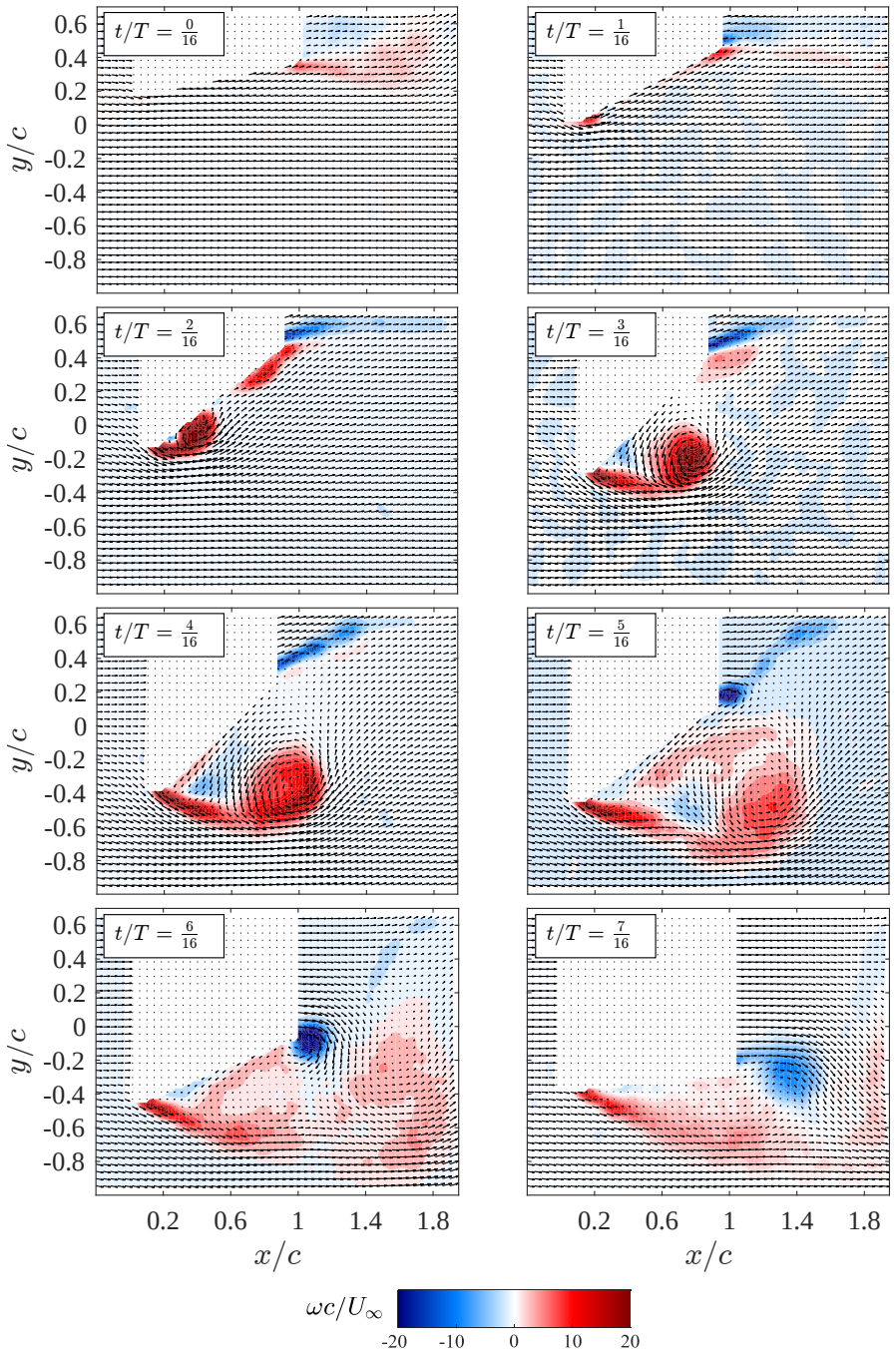

Figure G.8: Vorticity distribution overlaid with velocity vectors around the rigid foil with $k = 0.083$, $\theta_0 = 45°$, and $\Phi = 105°$.

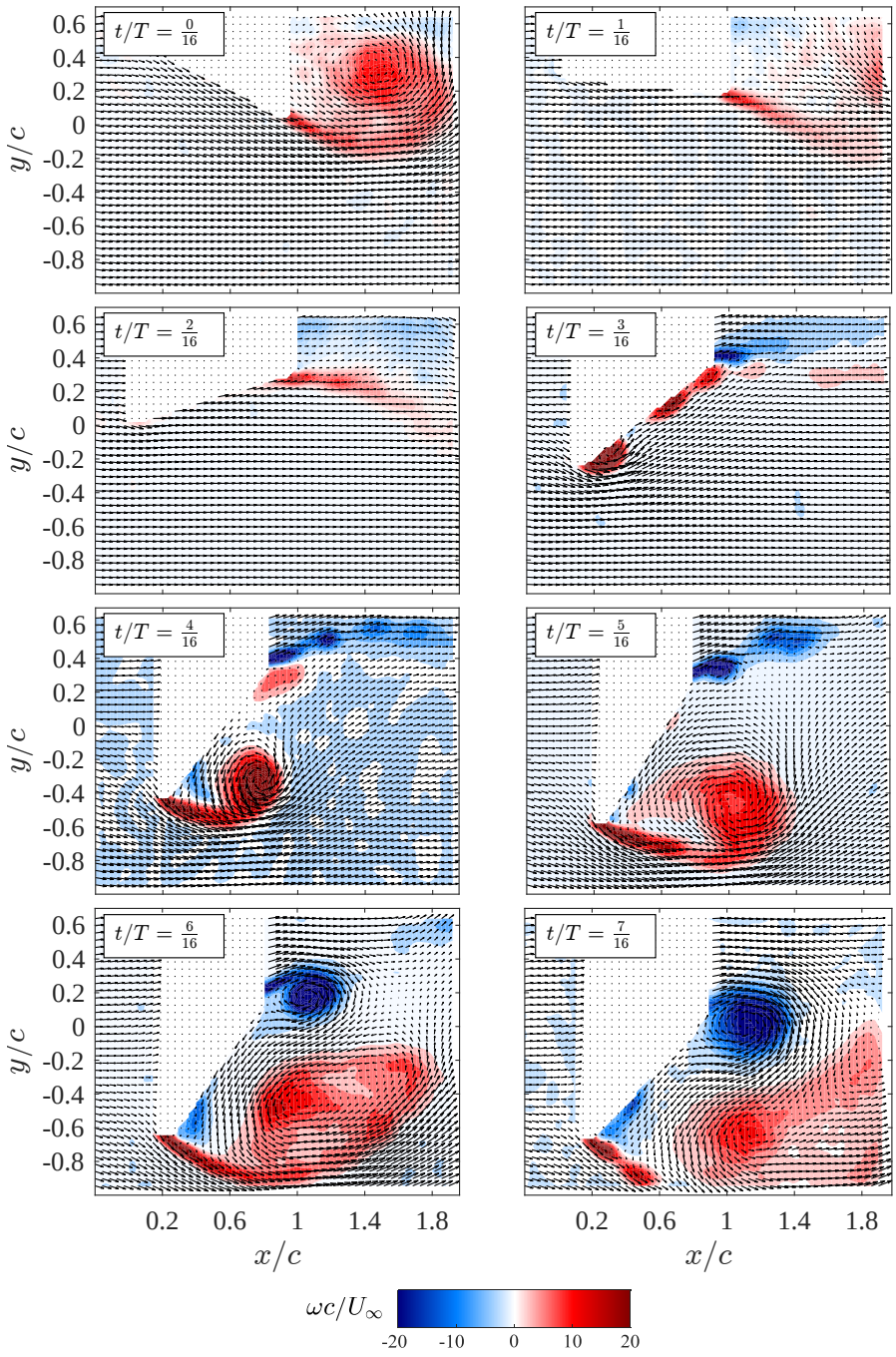

Figure G.9: Vorticity distribution overlaid with velocity vectors around the rigid foil with $k = 0.063$, $\theta_0 = 60°$, and $\Phi = 60°$.

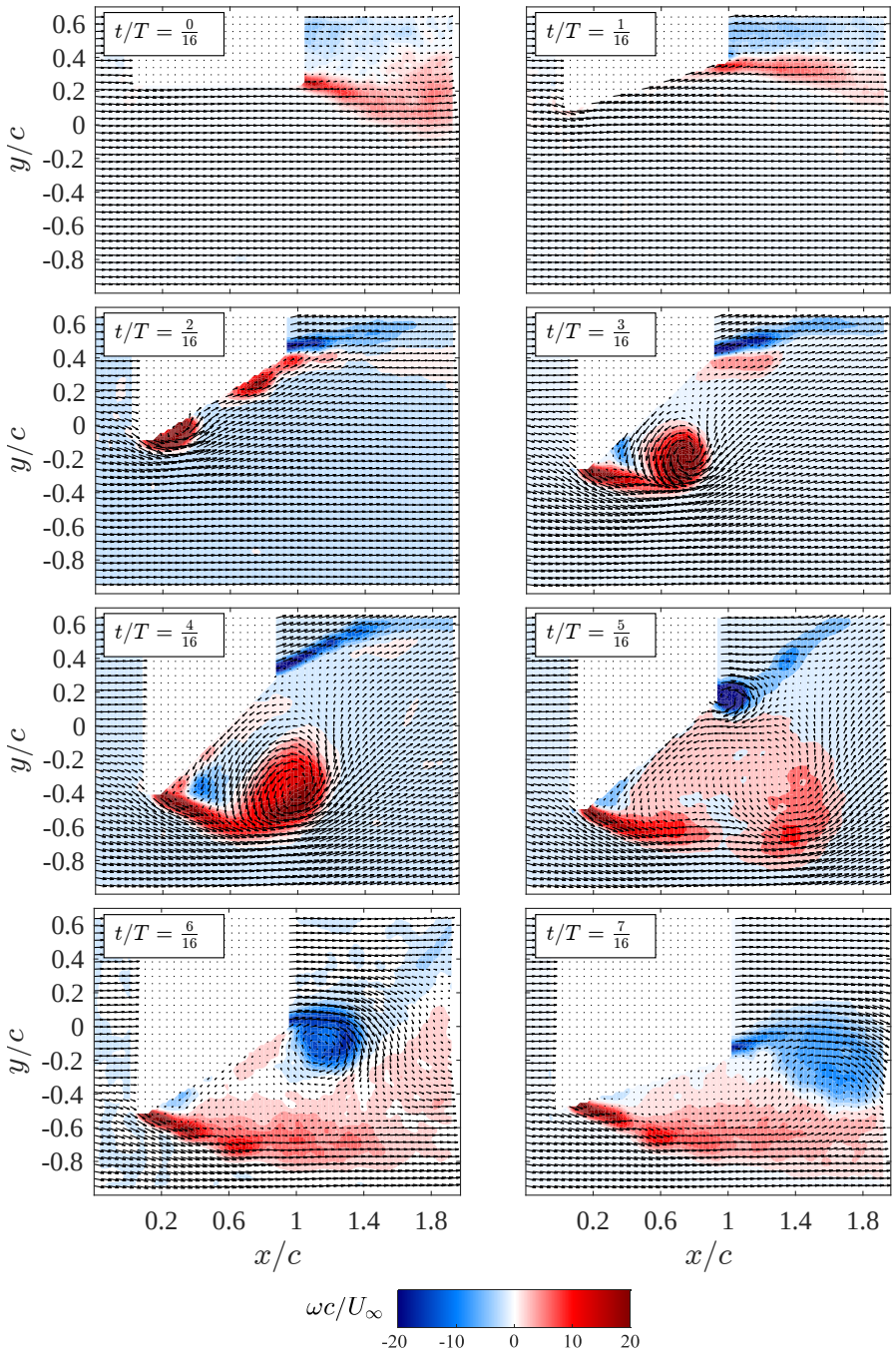

Figure G.10: Vorticity distribution overlaid with velocity vectors around the rigid foil with $k = 0.063$, $\theta_0 = 45°$, and $\Phi = 90°$.

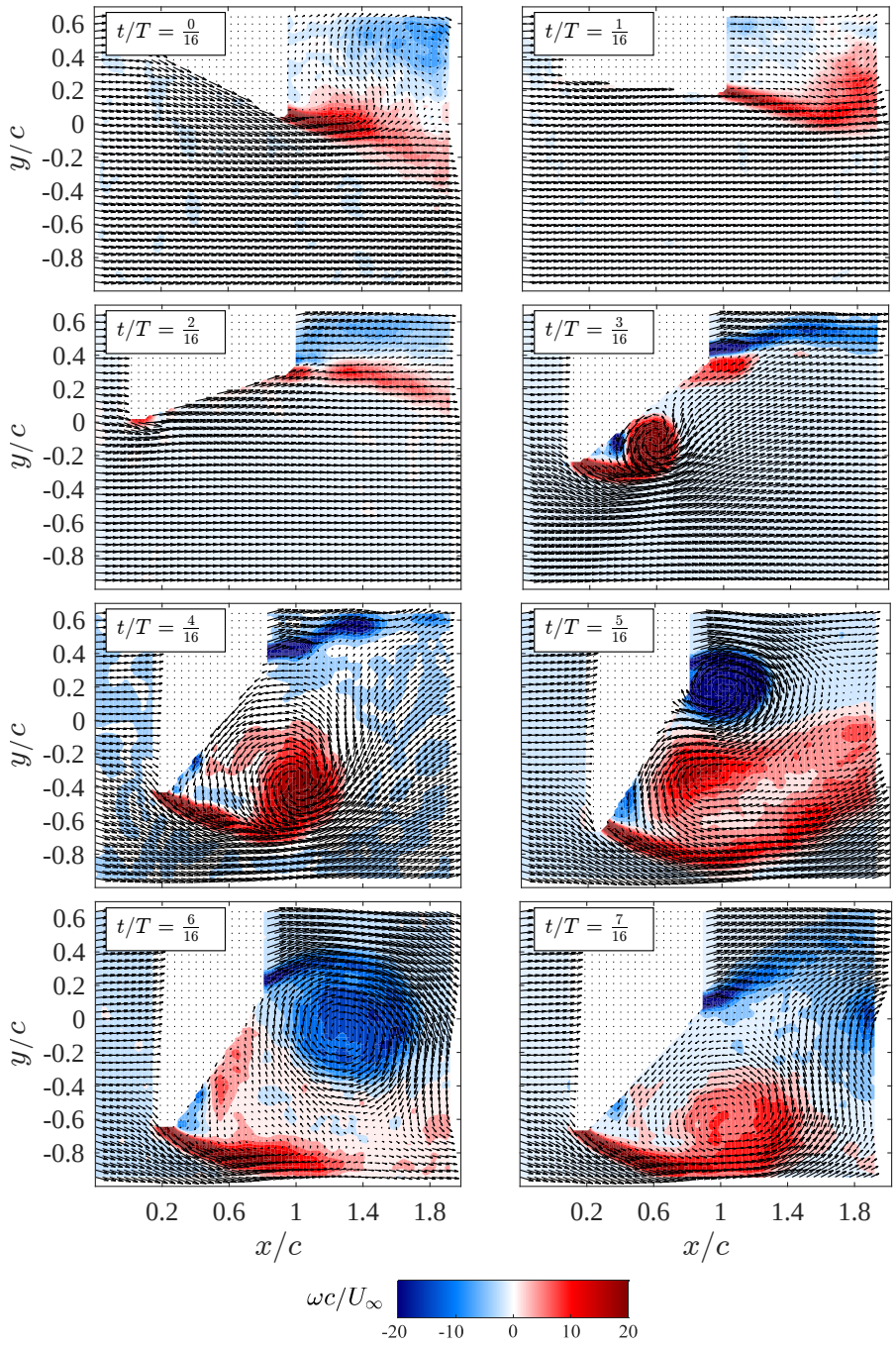

Figure G.11: Vorticity distribution overlaid with velocity vectors around the rigid foil with $k = 0.042$, $\theta_0 = 60°$, and $\Phi = 60°$.

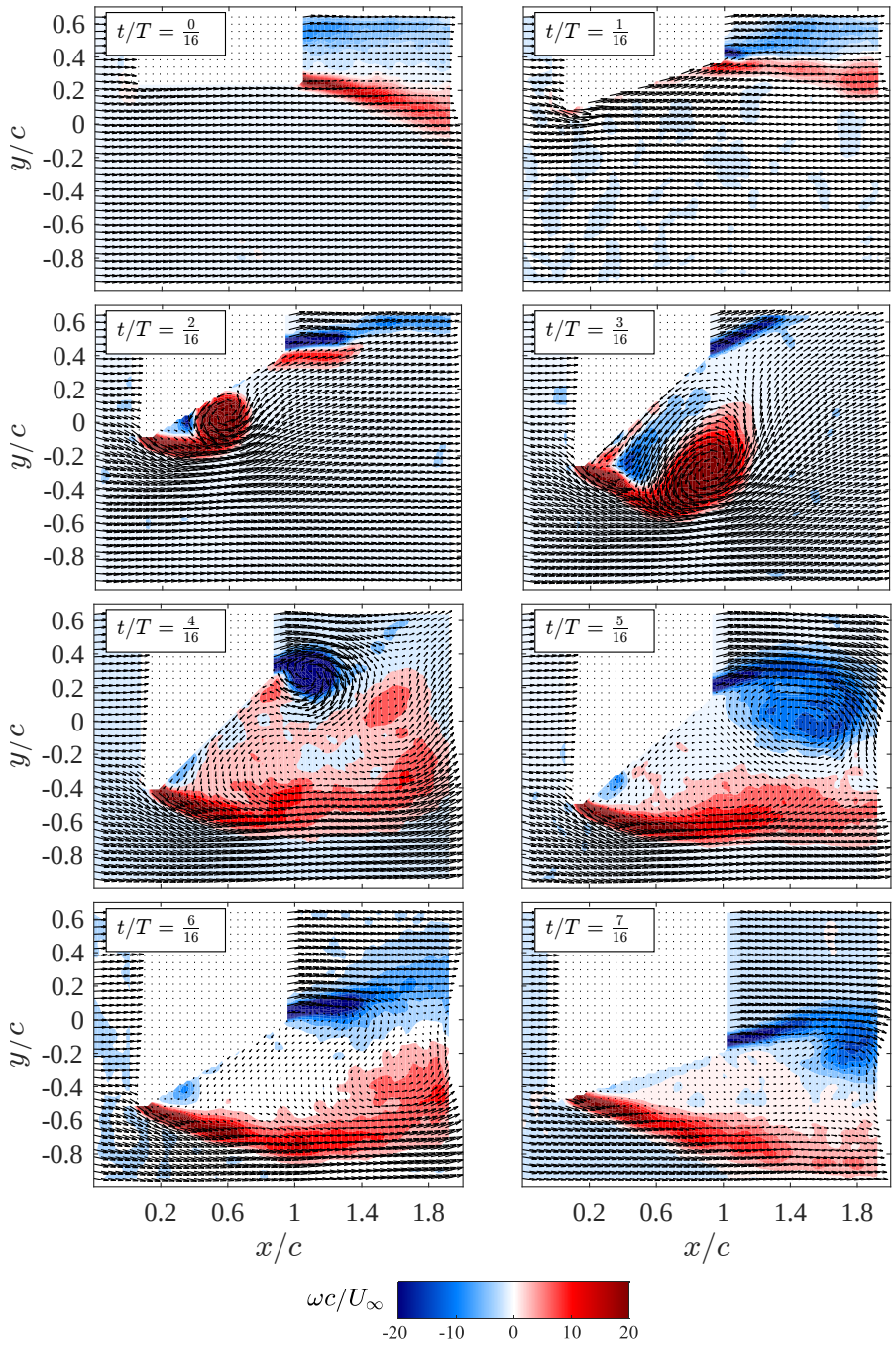

Figure G.12: Vorticity distribution overlaid with velocity vectors around the rigid foil with $k = 0.042$, $\theta_0 = 45°$, and $\Phi = 90°$.

Appendix H: Flexible LE Foil Force Measurements

This chapter contains all C_L curves for the flexible LE foil configurations after the processing techniques of Sections 2.2.4 and 2.2.5 have been applied. The results are organized according to Table H.1.

Table H.1: Table of C_L results for all force measurement runs.

Figure	θ_0 [°]	Φ [°]	k	κ $[N-m/rad]$
H.1	45	30 : 15 : 120	0.042	0.13
H.2	60	30 : 15 : 120	0.042	0.13
H.3	75	30 : 15 : 120	0.042	0.13
H.4	45	30 : 15 : 120	0.042	0.07
H.5	60	30 : 15 : 120	0.042	0.07
H.6	75	30 : 15 : 120	0.042	0.07

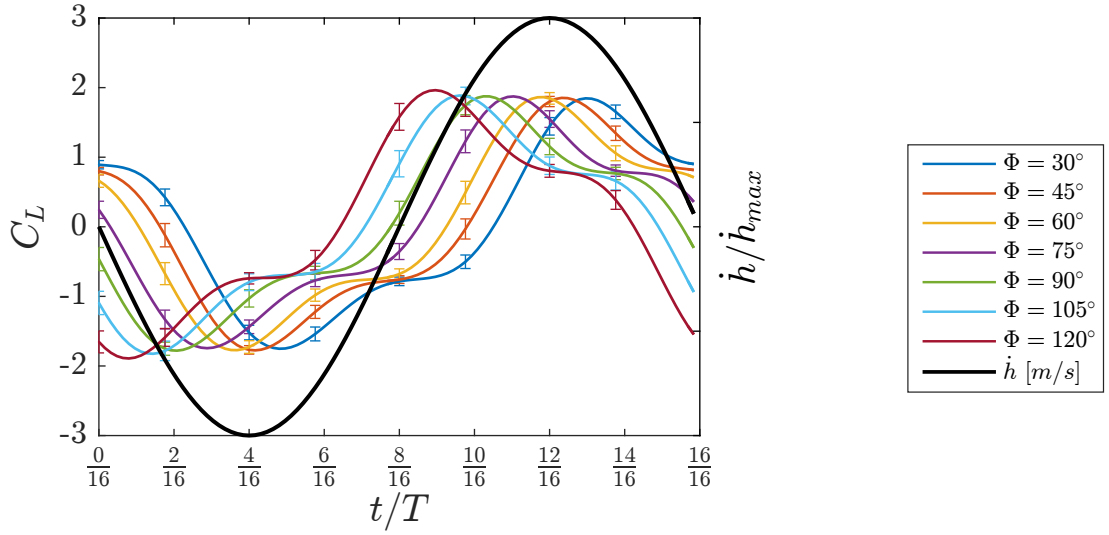

Figure H.1: Lift coefficient for all Φ tested $(30 : 15 : 105°)$, $\theta = 45°$, $k = 0.042$, $\kappa = 0.13\ N - m/rad$.

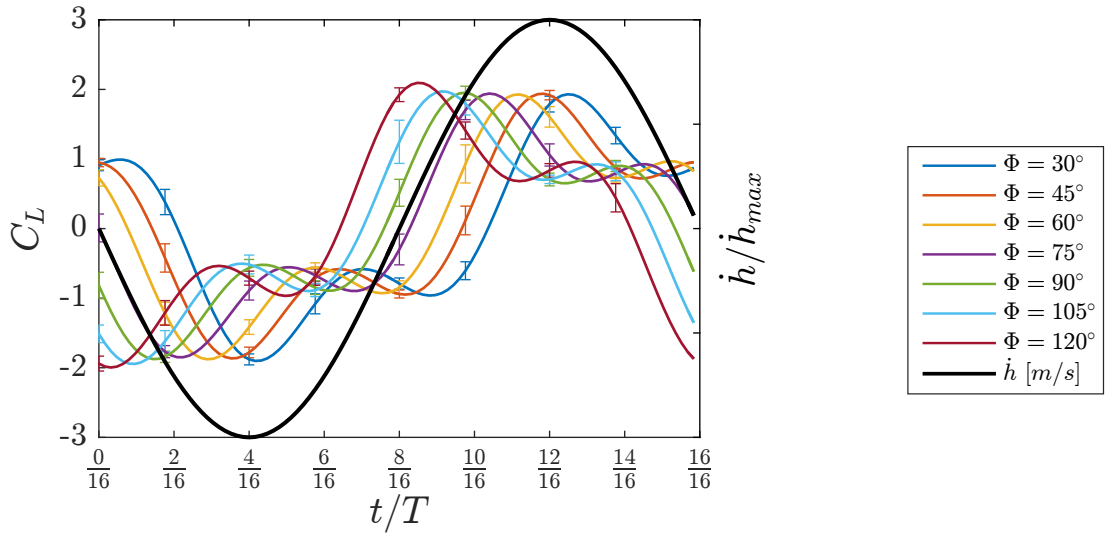

Figure H.2: Lift coefficient for all Φ tested $(30 : 15 : 105°)$, $\theta = 60°$, $k = 0.042$, $\kappa = 0.13\ N - m/rad$.

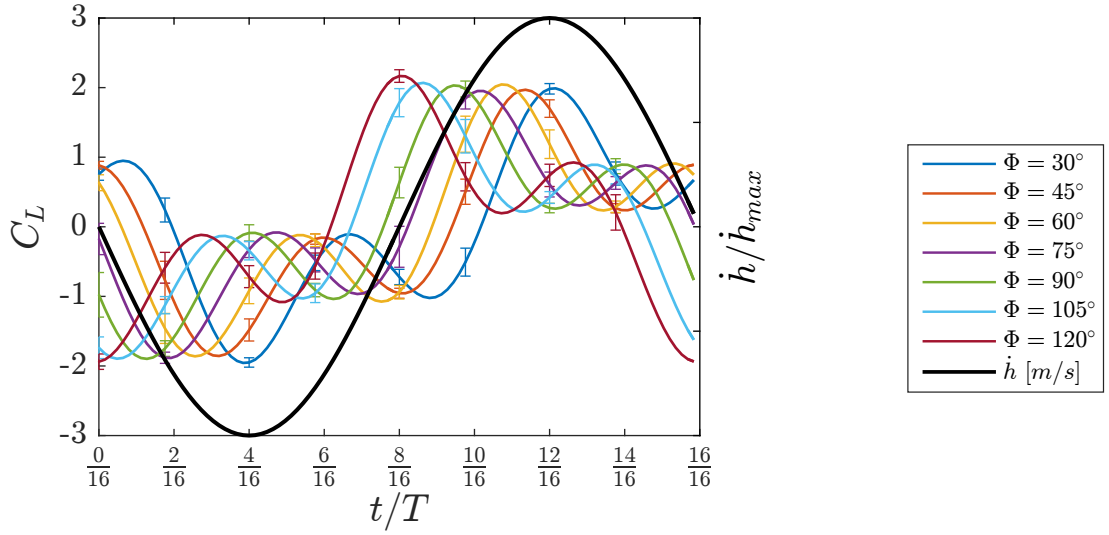

Figure H.3: Lift coefficient for all Φ tested $(30 : 15 : 105°)$, $\theta = 75°$, $k = 0.042$, $\kappa = 0.13\ N - m/rad$.

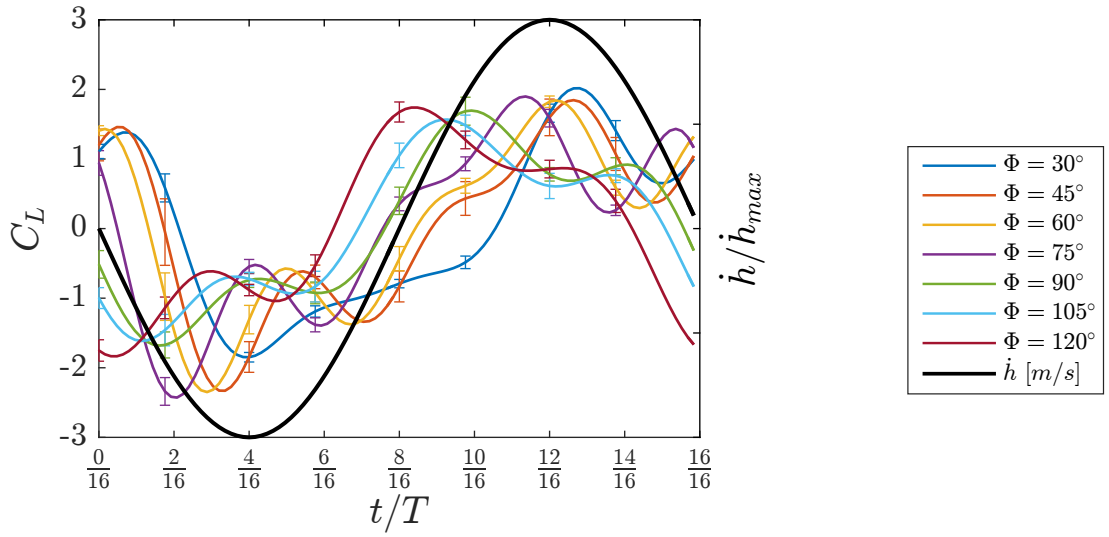

Figure H.4: Lift coefficient for all Φ tested $(30 : 15 : 105°)$, $\theta = 45°$, $k = 0.042$, $\kappa = 0.07\ N - m/rad$.

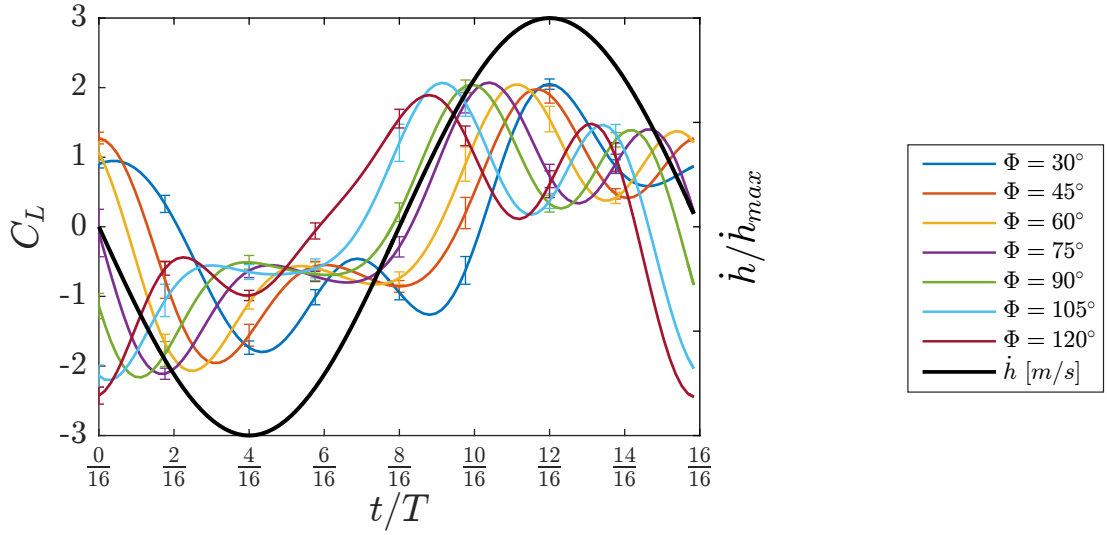

Figure H.5: Lift coefficient for all Φ tested $(30 : 15 : 105°)$, $\theta = 60°$, $k = 0.042$, $\kappa = 0.07\ N - m/rad$.

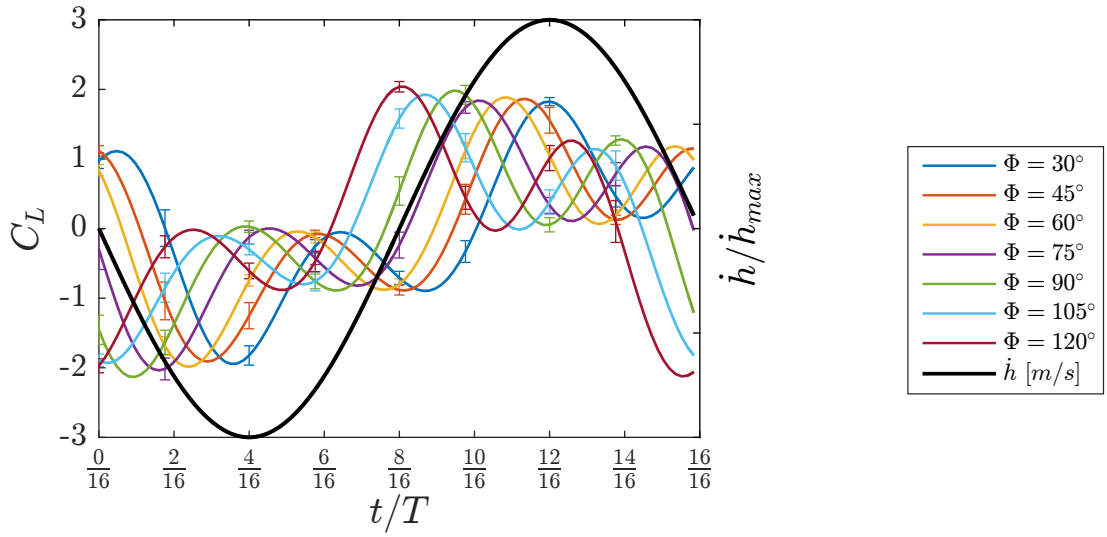

Figure H.6: Lift coefficient for all Φ tested $(30 : 15 : 105°)$, $\theta = 75°$, $k = 0.042$, $\kappa = 0.07\ N - m/rad$.

Appendix I: Flexible LE Foil PIV Measurements

This chapter contains all PIV measurements for the flexible LE foil configurations after the processing techniques of Section 2.4 has been applied. The results are organized according to Table I.1.

Table I.1: Table of PIV results for all flexible LE foil runs.

Figure	θ_0 [°]	Φ [°]	k	κ $[N-m/rad]$
I.1	60	60	0.042	0.13
I.2	45	90	0.042	0.13
I.3	60	60	0.042	0.07

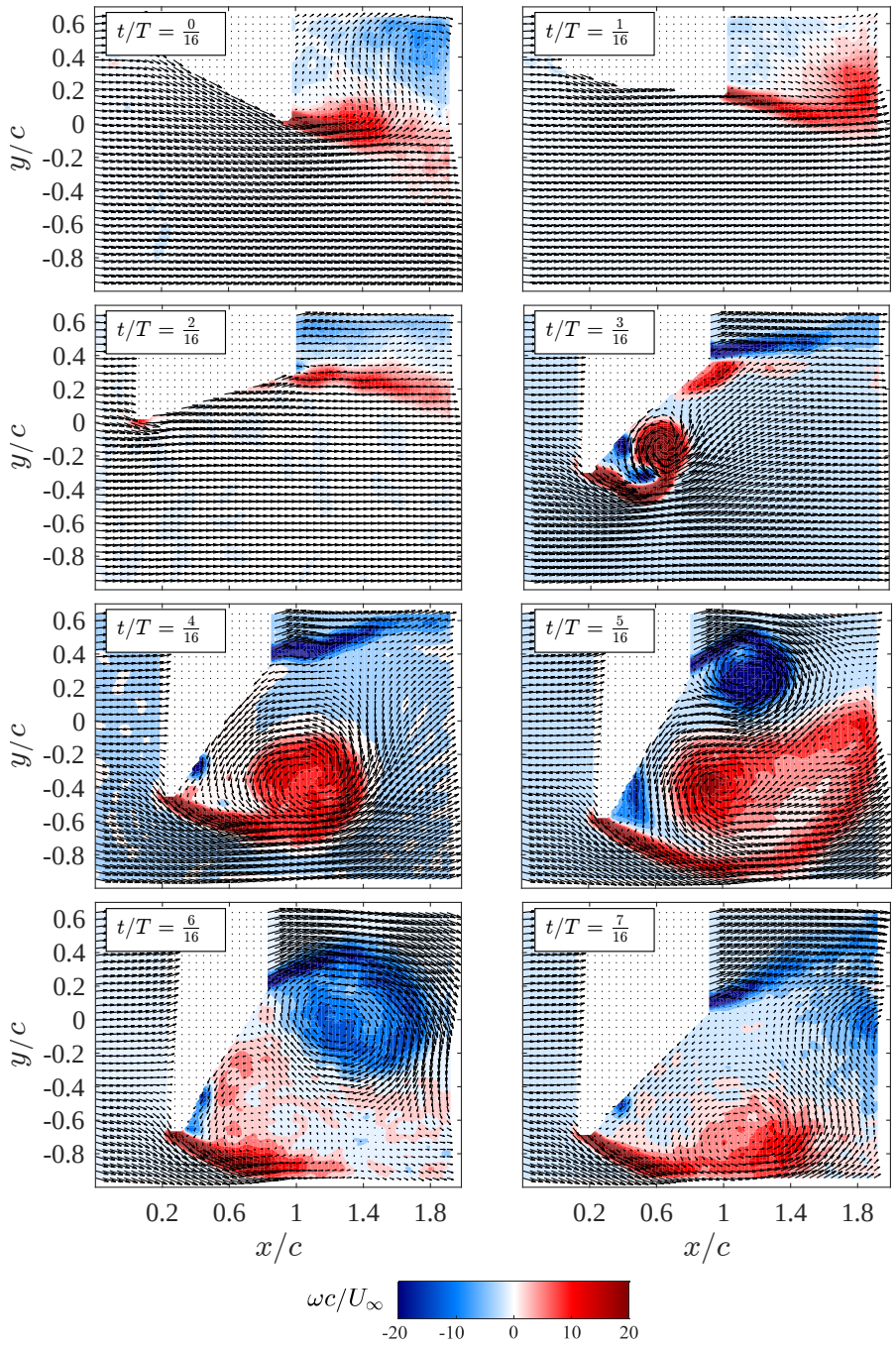

Figure I.1: Vorticity distribution overlaid with velocity vectors around the flexible LE foil with $k = 0.042$, $\theta_0 = 60°$, $\Phi = 60°$, and $\kappa = 0.13\ N - m/rad$.

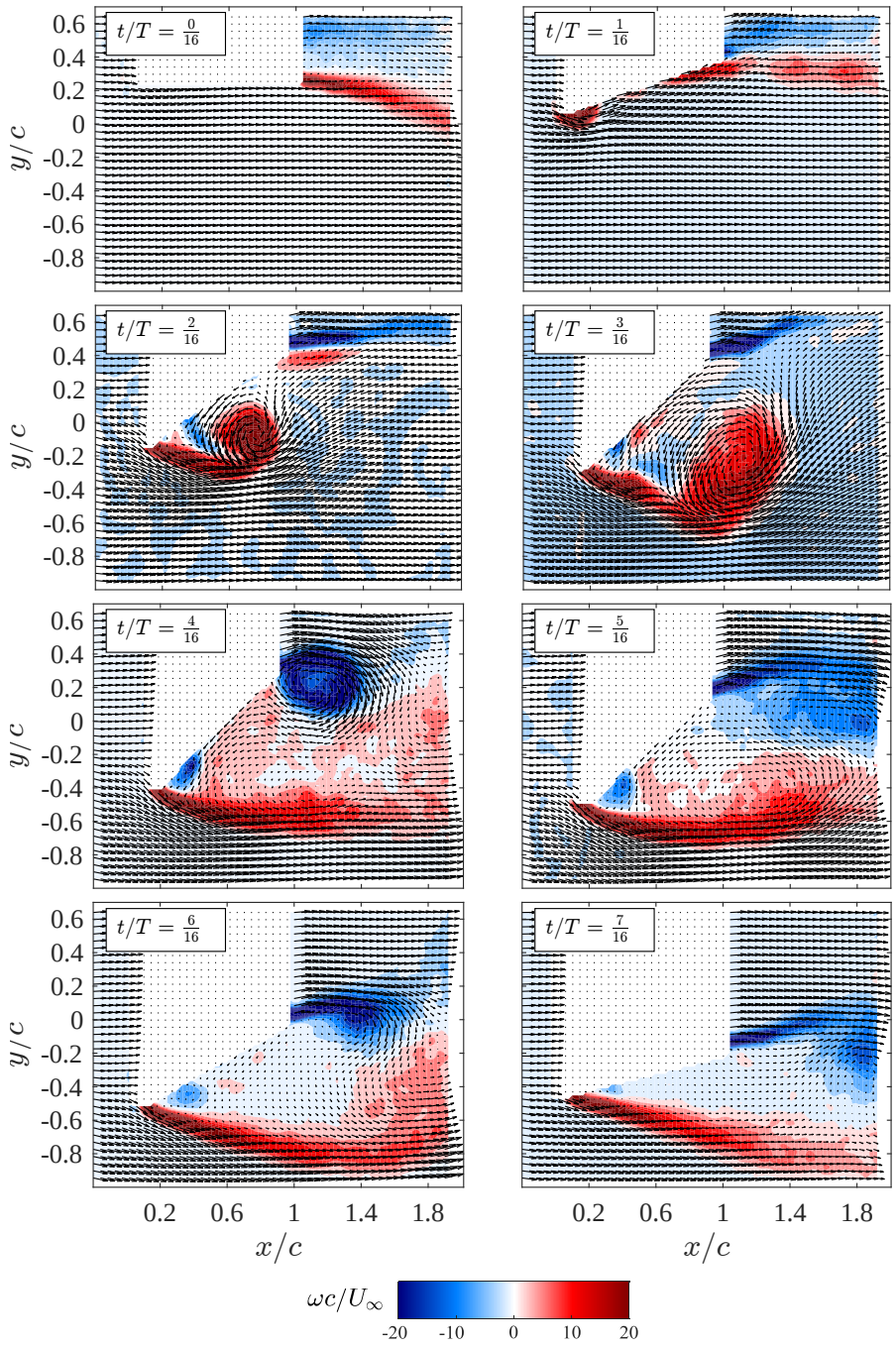

Figure I.2: Vorticity distribution overlaid with velocity vectors around the flexible LE foil with $k = 0.042$, $\theta_0 = 45°$, $\Phi = 90°$, and $\kappa = 0.13\ N - m/rad$.

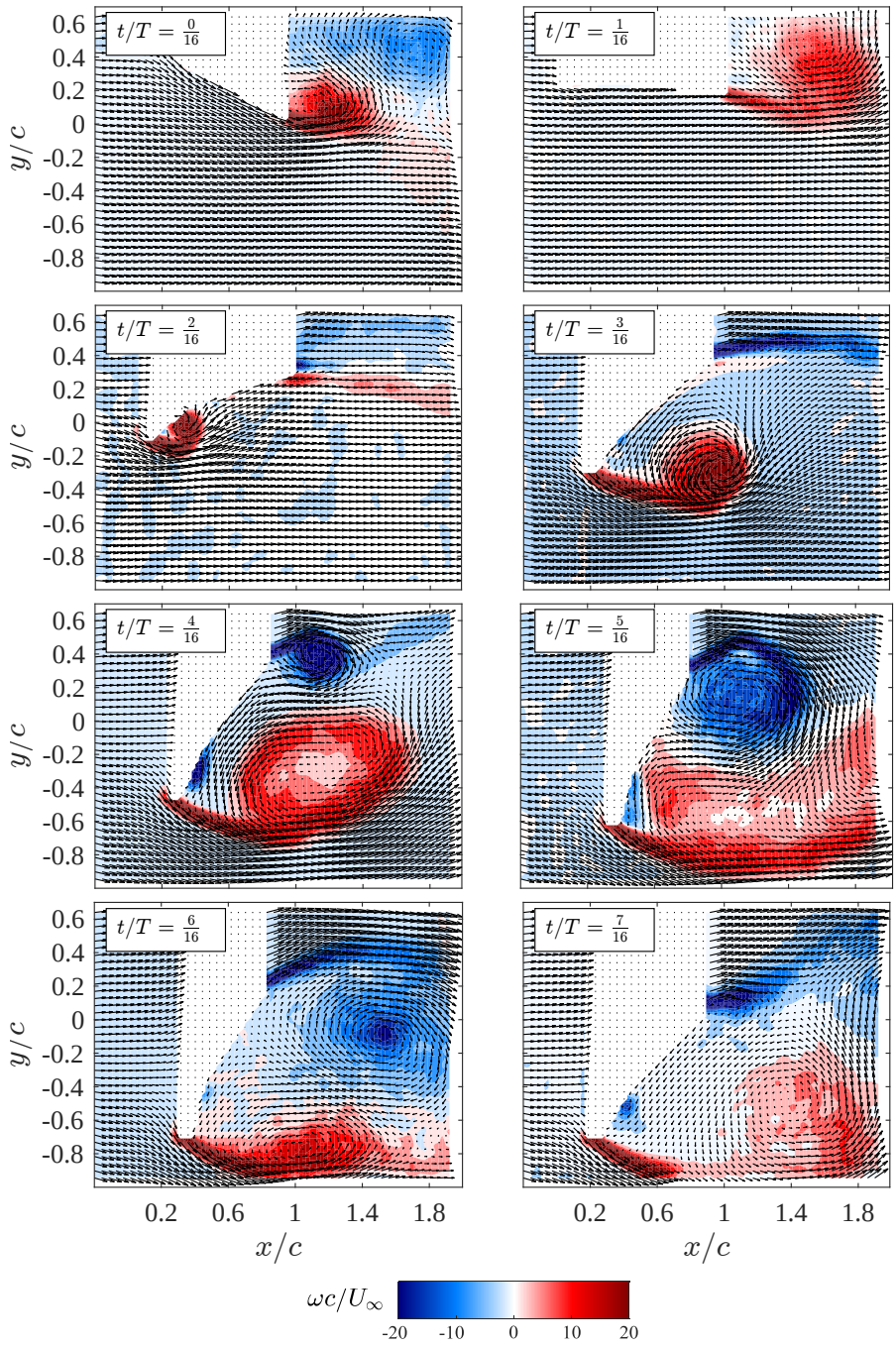

Figure I.3: Vorticity distribution overlaid with velocity vectors around the flexible LE foil with $k = 0.042$, $\theta_0 = 60°$, $\Phi = 60°$, and $\kappa = 0.07\ N - m/rad$.